Theory of exchange interaction and anisotropic magnetic properties of molecular magnets

Willem Van den Heuvel

Promotor
Prof. dr. Liviu F. Chibotaru

Proefschrift voorgedragen tot het behalen van de graad van Doctor in de Wetenschappen

Mei 2010

D/2010/10.705/32
ISBN 978-90-8649-339-5

Contents

Dankwoord

Ik wil graag prof. Liviu Chibotaru bedanken voor de begeleiding en hulp tijdens het onderzoek. Ik ben hem ook dankbaar voor het aandragen van de verschillende problemen die geleid hebben tot dit werk.

Ik dank het Fonds voor Wetenschappelijk Onderzoek - Vlaanderen (FWO) voor financiële steun onder het mandaat “Aspirant”.

Als laatste ben ik ook veel dank verschuldigd aan mijn ouders voor hun jarenlange steun.

Chapter 1

Introduction

The design and investigation of new magnetic molecular materials has attracted constantly increasing attention in the last years in view of their new physical properties and potential applications [1]. Besides traditional directions in magnetochemistry [2], a large research activity has been particularly focused in the last decade on the problem of design of efficient single-molecule magnets (SMM) and single-chain magnets (SCM) possessing large barriers of reversal of magnetization [3, 4]. Various metal complexes ranging from single-metal to tens-of-metals compounds have shown slow relaxation of magnetization as well as quantum tunnelling and interference effects below certain temperature [5]. These effects open the possibility for quantum storage and processing of information at the scale of individual molecules and represent the physical basis for the design of new multifunctional molecular materials. Although the synthesis of new SMMs and SCMs operating at elevated temperatures remains a desired goal, the recent progress in cryogenic techniques makes the devices operating at helium and subhelium temperatures feasible already now. In view of this perspective a new phase of research in molecular magnetism is foreseen which is directly aimed at the creation and investigation of electronic and spintronic devices and of magnetic materials based on already existing SMMs, SCMs and magnetic nanoparticles. This research undertaking will also require a multidisciplinary approach, combining the efforts of magnetochemists, device and material physicists and theoreticians.

Among the particular research objectives which the magnetochemistry community presently tries to meet are the following: 1) investigation of the possibilities of organization of SMMs on surfaces and design of compounds which do not alter their SMM properties upon this organization; 2) investigation of the factors allowing to diminish the environmental effects on individual SMMs; 3) investigation of spintronic properties of molecular magnets deposited on

conducting surfaces (carbon nanotubes, graphene strips, etc) or sandwiched between electrodes; 4) investigation of the effects of the non-collinear magnetic structure of SMMs involving strongly anisotropic metal ions on their conductivity; 5) investigation of spin dynamics in different organized structures of SMMs and of the possibility of addressing individual SMMs via the applied current; 6) investigation and design of new hard magnets on the basis of interacting single-chain magnets, and many others.

The new research directions in magnetochemistry and magnetic molecular materials put forward new challenges for the theory. First of all, the microscopic theory of exchange interactions, developed by Anderson in the late fifties of the last century [6, 7], was intended to explain the sign and amplitude of exchange interactions in insulating magnetic oxides, e.g. MnO, where the interaction between magnetic electrons is quite strong, and simple, involving a superexchange interaction over monoatomic ligands. The magnetic molecular materials of current interest involve lanthanide and actinide ions, whose electronic properties differ significantly from metal ions of the first transition row. Moreover the ligands bridging different magnetic ions are much diversified in the present magnetic materials. Therefore a first step in extending the microscopic theory to the new exchange systems requires the investigation of applicability of the Anderson and related theories in a broader range of electronic parameters. Second, the theory should be extended for an adequate description of magnetic properties of strongly anisotropic materials or, generally, materials involving metal ions with strong spin-orbit coupling on the metal sites as, e.g., polynuclear complexes with strongly anisotropic metal ions and magnetic nanoparticles doped with lanthanide ions. Third, the theoretical description of thermodynamic properties of long (infinite) magnetic molecular chains and cycles, including temperature and field-dependent magnetism, should be extended to the cases of strongly anisotropic metal ions, in particular, with arbitrarily oriented anisotropy axes, which is necessary for the rationalization of magnetic data of various heterometallic SCMs. This thesis contributes to all three mentioned aspects of the theory. Besides, the development of the theory has been applied to the description and rationalization of magnetic properties of newly synthesized magnetic molecules.

In chapter 2 the Anderson model of superexchange is compared with the valence bond configuration interaction (VBCI) model for the description of exchange interactions and with the results of exact diagonalization in a basic exchange model [2, 6]. The criterion of validity of these approaches is established for a wide domain of variation of electronic parameters. An alternative approach, free from the shortcomings of the Anderson and VBCI models, is proposed.

In chapter 3 the magnetism of the trinuclear complex $[Co_2PdCl_2(dpa)_4]$ is elucidated from a microscopic approach. The theory explains, in particular, the reason for the observed unusual temperature-independent paramagnetism, extending over the whole experimental temperature range. The interplay between

orbital degeneracy on the cobalt sites, spin-orbit coupling and peculiarities of electron delocalization between magnetic orbitals, which are responsible for this magnetic behavior, are analyzed.

In chapter 4 the theory of thermodynamics of the bond-decorated Ising model, which has relevance to recently synthesized heterometallic SCMs containing lanthanide ions, is presented. The required conditions for the lanthanide ion to have predominant Ising type exchange interaction with arbitrary neighboring metal ions are discussed. The theoretical approach is applied for the description of temperature-dependent magnetic susceptibility and field-dependent magnetization of a $[DyCuMoCu]_\infty$ chain, and a $[Dy_4Cr_4]$ complex.

In chapter 5 we analyze the reason for the axial nature of the ground state Kramers doublet of lanthanide ions placed in low-symmetric local environments, as found in lanthanide-containing polynuclear complexes, particularly, in the majority of Dy^{3+}-containing complexes. The "axiality" of the lowest doublet of lanthanide ions is of crucial importance for the slow relaxation of magnetization of the whole complex, since in the lanthanide SMMs the main contribution to the barrier of reversal of magnetization seems to come from individual lanthanide ions.

In chapter 6 the magnetization of recently fabricated Er^{3+}-doped PbF_2 nanoparticles is investigated within a crystal-field approach. Despite the high concentration of doping Er^{3+} ions and relatively large size (8 nm), these nanoparticles show unprecedented low temperature of blocking of magnetization (not detected down to $T = 0.35\,\mathrm{K}$), which points to negligible exchange interaction between Er^{3+} ions in the nanoparticles. Satisfactory simulation of magnetization within this model of independent Er^{3+} ions confirms the breakdown of the Néel-Brown giant spin model in these nanoparticles.

Finally in chapter 7 we give some conclusions and outlook for future work.

Bibliography

[1] D. Gatteschi, R. Sessoli, and J. Villain, *Molecular Nanomagnets* (Oxford University Press, Oxford, 2006)

[2] O. Kahn, *Molecular Magnetism* (VCH Publishers, New York, 1993)

[3] D. Gatteschi and R. Sessoli, Angew. Chem. Int. Ed. **42**, 268 (2003)

[4] C. Coulon, H. Miyasaka, and R. Clérac, in *Single-Molecule Magnets and Related Phenomena*, Structure and Bonding, Vol. 122, edited by R. Winpenny (Springer-Verlag, Berlin, 2006) pp. 163–206

[5] G. Christou, D. Gatteschi, D. N. Hendrickson, and R. Sessoli, Mater. Res. Bull. **25**, 66 (2000)

[6] P. W. Anderson, Phys. Rev. **115**, 2 (1959)

[7] P. W. Anderson, in *Magnetism*, Vol. 1, edited by G. T. Rado and H. Suhl (Academic Press, New York, 1963) p. 25

Chapter 2

Basic exchange model: Comparison of Anderson and valence bond configuration interaction approaches and an alternative exchange expression

Abstract The application of the Anderson and valence bond configuration interaction (VBCI) methods on a basic exchange model is investigated to assess their ability to calculate the exchange energy under a variety of physical situations, represented by the model parameters. The model comprises two metal orbitals and a central ligand orbital. We show that the validity of the Anderson method is not restricted to cases in which $U \ll \Delta$ if the "repulsion assisted transfer" term is included in the exchange expressions. We discuss the influence of the Coulomb repulsion in the metal and ligand orbitals on the Anderson method, pointing out some deficiencies of the Anderson orbitals. In cases of strong metal-ligand covalency, the VBCI method fails due to its perturbational character. The modified Anderson exchange performs better in some of these cases, depending on the specific situation. Based on the concept of a strict separation of covalent and exchange effects, we derive an exchange expression that overcomes all the discussed difficulties of the Anderson and VBCI methods.

W. Van den Heuvel and L. F. Chibotaru, Phys. Rev. B **76**, 104424 (2007)

2.1 Introduction

Models for the magnetic exchange interaction between metal centers have found wide use ever since the seminal work of Anderson [1]. Interest in exchange related phenomena has not ceased and model studies of such phenomena continue to appear in the physical [2–14] as well as in the chemical [15–20] literature. Numerous proposals for improvement and extension of the Anderson superexchange theory [1, 21, 22] have been made in the last decades (for a review see, e.g., Ref. [23] and references therein). Compared to them, the Valence Bond Configuration Interaction (VBCI) approach [17, 24], represented a radically different method to describe exchange interactions, which is now widely used. The general Anderson method is based on orthogonal localized molecular orbitals on the metal sites. These orbitals include the effect of the covalent chemical bond between the metal and the ligands. Some modifications of the original Anderson model, concerning the definition of the starting orbitals, have also been proposed [23, 25]. The VBCI approach was succesfully applied by Zaanen, Sawatzky and Allen to charge transfer insulators [26], while to the exchange problem it was applied by the first two authors and Geertsma [24, 27]. Unlike Anderson's method, VBCI uses atomic starting orbitals and includes chemical bonding through configuration interaction. In Ref. [24] the authors claimed that the Anderson theory would break down when the ligand-to-metal charge transfer energy becomes lower then the metal-to-metal charge transfer energy [24]. Although plenty of studies concerning the magnetic exchange have appeared where one of these theories are used, a quantitative analysis of the latter claim and a more general investigation of the applicability of both theories seems to be lacking. It is this gap that we want to fill with this paper. The two methods are tested by applying them to a basic model system consisting of two metal orbitals and a ligand orbital, occupied by four electrons (or two holes). Then, the capability of each approximation to reproduce the singlet-triplet splitting can be assessed by comparison with each other and with the result of an exact diagonalization within this model. It will be shown that the original Anderson approach has to be modified by including the "repulsion assisted transfer" when the condition $U \ll \Delta$ is not fulfilled. This modified Anderson exchange turns out to be more suitable than VBCI in some cases. At the same time we identify situations in which both of these methods fail. Guided by these findings, we finally propose an alternative method based on an exact incorporation of the metal-ligand covalency. With this new approach a quantitative agreement with the exact solution can be reached for a broad range of the model parameters.

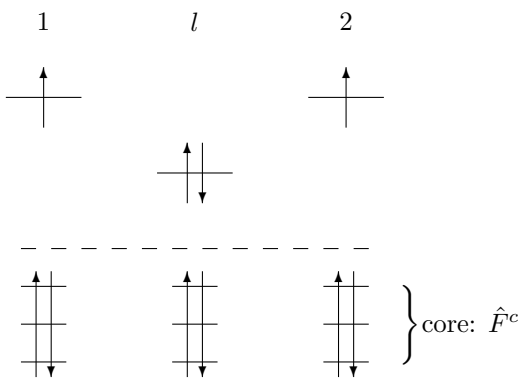

Figure 2.1: The model system in the electron representation showing the configuration used in the ROHF calculation.

2.2 The model system

The three-center system consisting of two magnetic metal ions separated by a diamagnetic ligand group has served for decades as a benchmark model to investigate the exchange interaction between metal centers. In this capacity, it has been used to test several theoretical approaches to the problem of magnetic exchange (for a review, see Ref. [23] and references therein; [17]). Of particular interest is the version with four (or two) electrons in three orbitals centered on the sites since it represents a basic model in which superexchange can be studied using a minimum of parameters. Going into more detail, the model system comprises two identical metal centers separated by a central ligand center. The three sites may be placed in a linear way although this is not necessary. One "atomic" real orbital is placed on each site. The orbitals on the metal sites are of course identical while the only condition on the ligand orbital is that it must not be orthogonal by symmetry to the metal orbitals. Without loss of generality the three orbitals are supposed to be s-like from now on. Further, the orbitals are made mutually orthogonal. The starting orbitals on the metal sites are denoted as ϕ_1 and ϕ_2, the orbital on the ligand as ϕ_l. Four electrons are distributed over these three orbitals. The electron core that bears our model system is treated as invariant and exerts its influence through the Fock operator $\hat{F}^c$. The situation is presented schematically in Fig. 2.1. Interactions included are the one-electron transfer between metal and ligand $t = \langle\phi_1|\hat{F}^c|\phi_l\rangle = \langle\phi_2|\hat{F}^c|\phi_l\rangle$ and the on-site Coulomb repulsion $U = \langle\phi_1(1)\phi_1(2)|\frac{1}{r_{12}}|\phi_1(1)\phi_1(2)\rangle = \langle\phi_2(1)\phi_2(2)|\frac{1}{r_{12}}|\phi_2(1)\phi_2(2)\rangle$ and $U' = \langle\phi_l(1)\phi_l(2)|\frac{1}{r_{12}}|\phi_l(1)\phi_l(2)\rangle$. The electronic Hamiltonian for the system is

then as follows:

$$H^{\mathrm{el}} = \sum_{\sigma}\Big[h_{11}(n_{1\,\sigma}+n_{2\,\sigma}) + h_{ll}n_{l\,\sigma} + \frac{1}{2}U(n_{1\,\sigma}n_{1\,-\sigma}+n_{2\,\sigma}n_{2\,-\sigma}) + \frac{1}{2}U'n_{l\,\sigma}n_{l\,-\sigma} + t(a^{\dagger}_{1\,\sigma}a_{l\,\sigma}+a^{\dagger}_{l\,\sigma}a_{1\,\sigma}+a^{\dagger}_{2\,\sigma}a_{l\,\sigma}+a^{\dagger}_{l\,\sigma}a_{2\,\sigma})\Big], \quad (2.2.1)$$

where $h_{ii} = \langle\phi_i|\hat{F}^c|\phi_i\rangle$, $n_{i\,\sigma} = a^{\dagger}_{i\,\sigma}a_{i\,\sigma}$, and $a^{\dagger}_{i\,\sigma}$ and $a_{i\,\sigma}$ are the electron creation and annihilation operators corresponding to the atomic orbitals. Note that there is no direct interaction between the metal sites included. To simplify further description we pass to holes representation by interchanging creation and annihilation operators [28]:

$$\begin{aligned} H^{\mathrm{holes}} = {} & 4h_{11} + 2h_{ll} + 2U + U' \\ & + \sum_{\sigma}\Big[(-h_{11}-U)(n_{1\,\sigma}+n_{2\,\sigma}) + (-h_{ll}-U')n_{l\,\sigma} \\ & + \frac{1}{2}U(n_{1\,\sigma}n_{1\,-\sigma}+n_{2\,\sigma}n_{2\,-\sigma}) + \frac{1}{2}U'n_{l\,\sigma}n_{l\,-\sigma} \\ & - t(a^{\dagger}_{1\,\sigma}a_{l\,\sigma}+a^{\dagger}_{l\,\sigma}a_{1\,\sigma}+a^{\dagger}_{2\,\sigma}a_{l\,\sigma}+a^{\dagger}_{l\,\sigma}a_{2\,\sigma})\Big], \end{aligned}$$

and set to zero the one-hole energy on the metals:

$$H^{\mathrm{holes}} = \sum_{\sigma}\Big[\Delta n_{l\,\sigma} + \frac{1}{2}U(n_{1\,\sigma}n_{1\,-\sigma}+n_{2\,\sigma}n_{2\,-\sigma}) + \frac{1}{2}U'n_{l\,\sigma}n_{l\,-\sigma} - t(a^{\dagger}_{1\,\sigma}a_{l\,\sigma}+a^{\dagger}_{l\,\sigma}a_{1\,\sigma}+a^{\dagger}_{2\,\sigma}a_{l\,\sigma}+a^{\dagger}_{l\,\sigma}a_{2\,\sigma})\Big], \quad (2.2.2)$$

where $\Delta = h_{11} + U - h_{ll} - U'$. The further discussion will be built upon the Hamiltonian in Eq. (2.2.2).

In constructing the determinantal wave functions the central plane of symmetry is used to reduce the size of the Hamiltonian matrix and to label the wave functions according to their parity with respect to the plane (+ or −). We have then four $^1\Gamma_+$, two $^3\Gamma_-$, two $^1\Gamma_-$ and one $^3\Gamma_+$ states. The configuration with one hole on each metal center is contained in the $^1\Gamma_+$ and the $^3\Gamma_-$ sets so that the exchange interaction problem corresponds to the determination of the energy difference between the lowest $^3\Gamma_-$ and the lowest $^1\Gamma_+$ state. Therefore, we do not need to consider the states belonging to the other two sets. In the

atomic basis the wave functions of the ${}^1\Gamma_+$ set are:

$$|\mathrm{cov};0\,0\rangle = \frac{1}{\sqrt{2}}(a^\dagger_{1\uparrow}a^\dagger_{2\downarrow} - a^\dagger_{1\downarrow}a^\dagger_{2\uparrow})|0\rangle \tag{2.2.3}$$

$$|\mathrm{l\,m};0\,0\rangle = \frac{1}{2}(a^\dagger_{1\uparrow}a^\dagger_{l\downarrow} - a^\dagger_{1\downarrow}a^\dagger_{l\uparrow} + a^\dagger_{2\uparrow}a^\dagger_{l\downarrow} - a^\dagger_{2\downarrow}a^\dagger_{l\uparrow})|0\rangle \tag{2.2.4}$$

$$|\mathrm{m\,m};0\,0\rangle = \frac{1}{\sqrt{2}}(a^\dagger_{1\uparrow}a^\dagger_{1\downarrow} + a^\dagger_{2\uparrow}a^\dagger_{2\downarrow})|0\rangle \tag{2.2.5}$$

$$|\mathrm{l\,l};0\,0\rangle = a^\dagger_{l\uparrow}a^\dagger_{l\downarrow}|0\rangle, \tag{2.2.6}$$

and those of the ${}^3\Gamma_-$ set are (with $M_s = 1$):

$$|\mathrm{cov};1\,1\rangle = a^\dagger_{1\uparrow}a^\dagger_{2\uparrow}|0\rangle \tag{2.2.7}$$

$$|\mathrm{l\,m};1\,1\rangle = \frac{1}{\sqrt{2}}(a^\dagger_{1\uparrow}a^\dagger_{l\uparrow} - a^\dagger_{2\uparrow}a^\dagger_{l\uparrow})|0\rangle, \tag{2.2.8}$$

where the entries in the kets contain an abbreviated identification of the state, together with its S and M_S quantum numbers. The corresponding Hamiltonian matrices are[1]:

$$H^{{}^1\Gamma_+} = \begin{array}{c} \begin{array}{cccc} |\mathrm{cov};0\,0\rangle & |\mathrm{l\,m};0\,0\rangle & |\mathrm{m\,m};0\,0\rangle & |\mathrm{l\,l};0\,0\rangle \end{array} \\ \begin{pmatrix} 0 & -\sqrt{2}t & 0 & 0 \\ & \Delta & -\sqrt{2}t & -2t \\ & & U & 0 \\ & & & 2\Delta + U' \end{pmatrix} \end{array} \tag{2.2.9}$$

$$H^{{}^3\Gamma_-} = \begin{array}{c} \begin{array}{cc} |\mathrm{cov};1\,1\rangle & |\mathrm{l\,m};1\,1\rangle \end{array} \\ \begin{pmatrix} 0 & -\sqrt{2}t \\ & \Delta \end{pmatrix} \end{array}. \tag{2.2.10}$$

Within this model exact exchange splittings are obtained by diagonalizing the matrices (2.2.9) and (2.2.10). One notices immediately that there is no ferromagnetism possible in this system since the ${}^1\Gamma_+$ ground state always has a larger hybridization space at its disposal than the ${}^3\Gamma_-$ ground state. It is indeed a familiar experimental fact that antiferromagnetic interactions, if present, usually dominate [1, 21]. Following these defining preliminaries, we can now investigate the different approximation schemes.

[1] These matrices are found in Zaanen and Sawatzky [24] and in Shen *et al.* [29] but without the inclusion of U'.

2.3 Anderson and VBCI treatments of superexchange

2.3.1 Anderson approach

The Anderson method is an orbital based one. That is, a set of magnetic orbitals, localized at the metal sites, defines the ground and excited state configurations. Energy corrections are obtained by a perturbation approach in which excited configurations are mixed with the ground configurations. In constructing the starting orbitals, we follow closely the original Anderson recipe [22]: restricted open-shell Hartree-Fock (ROHF) orbitals are constructed for the high-spin configuration with one hole on each metal site. This corresponds to the first (covalent) $^3\Gamma_-$ state in our case. Then the singly occupied orbitals (Bloch waves in the crystal) are transformed into equivalent localized Wannier functions (the Anderson magnetic orbitals). The restricted Hartree-Fock procedure ensures the pure spin character of the determinantal states, which is of course a necessary condition to speak about the "singlet-triplet" splitting. The idea behind the orbital part of this method is that the covalent interaction between the metal and ligand orbitals is already included from the beginning while the on-site electron repulsion remains strong enough to keep the electrons mainly localized on the metals [1]. The ground configurations are those with one hole in each magnetic orbital where every hole may be spin up or spin down. The degeneracy of these configurations is guaranteed by including in the zero-order Hamiltonian only those parts of the total Hamiltonian that do not transfer holes between orbitals. These are the diagonal hole energies and the classic Coulomb repulsions. Differentiation is then brought into the ground manifold through the action of an effective perturbation Hamiltonian. This Hamiltonian reduces in every order of perturbation to the well-known effective spin-Hamiltonian. For the case of only two metal centers it takes the form: $H^{\text{eff}} = 2J_{\text{exch}}\hat{\mathbf{S}}_\mathbf{1}\hat{\mathbf{S}}_\mathbf{2}$. The energy difference between the lowest triplet and singlet state is thus $2J_{\text{exch}}$.

We now proceed to calculate the Anderson orbitals for our molecular system. These result from a ROHF calculation on the electron configuration with two spin-up electrons (See Fig. 2.1). It can be shown that exactly the same orbitals are obtained from a HF calculation on the equivalent hole configuration (see Appendix 2.A). From the three starting orbitals symmetry adapted orbitals are constructed:

$$\phi_+ = \frac{1}{\sqrt{2}}(\phi_1 + \phi_2) \tag{2.3.1}$$

$$\phi_l = \phi_l \tag{2.3.2}$$

$$\phi_- = \frac{1}{\sqrt{2}}(\phi_1 - \phi_2). \tag{2.3.3}$$

Minimizing the energy of the determinant with one spin-up hole on each metal (using the Hamiltonian in Eq. (2.2.2)), we arrive at the HF matrix that mixes orbitals (2.3.1) and (2.3.2):

$$F_+^{\text{holes}} = \begin{array}{c} \begin{matrix} \phi_+ & \phi_l \end{matrix} \\ \begin{pmatrix} 0 & -\sqrt{2}t \\ & \Delta \end{pmatrix} \end{array}. \tag{2.3.4}$$

A few remarks should be made about this HF matrix. It depends only on two parameters (Δ and t) instead of the four independent parameters that describe the system, and the eigenfunctions will only depend on the ratio of t and Δ. This indicates that the HF orbitals have a limited flexibility to adjust themselves to the physical situation. For instance, the HF orbitals are unaffected by an increase of the on-site Coulomb repulsion (the other parameters being the same). The repulsion parameters U and U' are absent in the HF matrix because repulsion takes place only when two paired holes reside on the same atomic center. This favors our present purpose since no further iterations are necessary to solve the HF equations. Exact solutions are obtained by diagonalizing (2.3.4). The HF orbitals and their energies are:

$$\Psi_{1+} = c_1\phi_+ + c_2\phi_l \qquad \epsilon_{1+} = \frac{\Delta}{2} + \sqrt{\left(\frac{\Delta}{2}\right)^2 + 2t^2} \qquad = -\sqrt{2}t\frac{c_2}{c_1} \tag{2.3.5}$$

$$\Psi_- = \phi_- \qquad \epsilon_- = 0 \tag{2.3.6}$$

$$\Psi_{2+} = c_2\phi_+ - c_1\phi_l \qquad \epsilon_{2+} = \frac{\Delta}{2} - \sqrt{\left(\frac{\Delta}{2}\right)^2 + 2t^2} \qquad = \sqrt{2}t\frac{c_1}{c_2}, \tag{2.3.7}$$

where (for $\Delta \geq 0$):

$$c_1 = -\frac{1}{\sqrt{2}}\frac{t}{|t|}\sqrt{1 - \frac{1}{\sqrt{1 + 8(\frac{t}{\Delta})^2}}} \tag{2.3.8}$$

$$c_2 = \frac{1}{\sqrt{2}}\sqrt{1 + \frac{1}{\sqrt{1 + 8(\frac{t}{\Delta})^2}}}. \tag{2.3.9}$$

It follows that $|c_2| \geq |c_1|$ for $\Delta \geq 0$ and that the orbitals depend solely on the ratio of t and Δ. Note also that $t\frac{c_1}{c_2}$ is always negative, regardless of the sign of t. Orbital Ψ_{1+} (Eq. (2.3.5)) is the bonding "ligand" orbital, which is doubly occupied in the electron configuration. In the hole picture however, it has the highest energy and is not occupied. In the configuration for which the orbitals are optimized, one spin-up hole resides in Ψ_- and one in Ψ_{2+}. The Anderson magnetic orbitals are then obtained by combining Ψ_- and Ψ_{2+} in a symmetric

and antisymmetric way, which provides the maximal possible localization of the holes within this approach:

$$A_1 = \frac{c_2+1}{2}\phi_1 - \frac{c_1}{\sqrt{2}}\phi_l + \frac{c_2-1}{2}\phi_2 \tag{2.3.10}$$

$$A_2 = \frac{c_2-1}{2}\phi_1 - \frac{c_1}{\sqrt{2}}\phi_l + \frac{c_2+1}{2}\phi_2 \tag{2.3.11}$$

The orbitals (2.3.5), (2.3.10) and (2.3.11) replace ϕ_l, ϕ_1 and ϕ_2, respectively, and define the configurations in the Anderson basis. The ground configurations are $b^\dagger_{1\uparrow}b^\dagger_{2\downarrow}|0\rangle$, $b^\dagger_{1\downarrow}b^\dagger_{2\uparrow}|0\rangle$, $b^\dagger_{1\downarrow}b^\dagger_{2\downarrow}|0\rangle$ and $b^\dagger_{1\uparrow}b^\dagger_{2\uparrow}|0\rangle$, where the b operators refer to the Anderson basis. The second quantized Hamiltonian is found by transforming Hamiltonian (2.2.2) to the new orbital basis (Appendix 2.B).

With these configurations as a starting point, the next step is to calculate the perturbational expression for the exchange splitting. If we have a general Hamiltonian $H = H^0 + H'$ where the ground state of H^0 is generally degenerate and H' denotes a perturbation, the effective perturbation Hamiltonian working in the space of the ground states of H^0 can be written as $H^{\text{eff}} = H^{(0)} + H^{(1)} + H^{(2)} + H^{(3)} + \cdots$ where the superscripts indicate the order of the perturbation after H'. We then have

$$\begin{aligned}
H^{(0)} &= P_0 H^0 P_0 \\
H^{(1)} &= P_0 H' P_0 \\
H^{(2)} &= P_0 H' \frac{P}{a} H' P_0 \\
H^{(3)} &= P_0 H' \frac{P}{a} H' \frac{P}{a} H' P_0 - P_0 H' P_0 H' \frac{P}{a^2} H' P_0 \\
H^{(4)} &= P_0 H' \frac{P}{a} H' \frac{P}{a} H' \frac{P}{a} H' P_0 - P_0 H' \frac{P}{a} H' \frac{P}{a^2} H' P_0 H' P_0 \\
&\quad - P_0 H' \frac{P}{a^2} H' \frac{P}{a} H' P_0 H' P_0 - P_0 H' \frac{P}{a} H' P_0 H' \frac{P}{a^2} H' P_0 \\
&\quad + P_0 H' \frac{P}{a^3} H' P_0 H' P_0 H' P_0,
\end{aligned} \tag{2.3.12}$$

where P_0 is the projection operator on the space of the ground states and $\frac{P}{a^n} = \frac{P}{(E_G^0 - H^0)^n}$ with P the projection operator on the space of excited states: $P = 1 - P_0$ and E_G^0 the unperturbed energy of the ground states. The total Hamiltonian (2.B.3) is divided in two parts: the unperturbed Hamiltonian (H^0) is taken as the first two lines of Eq. (2.B.3) which is, as mentioned before, the part that does not transfer holes between orbitals. The rest of Eq. (2.B.3) is considered as perturbation. Details of the procedure to evaluate the expressions in Eq. (2.3.12) are provided in Appendix 2.C. Working out the expressions to first and second order using Eq. (2.3.12) we get, ignoring constant terms (the

new matrix elements are defined in Eq. (2.B.2)):

$$H^{(1)}_{\text{And}} = -2\tilde{J}_{12}\hat{\mathbf{S}}_\mathbf{1}\hat{\mathbf{S}}_\mathbf{2} \tag{2.3.13}$$

$$H^{(2)}_{\text{And}} = 2\left[2\frac{(\tilde{t}_{12}+\tilde{V}_{1222})^2}{\tilde{U}-\tilde{K}_{12}} + 4\frac{\tilde{V}_{122l}(\tilde{t}_{1l}+\tilde{V}_{12l2})}{\tilde{\Delta}+\tilde{K}_{1l}-\tilde{K}_{12}} + \frac{(\tilde{V}_{1ll2})^2}{2\tilde{\Delta}+\tilde{U}'-\tilde{K}_{12}}\right]\hat{\mathbf{S}}_\mathbf{1}\hat{\mathbf{S}}_\mathbf{2}. \tag{2.3.14}$$

Note that the indices $1, 2, l$ now refer to the orbitals of the Anderson basis, A_1, A_2 and Ψ_{1+}, respectively. $H^{(1)}$ is just the ferromagnetic potential exchange between the overlapping Anderson magnetic orbitals [1]. The three terms in $H^{(2)}$ result from three second order processes: the first is the well-known one-hole transfer between the magnetic orbitals [1]. The second is a hole transfer between metal and ligand and the third is a two-hole transfer between the metals and the ligand (the Nesbet term). The first term in (2.3.14) contains the kinetic exchange contribution, which was held responsible for antiferromagnetism in the original paper [1]: $\frac{4b_{12}^2}{U}\hat{\mathbf{S}}_\mathbf{1}\hat{\mathbf{S}}_\mathbf{2}$, using the notation from that paper, where b_{12} stands for the kinetic energy matrix element between the magnetic orbitals. "Kinetic energy" here means the energy of an electron in the field of the diamagnetic lattice. Expressed in terms of the present model (see Appendix 2.B):

$$b_{12} = \tilde{F}^c_{12} + 2\tilde{V}_{1l2l} - \tilde{V}_{1ll2} = -(\tilde{t}_{12} + 2\tilde{V}_{1222}). \tag{2.3.15}$$

In the present model, b_{12} is equivalent to the off-diagonal matrix element of the Fock operator for the ferromagnetic configuration (Fig. 2.1). We note however that this equivalence takes place only for this simple model. In a general case, b_{12} is always understood as an off-diagonal matrix element of the Fock operator for the corresponding ferromagnetic configuration. We can see that b_{12} must not be confused with $\tilde{t}_{12}$ here. The latter is the matrix element of the "one-hole kinetic energy". The entanglement of terms originates from the transition from electrons to holes, where only the total matrix elements between determinantal configurations are left unchanged, apart from a possible change of sign. Consider, for example, the transfer of one electron or hole between the magnetic orbitals. This antiferromagnetic process contributes the first term to $H^{(2)}_{\text{And}}$, Eq. (2.3.14), and is shown schematically in Fig. 2.2. The corresponding matrix element is:

$$\langle A_1\bar{A}_2|H|A_2\bar{A}_2\rangle = \tilde{t}_{12} + \tilde{V}_{1222} = -(b_{12} + \tilde{V}_{1222}),$$

where the notation in the bracket denotes the determinantal hole configuration. Here we see that b_{12} is not the only term that transfers an electron between metal sites; $\tilde{V}_{1222}$ represents a process which may be called "repulsion assisted transfer" since the transfer of one electron (hole) is mediated by the repulsion with the other electron (hole). Depending on the relative sign of b_{12} and $\tilde{V}_{1222}$, the latter can either reinforce or weaken the antiferromagnetic interaction.

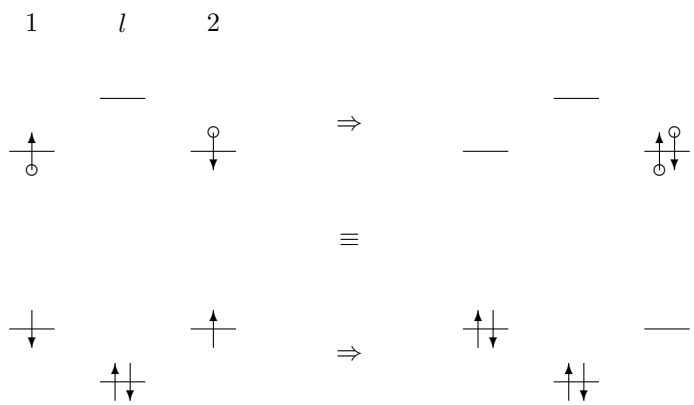

Figure 2.2: Schematic representation of the antiferromagnetic one-hole transfer process (upper part) and its equivalent electron transfer process (lower part).

2.3.2 Valence bond configuration interaction

Working out the perturbation Hamiltonians in Eq. (2.3.12) for the atomic basis system, using Eq. (2.2.2) and $H' = -t(a^\dagger_{1\,\sigma}a_{l\,\sigma} + a^\dagger_{l\,\sigma}a_{1\,\sigma} + a^\dagger_{2\,\sigma}a_{l\,\sigma} + a^\dagger_{l\,\sigma}a_{2\,\sigma})$ we get, up to fourth order (up to second or third order there is no energy differentiation between singlet and triplet):

$$H^{\text{eff}}_{\text{VBCI}} = 4\left(\frac{t^2}{\Delta}\right)^2\left(\frac{1}{U} + \frac{2}{2\Delta + U'}\right)\hat{\mathbf{S}}_\mathbf{1}\hat{\mathbf{S}}_\mathbf{2}. \tag{2.3.16}$$

Eq. (2.3.16) is the original exchange expression found in Zaanen and Sawatzky [24], except for the ligand Coulomb repulsion U', which they did not take into account. The perturbational character of Eq. (2.3.16) requires that both $|\frac{t}{\Delta}|$ and $|\frac{t}{U}|$ are small enough to make the expansion converge and to ensure that the cutoff at fourth order is a valid approximation. The authors pointed out that whenever the transition metal compound is a charge-transfer insulator ($\Delta < U$), Eq. (2.3.16) is to be preferred to the Anderson expression [24]. Especially in the hypothetical case $U \to \infty$, Eq. (2.3.16) shows that there is still an antiferromagnetic interaction.

2.3.3 Comparison

We are now in a position to compare the different approximation schemes in a quantitative way. For this purpose the triplet-singlet exchange splitting is plotted as a function of the parameter t, which represents the metal-ligand hybridization interaction in the atomic basis. The exact exchange splitting is

calculated by exact diagonalization of the matrices (2.2.9) and (2.2.10). With regard to the Anderson approach, the original method only applied to the half filled magnetic orbitals on the metals, i.e., it did not consider the filled ligand orbital in the perturbation expressions. Still several ways of approximation are possible here. There is the purely kinetic part which ignores the first-order potential exchange ($H^{\mathrm{A}}_{\mathrm{And}}$), the potential plus the kinetic part ($H^{\mathrm{B}}_{\mathrm{And}}$) and the potential plus the kinetic plus the repulsion assisted part ($H^{\mathrm{C}}_{\mathrm{And}}$):

$$H^{\mathrm{A}}_{\mathrm{And}} = \frac{4b_{12}^2}{\tilde{U} - \tilde{K}_{12}} \hat{\mathbf{S}}_{\mathbf{1}} \hat{\mathbf{S}}_{\mathbf{2}} \tag{2.3.17}$$

$$H^{\mathrm{B}}_{\mathrm{And}} = \left[-2\tilde{J}_{12} + \frac{4b_{12}^2}{\tilde{U} - \tilde{K}_{12}} \right] \hat{\mathbf{S}}_{\mathbf{1}} \hat{\mathbf{S}}_{\mathbf{2}} \tag{2.3.18}$$

$$H^{\mathrm{C}}_{\mathrm{And}} = \left[-2\tilde{J}_{12} + \frac{4(b_{12} + \tilde{V}_{1222})^2}{\tilde{U} - \tilde{K}_{12}} \right] \hat{\mathbf{S}}_{\mathbf{1}} \hat{\mathbf{S}}_{\mathbf{2}}. \tag{2.3.19}$$

Higher forms, including the effect of the ligand orbital, are the perturbation up to complete second order: $H^{(1)} + H^{(2)}$ (Eqs. (2.3.13) and (2.3.14)) and likewise up to third, fourth, etc. order. Eq. (2.3.19) was also obtained by Hay, Thibeault and Hoffmann [30] using direct configuration interaction within A_1 and A_2 but they considered the repulsion assisted transfer term $\tilde{V}_{1222}$ unimportant, reducing the exchange expression to Eq. (2.3.18).

We are not concerned here with the application of the discussed theoretical approaches to real experimental cases, but merely want to compare them quantitatively as applied to one and the same model system. The parameters take values in arbitrary energy units.

Cases for which $|\frac{t}{\Delta}| \ll 1, |\frac{t}{U}| \ll 1$

In this region of parameters it is clear that the VBCI approximation of the exchange splitting Eq. (2.3.16) is valid. On the other hand it is not at once apparent how the Anderson-based expressions relate to the VBCI equation. An expansion of the elements of the Anderson equations, collecting terms of $(\frac{t^2}{\Delta})^2$ and neglecting higher powers, will clarify this situation. (U and U' are supposed to be of the same order of magnitude as Δ.) We get:

$$\frac{4b_{12}^2}{\tilde{U} - \tilde{K}_{12}} \approx 4 \left(\frac{t^2}{\Delta} \right)^2 \frac{(1 + \frac{U}{\Delta})^2}{U} = 4 \left(\frac{t^2}{\Delta} \right)^2 \left(\frac{1}{U} + \frac{2}{\Delta} + \frac{U}{\Delta^2} \right) \tag{2.3.20}$$

$$-2\tilde{J}_{12} + \frac{4b_{12}^2}{\tilde{U} - \tilde{K}_{12}} \approx 4 \left(\frac{t^2}{\Delta} \right)^2 \left(\frac{1}{U} + \frac{1}{\Delta} \left(1 - \frac{U'}{2\Delta} \right) + \frac{1}{\Delta} + \frac{3U}{4\Delta^2} \right) \tag{2.3.21}$$

$$-2\tilde{J}_{12} + \frac{4(b_{12} + \tilde{V}_{1222})^2}{\tilde{U} - \tilde{K}_{12}} \approx 4 \left(\frac{t^2}{\Delta} \right)^2 \left(\frac{1}{U} + \frac{1}{\Delta} \left(1 - \frac{U'}{2\Delta} \right) \right). \tag{2.3.22}$$

The last term in Eq. (2.3.22) is the first part of a Taylor expansion of $\frac{1}{\Delta(1+\frac{U'}{2\Delta})} = \frac{2}{2\Delta+U'}$. Therefore, $H^{\mathrm{C}}_{\mathrm{And}}$ is equivalent to the VBCI expression Eq. (2.3.16) for $\frac{U'}{2\Delta} \ll 1$. Now, we add the other second-order terms of Eq. (2.3.14). The second one is of the order $(\frac{t}{\Delta})^6$ and can be neglected. Addition of the third term of Eq. (2.3.14) to Eq. (2.3.22) yields exactly:

$$H^{(1)}_{\mathrm{And}} + H^{(2)}_{\mathrm{And}} \approx 4\left(\frac{t^2}{\Delta}\right)^2 \left(\frac{1}{U} + \frac{2}{2\Delta+U'}\right) \hat{\mathbf{S}}_{\mathbf{1}}\hat{\mathbf{S}}_{\mathbf{2}}, \tag{2.3.23}$$

which is just the VBCI expression Eq. (2.3.16). This shows that—for a relative small t—a second-order perturbation calculation based on the Anderson orbitals, including the metal-to-metal transfer and the double ligand-to-metal excitation, is equivalent to an atomic orbital based calculation including the same processes in fourth order of perturbation. By using a different approach, Geertsma has obtained a similar result [23]. The approximate expressions Eqs. (2.3.20) and (2.3.21) show that the "conventional" Anderson approach (that is, including only kinetic or kinetic and potential exchange ($H^{\mathrm{A}}_{\mathrm{And}}$ and $H^{\mathrm{B}}_{\mathrm{And}}$)) is only correct when $U, U' \ll \Delta$, which is not the case in most materials. We note that the term $\propto \frac{U}{\Delta^2}$, which cannot be considered small, comes in Eq. (2.3.20) via the transfer amplitude b_{12} (Eq. (2.B.7) and Table 2.1):

$$b_{12} \approx \frac{t^2}{\Delta}\left(1 + \frac{U}{\Delta}\right). \tag{2.3.24}$$

Zaanen and Sawatzky [24] discussed Eq. (2.3.16) as being composed of an Anderson term ($4\frac{(t^2/\Delta)^2}{U}$) and an additional term. They approximated $b_{12} \approx \frac{t^2}{\Delta}$. However, using the correct approximation in Eq. (2.3.24) we see that such a classification is not possible. Rather, one arrives at Eq. (2.3.16) through the inclusion of other Anderson terms, like $\tilde{J}_{12}$ and $\tilde{V}_{1222}$, which cancel the erroneous terms in Eq. (2.3.20). In this connection we want to emphasize the importance of the repulsion assisted transfer term $\tilde{V}_{1222}$ in the "modified" Anderson exchange Hamiltonian $H^{\mathrm{C}}_{\mathrm{And}}$. Consider the signs of b_{12} and $\tilde{V}_{1222}$. From the exact expression of $\tilde{V}_{1222}$ in Table 2.1, it can be derived that a necessary condition for $\tilde{V}_{1222}$ to be *positive* is: $U' > \frac{3}{2}U$. Because repulsion on the metal is always higher than that on the ligand, this condition is never satisfied and consequently $\tilde{V}_{1222}$ is always negative. At the same time, b_{12} is always positive.[2] $\tilde{V}_{1222}$ thus always lowers the magnitude of the conventional Anderson expressions and effectively reduces the condition for validity from $U, U' \ll \Delta$ to $U' \ll \Delta$, which is more reasonable as it may correspond to some physical reality. Inclusion of $\tilde{V}_{1222}$ in the Anderson theory thus removes the limitation $U \ll \Delta$, which was the main point of critique, eventually leading to the VBCI theory [24]. We

[2] See Eq. (2.B.7), where $\tilde{t}_{12}$ (Table 2.1) is always negative because $t\frac{c_1}{c_2}$ is always negative, as was mentioned in Section 2.3.1.

Table 2.1: Exact expressions of the matrix elements of the holes Hamiltonian (2.B.3) in the Anderson basis in terms of the orbital coefficients c_1 and c_2 and the model parameters t, Δ, U and U' and approximate expressions for $|\frac{t}{\Delta}| \ll 1$.

		Exact		Approximate
		c_1^2	$\approx$	$2(\frac{t}{\Delta})^2$
		c_2^2	$\approx$	1
		$c_1 c_2$	$\approx$	$-\sqrt{2}\frac{t}{\Delta}$
$\tilde{\Delta}$	$=$	$(c_2^2 - \frac{1}{2}c_1^2)\Delta - 3\sqrt{2}c_1c_2t$	$\approx$	Δ
$\tilde{t}_{12}$	$=$	$\frac{1}{2}(c_1^2\Delta + 2\sqrt{2}c_1c_2t) = \frac{1}{\sqrt{2}}t\frac{c_1}{c_2}$	$\approx$	$-\frac{t^2}{\Delta}$
$\tilde{t}_{1l}$	$=$	$(c_1^2 - c_2^2)t - \frac{1}{\sqrt{2}}c_1c_2\Delta$	$=$	0
$\tilde{U}$	$=$	$c_2^2U + \frac{1}{8}c_1^4(U + 2U')$	$\approx$	$U + (\frac{t}{\Delta})^4U'$
$\tilde{U}'$	$=$	$c_2^4U' + \frac{1}{2}c_1^4U$	$\approx$	$U' + 2(\frac{t}{\Delta})^4U$
$\tilde{K}_{12}$	$=$	$\frac{1}{8}c_1^4(U + 2U')$	$\approx$	$\frac{1}{2}(\frac{t}{\Delta})^4(U + 2U')$
$\tilde{K}_{1l}$	$=$	$\frac{1}{4}c_1^2((1 + c_2^2)U + 2c_2^2U')$	$\approx$	$(\frac{t}{\Delta})^2(U + U')$
$\tilde{J}_{12}$	$=$	$\frac{1}{8}c_1^4(U + 2U')$	$\approx$	$\frac{1}{2}(\frac{t}{\Delta})^4(U + 2U')$
$\tilde{J}_{1l}$	$=$	$\frac{1}{4}c_1^2((1 + c_2^2)U + 2c_2^2U')$	$\approx$	$(\frac{t}{\Delta})^2(U + U')$
$\tilde{V}_{1222}$	$=$	$-\frac{1}{4}c_1^2U + \frac{1}{8}c_1^4(U + 2U')$	$\approx$	$-\frac{1}{2}(\frac{t}{\Delta})^2(U - 2(\frac{t}{\Delta})^2U')$
$\tilde{V}_{1ll}$	$=$	$\frac{1}{2\sqrt{2}}c_1c_2(c_1^2U - 2c_2^2U')$	$\approx$	$\frac{t}{\Delta}\left(U' - (\frac{t}{\Delta})^2U\right)$
$\tilde{V}_{1l11}$	$=$	$\frac{1}{4\sqrt{2}}c_1c_2((3 + c_2^2)U - 2c_1^2U')$	$\approx$	$-\frac{t}{\Delta}\left(U - (\frac{t}{\Delta})^2U'\right)$
$\tilde{V}_{12l2}$	$=$	$-\frac{1}{4\sqrt{2}}c_1^3c_2(U + 2U')$	$\approx$	$\frac{1}{2}(\frac{t}{\Delta})^3(U + 2U')$
$\tilde{V}_{1l2l}$	$=$	$\frac{1}{4}c_1^2(-c_1^2U + 2c_2^2U')$	$\approx$	$(\frac{t}{\Delta})^2(U' - (\frac{t}{\Delta})^2U)$
$\tilde{V}_{122l}$	$=$	$-\frac{1}{4\sqrt{2}}c_1^3c_2(U + 2U')$	$\approx$	$\frac{1}{2}(\frac{t}{\Delta})^3(U + 2U')$
$\tilde{V}_{1ll2}$	$=$	$\frac{1}{4}c_1^2(-c_1^2U + 2c_2^2U')$	$\approx$	$(\frac{t}{\Delta})^2(U' - (\frac{t}{\Delta})^2U)$

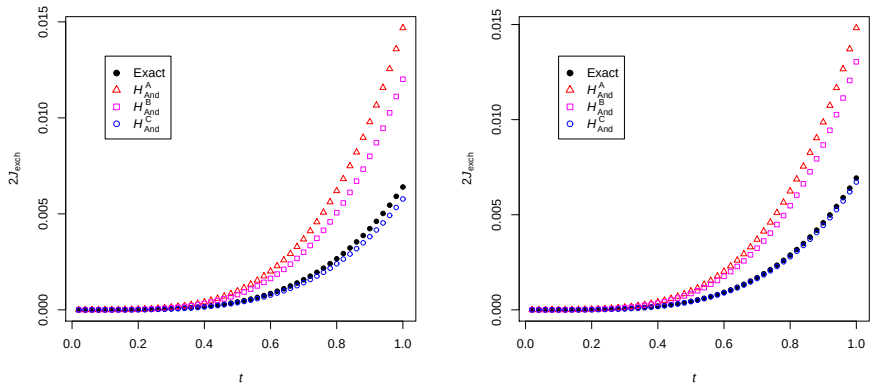

(a) $\Delta = 10$, $U = 10$, $U' = 10$ (b) $\Delta = 10$, $U = 10$, $U' = 5$

Figure 2.3: Exchange splittings as a function of t. The three Anderson based approaches are compared with the exact solution.

should note that the modified Anderson exchange $H^{\mathrm{C}}_{\mathrm{And}}$ retains the form of the conventional Anderson exchange $H^{\mathrm{B}}_{\mathrm{And}}$: by substituting $\beta_{12} = b_{12} + \tilde{V}_{1222}$ we have:

$$H^{\mathrm{C}}_{\mathrm{And}} = \left[-2\tilde{J}_{12} + \frac{4\beta_{12}^2}{\tilde{U} - \tilde{K}_{12}} \right] \hat{\mathbf{S}}_{\mathbf{1}} \hat{\mathbf{S}}_{\mathbf{2}}, \tag{2.3.25}$$

where we must keep in mind that β_{12} can be reduced considerably with respect to b_{12}. These findings are visualized in Fig. 2.3, where the three Anderson based approximations are plotted together with the exact exchange. The plot clearly shows that the conventional approximations $H^{\mathrm{A}}_{\mathrm{And}}$ and $H^{\mathrm{B}}_{\mathrm{And}}$ calculate the exchange splitting much too high, independent of t and U'. The modified form $H^{\mathrm{C}}_{\mathrm{And}}$ corrects this overestimation and gives good agreement with the exact exchange, even for $U' \approx \Delta$. Hence the usual assumption that $\tilde{V}_{1222}$ can be neglected [30] is not justified.

An interesting question is how variations of the system parameters affect the validity of the approaches. Consider for example the repulsion U on the metal ion. In the classical Anderson theory (Eqs. (2.3.20) and (2.3.21)), a—hypothetical—increase of U, at fixed Δ, would increase the exchange interaction, going to infinity for $U \to \infty$.[3] From the VBCI theory, however, we know that in the case of infinite Coulomb repulsion on the metal, a source of finite exchange is present in the form of a double ligand-to-metal excitation. In principle one

[3]This behavior really depends on the definition of the independent variable $\Delta = h_{11} + U - h_{ll} - U'$ (see Section 2.2). If $h_{11} - h_{ll}$ were held constant, then Δ grows with U and the exchange interaction would reach zero when $U \to \infty$.

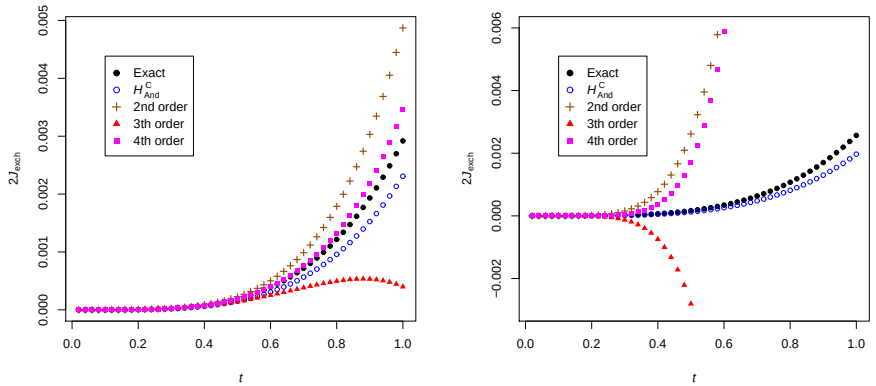

(a) $\Delta = 10$, $U = 100$, $U' = 10$ (b) $\Delta = 10$, $U = 1000$, $U' = 10$

Figure 2.4: Exchange splittings as a function of t for increased values of U. The modified Anderson exchange and complete second, third and fourth order perturbational approximations are compared with the exact solution.

might think that this effect could also be recovered in the Anderson theory by including the ligand orbital Ψ_{1+} in the perturbational calculation. This has indeed shown to successfully reproduce the VBCI expression: Eq. (2.3.23). However, when U grows further, some approximations used there are not valid anymore. It turns out that the Anderson orbitals do not provide a useful starting point for perturbation theory anymore, as can be seen in Fig. 2.4, where the complete second-, third-, and fourth-order perturbational approximations are plotted. The reason for this behavior is to be found in the composition of the Anderson orbitals. Each magnetic orbital contains a contribution on its neighboring metal site (cf. Eqs. (2.3.10) and (2.3.11)). One naturally expects this contribution to diminish with increasing U, so as to prevent two electrons from residing on the same metal site when their spins are paired. However, this does not happen with the Anderson orbitals: in Section 2.3.1 it was shown that they depend only on $\frac{t}{\Delta}$. Thus, a variation of U does not alter the orbitals at all. As a result, the first order energy of the singlet state increases with U while that of the triplet state is unaffected. Eventually this wrong-signed splitting reaches a point where perturbation theory cannot recover this anymore, as is apparent in Fig. 2.4. Note that the first order splitting equals $-2\tilde{J}_{12}$ (Eq. (2.3.13)) so that the discussed effect of U is totally contained in the exact expression of $\tilde{J}_{12}$ (Table 2.1). In general, it is not possible for the neighboring-ion contribution to vanish while still preserving the delocalization on the ligand, because of the orthogonality of the magnetic orbitals: the contribution on the

neighboring ion is essential to keep them orthogonal. Despite the fact that the Anderson orbitals are inappropriate for large U, the modified Anderson exchange $H^{\mathrm{C}}_{\mathrm{And}}$ still reproduces the exact exchange quite well (Fig. 2.4) because the approximation in Eq. (2.3.22) remains valid.

Cases for which $|\frac{t}{\Delta}| \ll 1$ is not valid

As was repeatedly pointed out [24, 26, 29, 31], the assumption $|\frac{t}{\Delta}| \ll 1$ is not generally valid. In fact, numerous examples exist where the ligand-metal energy gap Δ is known to be quite small or the metal-ligand hybridization element t to be rather large. In these cases we cannot rely on a Taylor series approximation of the orbital coefficients c_1 and c_2, as was done in Eq. (2.3.20) to (2.3.23). Instead, information will be inferred from plots.

In the previous section we saw that the conventional Anderson approaches (Eqs. (2.3.17) and (2.3.18)) always gave too high exchange interactions when $U \geq \Delta$. This situation is left unchanged for what is to come and we shall therefore not consider these approaches anymore, but focus on the VBCI exchange, the modified Anderson exchange $H^{\mathrm{C}}_{\mathrm{And}}$ and the Anderson-based perturbations up to fourth order. Both an increase of t as a decrease of Δ will be examined as well as the effect of varying U', since the Coulomb repulsion on the ligand can vary considerably according to the ligand's nature, though it will generally be smaller than U, which will be held constant as a reference energy.

A first series of plots is presented in Fig. 2.5, where Δ is lowered from left to right while U' is lowered from top to bottom. In the left column of Fig. 2.5, all approaches reproduce the exchange splitting very well because the conditions correspond with those discussed in the previous section: $|\frac{t}{\Delta}| \ll 1$, U and Δ are of the same order of magnitude, and U' is of the same order of magnitude or smaller than Δ. In the middle and the right columns of Fig. 2.5, the first condition is gradually less obeyed as Δ decreases. A first observation concerns the VBCI approach. As Δ decreases, the VBCI exchange behaves gradually more erroneously, calculating the exchange energy too high, obviously due to its perturbative nature with respect to $|\frac{t}{\Delta}|$. Note that the failure of VBCI is solely due to the increase of $|\frac{t}{\Delta}|$, independent of the value of U'.[4] This situation is different for the Anderson approaches: here, a lowering of Δ also has a negative influence on the quality of the approximation, as is most apparent in the first row of Fig. 2.5. However, lowering U' brings these approximations again closer to the exact solution. Consider for example the third column of Fig. 2.5, where $\Delta = 2$. When $U' = 10$, there is no agreement at all but on diminishing U' to 5 and 2, the Anderson approaches tend to get better and curiously, it's the

[4] In fact, for small Δ a lowering of U' makes the VBCI approximation even worse, as can be seen in the third column of Fig. 2.5.

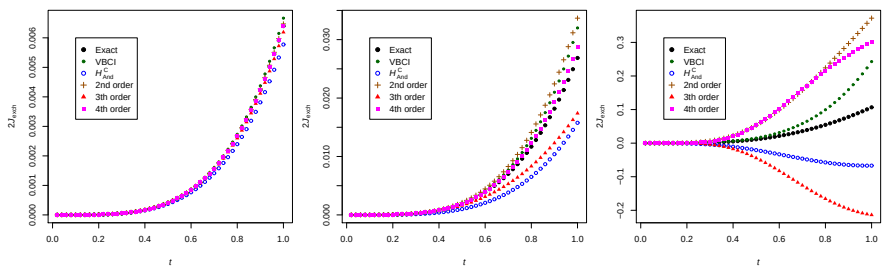

(a) $\Delta = 10$, $U = 10$, $U' = 10$ (b) $\Delta = 5$, $U = 10$, $U' = 10$ (c) $\Delta = 2$, $U = 10$, $U' = 10$

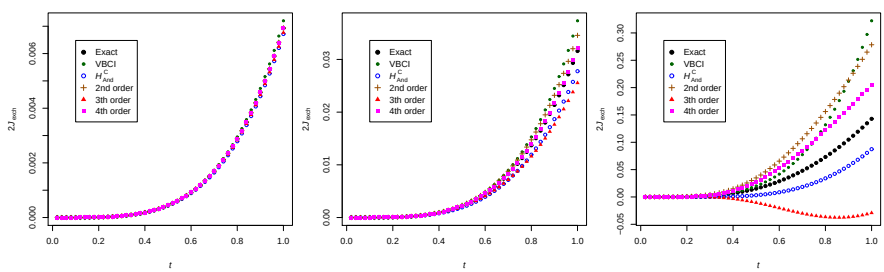

(d) $\Delta = 10$, $U = 10$, $U' = 5$ (e) $\Delta = 5$, $U = 10$, $U' = 5$ (f) $\Delta = 2$, $U = 10$, $U' = 5$

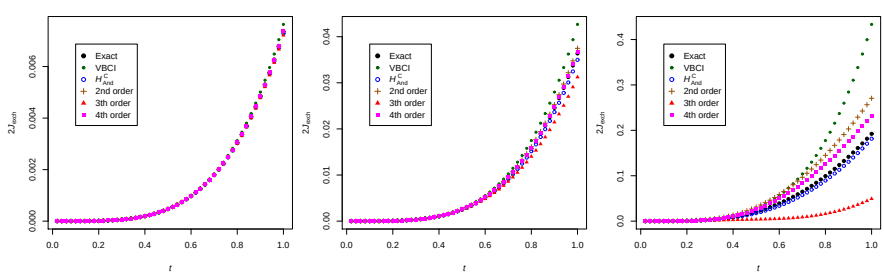

(g) $\Delta = 10$, $U = 10$, $U' = 2$ (h) $\Delta = 5$, $U = 10$, $U' = 2$ (i) $\Delta = 2$, $U = 10$, $U' = 2$

Figure 2.5: Exchange splittings as a function of t. The modified Anderson exchange and complete second, third and fourth order perturbational approximations are compared with VBCI and the exact solution. Values of Δ are varied per column. Values of U' are varied per row.

modified Anderson exchange $H^{\mathrm{C}}_{\mathrm{And}}$ which in the end gives closest correspondence to the exact solution: Fig. 2.5(i). One notices that even then, higher order corrections do not tend to converge to the exact solution, so that the success of $H^{\mathrm{C}}_{\mathrm{And}}$ is rather remarkable. This case resembles in a sense the one discussed in the previous section, where an increase of U was found to have a dramatic effect on the quality of the starting point configurations for perturbation theory in the Anderson approaches. Here again, only $\frac{t}{\Delta}$ determines the composition of the orbitals. When $|\frac{t}{\Delta}|$ increases, the magnetic orbitals get more delocalized onto the ligand and the neighboring metal. In the singlet state then, the wave function contains a contribution with the two holes paired on the ligand. If U' is relatively high, this contribution may increase the energy of this state to such an extent that perturbation theory is not capable anymore of correcting this. This analysis in terms of contributing configurations in the atomic basis essentially comes down to stating that the first order exchange splitting, $-2\tilde{J}_{12}$, or the potential exchange, increases as $|\frac{t}{\Delta}|$ and U' (and U) increase (see the exact expression for $\tilde{J}_{12}$ in Table 2.1), placing the triplet state at lowest energy, an error that must be corrected in the subsequent perturbational orders.

In this connection, we would like to mention that an unrestricted Hartree-Fock (UHF) calculation of the exchange energy in this model will also fail for relatively large U'. With UHF, the orbitals are seperataly optimized for the $M_S = 1$ and the broken symmetry $M_S = 0$ state. In the limit of large U', the magnetic orbitals of the latter state will be the pure atomic starting orbitals on the metals, i.e. without any delocalization on the ligand. The $M_S = 0$ state will therefore not gain energy. The solution for the $M_S = 1$ state, on the other hand, will be the same as the HF solution for this state, given in Section 2.3.1. Through bonding with the ligand, it will gain energy. The UHF calculation will therefore predict a ferromagnetic ground state in this case.

In Fig. 2.6 a series of plots is shown where the maximum value of t is set to 3. These are just extensions of the plots 2.5(a), 2.5(e), and 2.5(i). Again, we see that the VBCI curve is always too high, again due to the increase of $|\frac{t}{\Delta}|$. On the other hand, the Anderson approach behaves very well in Figs. 2.6(a) and 2.6(b), where especially the modified Anderson exchange $H^{\mathrm{C}}_{\mathrm{And}}$ is seen to nearly perfectly reproduce the exact exchange. Only in an extreme situation as in Fig. 2.6(c), the latter also fails, although it's still much better than VBCI. Clearly, the quality of the Anderson exchange is much less sensitive to an increase of t than to a decrease of Δ.

The previous examples, where the condition $|\frac{t}{\Delta}| \ll 1$ is not fulfilled, show the importance of a non-perturbative incorporation of the metal-ligand covalency, as in the Anderson HF orbitals, as opposed to a perturbative approach such as VBCI. Still there remain cases in which neither VBCI nor Anderson provides a satisfactory solution to the exchange problem.

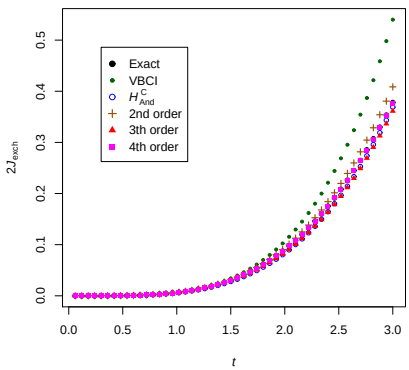

(a) $\Delta = 10$, $U = 10$, $U' = 10$

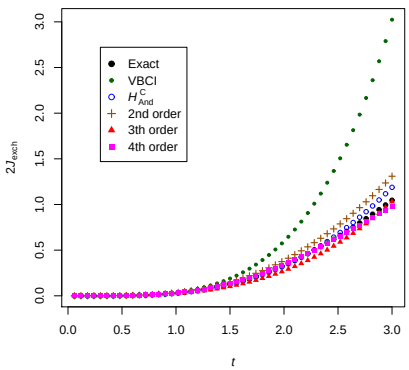

(b) $\Delta = 5$, $U = 10$, $U' = 5$

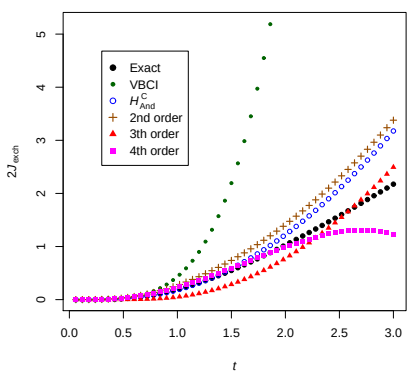

(c) $\Delta = 2$, $U = 10$, $U' = 2$

Figure 2.6: Exchange splittings as a function of t. The modified Anderson exchange and complete second, third and fourth order perturbational approximations are compared with VBCI and the exact solution, for extended values of t.

2.4 Exact treatment of the metal-ligand covalency

A physical theory that is to provide an insight into the origin of the magnetic interaction between centra, should ideally define a starting point where all important physical interactions are included except for those that differentiate between the relative spin direction of the magnetic electrons. The important effect to incorporate is the delocalization of each magnetic electron onto its neighboring ligand, an effect that is since long known to be essential for superexchange to occur. The purpose of the Anderson orbitals is indeed to incorporate this covalency via a HF type calculation. The choice of the ferromagnetic configuration as substrate for the HF calculation, as was done in Section 2.3.1, ensures that no exchange effects are included in the construction of the orbitals, because unpaired spins cannot reside on the same metal or ligand orbital. However, when these orbitals are used to construct the antiferromagnetic ground state, pairing of spins on the sites is allowed. As a result, the equivalence of starting points for the ferro- and antiferromagnetic states is broken. Under certain conditions, this may lead to a failure of the Anderson exchange, as discussed in the previous section. The VBCI approach treats the ferro- and antiferromagnetic state on equal footing in including the metal-ligand covalency but does so in a perturbative way. This works well if $|\frac{t}{\Delta}| \ll 1$ but inevitably leads to errors when this condition is not fulfilled.

Within the present model it is possible to obtain an exchange expression satisfying both requirements: metal-ligand covalency is treated exactly and magnetic exchange occurs in second order of perturbation. We start from the Hamiltonian matrices in the atomic basis (Eqs. (2.2.9) and (2.2.10)) and notice that the parts describing the interaction of the "ground" covalent state $|\mathrm{cov}; S\, M_S\rangle$ (Eqs. (2.2.3) and (2.2.7)), where each metal center is occupied by one hole, with the state $|\mathrm{l\,m}; S\, M_S\rangle$ (Eqs. (2.2.4) and (2.2.8)), where one hole is excited to the ligand site, are equal:

$$\begin{pmatrix} 0 & -\sqrt{2}t \\ & \Delta \end{pmatrix}.$$

On diagonalizing this matrix we obtain an exact inclusion of covalency that is equal for the triplet and singlet states. Note that this matrix is the same as the HF matrix (2.3.4) so that the solutions of the latter can be transferred to the present problem. The eigenstates are then:

$$|A; S\, M_S\rangle = c_2|\mathrm{cov}; S\, M_S\rangle - c_1|\mathrm{l\,m}; S\, M_S\rangle$$
$$|B; S\, M_S\rangle = c_1|\mathrm{cov}; S\, M_S\rangle + c_2|\mathrm{l\,m}; S\, M_S\rangle,$$

and the transformed Hamiltonian matrices:

$$H_{\text{alt}}^{{}^1\Gamma_+} = \begin{array}{c} \begin{array}{cccc} |A;0\,0\rangle & |B;0\,0\rangle & |\mathrm{m\,m};0\,0\rangle & |\mathrm{l\,l};0\,0\rangle \end{array} \\ \begin{pmatrix} \frac{\Delta}{2} - \sqrt{\left(\frac{\Delta}{2}\right)^2 + 2t^2} & 0 & -\sqrt{2}c_1 t & -2c_1 t \\ & \frac{\Delta}{2} + \sqrt{\left(\frac{\Delta}{2}\right)^2 + 2t^2} & -\sqrt{2}c_2 t & -2c_2 t \\ & & U & 0 \\ & & & 2\Delta + U' \end{pmatrix} \end{array}$$

$$H_{\text{alt}}^{{}^3\Gamma_-} = \begin{array}{c} \begin{array}{cc} |A;1\,1\rangle & |B;1\,1\rangle \end{array} \\ \begin{pmatrix} \frac{\Delta}{2} - \sqrt{\left(\frac{\Delta}{2}\right)^2 + 2t^2} & 0 \\ & \frac{\Delta}{2} + \sqrt{\left(\frac{\Delta}{2}\right)^2 + 2t^2} \end{pmatrix} \end{array},$$

with c_1 and c_2 as in Eqs. (2.3.8) and (2.3.9). The singlet and triplet ground states have the same starting point energy: $\frac{\Delta}{2} - \sqrt{\left(\frac{\Delta}{2}\right)^2 + 2t^2}$. With $|A;S\,M_S\rangle$ we have constructed a state in which the holes are delocalized over the metal and ligand sites but are never allowed to pair on the same site. It is thus a *purely covalent* starting point. Note that for the triplet state, this starting point is the same as the one obtained in the Anderson HF calculation. Indeed, parallel spins automatically exclude each other from the same site. For the singlet state, on the other hand, the present starting point cannot be described as a single configuration. As a result of the transformation, the ground state of $H_{\text{alt}}^{{}^1\Gamma_+}$ has now a direct matrix element with the third and fourth basis states, viz. $|\mathrm{m\,m};0\,0\rangle$ and $|\mathrm{l\,l};0\,0\rangle$. These interactions are absent in $H_{\text{alt}}^{{}^3\Gamma_-}$ and thus provide the path for exchange interaction, which is already obtained in second order of perturbation:

$$\begin{aligned} H_{\text{alt}}^{\text{eff}} &= 2t^2c_1^2 \left(\frac{1}{U - \left(\frac{\Delta}{2} - \sqrt{\left(\frac{\Delta}{2}\right)^2 + 2t^2}\right)} \right. \\ &\qquad \left. + \frac{2}{2\Delta + U' - \left(\frac{\Delta}{2} - \sqrt{\left(\frac{\Delta}{2}\right)^2 + 2t^2}\right)} \right) \hat{\mathbf{S}}_\mathbf{1}\hat{\mathbf{S}}_\mathbf{2} \\ &= 2t^2c_1^2 \left(\frac{1}{U - \sqrt{2}t\frac{c_1}{c_2}} + \frac{2}{2\Delta + U' - \sqrt{2}t\frac{c_1}{c_2}} \right) \hat{\mathbf{S}}_\mathbf{1}\hat{\mathbf{S}}_\mathbf{2}. \end{aligned} \tag{2.4.1}$$

This equation is very similar to the VBCI equation Eq. (2.3.16) and reduces to the latter if $|\frac{t}{\Delta}| \ll 1$ and $|\frac{t}{U}| \ll 1$. $H_{\text{alt}}^{\text{eff}}$ is however not restricted by a limitation on the value of $|\frac{t}{\Delta}|$, as was the VBCI equation, nor will it fail when U or U' are too large, as was the case with the Anderson approach.

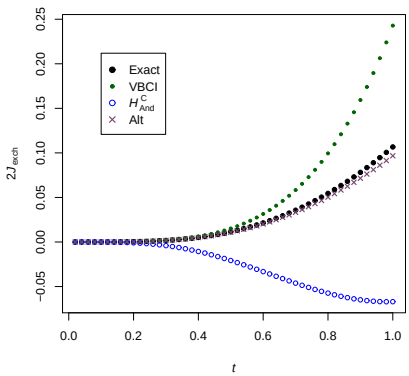

(a) $\Delta = 2$, $U = 10$, $U' = 10$

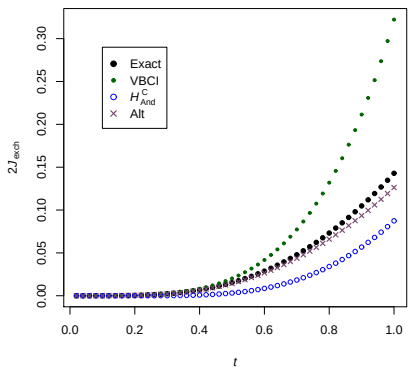

(b) $\Delta = 2$, $U = 10$, $U' = 5$

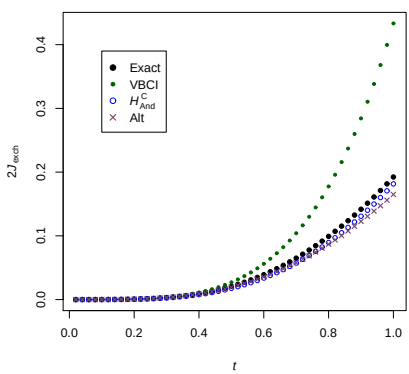

(c) $\Delta = 2$, $U = 10$, $U' = 2$

Figure 2.7: Exchange splittings as a function of t. The modified Anderson exchange and VBCI are compared with the alternative exchange and the exact solution.

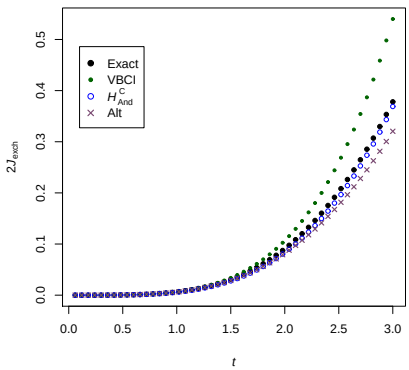

(a) $\Delta = 10$, $U = 10$, $U' = 10$

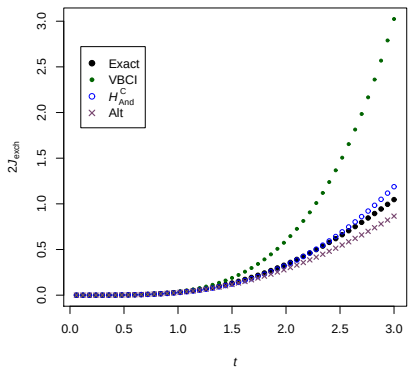

(b) $\Delta = 5$, $U = 10$, $U' = 5$

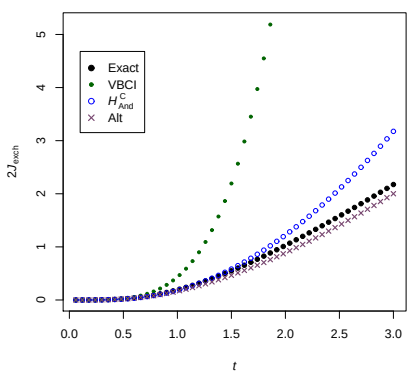

(c) $\Delta = 2$, $U = 10$, $U' = 2$

Figure 2.8: Exchange splittings as a function of t. The modified Anderson exchange and VBCI are compared with the alternative exchange and the exact solution, for extended values of t.

Figures 2.7 and 2.8 present some plots of conditions that were found to be problematic for VBCI, Anderson, or both. The present approach has been included, in comparison with VBCI, the modified Anderson and the exact solution. The plots in Fig. 2.7 represent the case of small Δ and correspond to the third column of Fig. 2.5. Especially in Fig. 2.7(a) the present approach is seen to be capable of dealing with a situation in which VBCI and Anderson are unsuccessful. Only in Fig. 2.7(c) the modified Anderson exchange comes closer to the exact solution. Larger values of t are considered in Fig. 2.8 with plots corresponding to Fig. 2.6(a), 2.6(b) and 2.6(c). Overall, the new approach proves to be versatile in treating the exchange problem in a broad range of situations.

How stable is the second order perturbational expression Eq. (2.4.1)? In analogy with VBCI one might expect that it would diverge for large t or small U, U', or Δ. This is however not the case; it can be shown that the perturbational fractions are, in absolute value, always smaller than 1:

$$\frac{\sqrt{2}|c_1 t|}{U - \sqrt{2}t\frac{c_1}{c_2}} < 1$$
$$\frac{2|c_1 t|}{2\Delta + U' - \sqrt{2}t\frac{c_1}{c_2}} < 1,$$

for $\Delta, U, U', |t| > 0$. This means that the perturbational expansion is always valid and explains why, for example, this second order exchange expression does never diverge from the exact solution, as can be clearly seen in Fig. 2.8(c).

2.5 Conclusion

We have investigated the application of the Anderson and the VBCI theories to a basic exchange model, in which the ground state is always antiferromagnetic. The Anderson orbitals can be obtained exactly, allowing us to compare both methods quantitatively. A first, and remarkable, observation is that the original Anderson exchange expression, including only the kinetic transfer b_{12} and the potential exchange $\tilde{J}_{12}$, is not an accurate approximation if the rather unphysical condition $U \ll \Delta$ is not fullfilled, even in the most well-behaved situations (Fig. 2.3). The reason is that the often disregarded "repulsion assisted transfer" term $\tilde{V}_{1222}$ is not negligible with respect to b_{12}. Inclusion of the former indeed removes the mentioned restricting condition while the form of the original Anderson expression is preserved: Eq. (2.3.25). We have discussed the importance of the on-site metal and ligand Coulomb repulsions U and U' for the reliability of the Anderson method. The composition of the Anderson orbitals does not depend on U or U'. For relatively high values of these parameters, the

Anderson ground configurations are not valid starting points for perturbation theory anymore, because the first-order energy of the singlet state is raised too much above the triplet energy. The VBCI method is reliable for systems with weak metal-ligand covalency, i.e. $|\frac{t}{\Delta}| \ll 1$. Whenever this is not the case, it fails due to its perturbational description of covalency. In some of these cases, the Anderson method, incorporating the metal-ligand covalency in a variational way in its orbitals, may prove more succesfull, although this again depends on the relative magnitude of U and U'. To overcome the problems of both methods, we have suggested that the metal-ligand covalency be incorporated exactly in the starting point wave functions followed by a second-order evaluation of the exchange effects. This way, we obtained an exchange expression that does not suffer from any restricting condition on the model parameters.

2.A Derivation of the Hartree-Fock orbitals

It is not immediately obvious that a HF treatment of the triplet state in the hole representation is completely equivalent to a ROHF treatment of the same state in the electron representation. In the electron case, a restriction is imposed upon the doubly occupied orbital, namely that it have the same spatial part for both spin up and spin down. In the hole case, on the other hand, there are no paired holes and a similar restriction seems to be absent. In the following it will be explicitly shown that the obtained HF orbitals are nevertheless identical.

The ground $^3\Gamma_-$ state is written in the electron representation:

$$|\mathrm{cov};1\,1\rangle = |\Psi_{2+}\Psi_{-}\Psi_{1+}\overline{\Psi}_{1+}|.$$

Symmetry restrictions and mutual orthonormality require the molecular orbitals to be of the form:

$$\Psi_{1+} = a_1\phi_+ + a_2\phi_l \qquad \Psi_- = \phi_- \qquad \Psi_{2+} = a_2\phi_+ - a_1\phi_l, \tag{2.A.1}$$

with $a_1^2 + a_2^2 = 1$. Finding the HF orbitals means minimizing the energy of $|\mathrm{cov};1\,1\rangle$ with respect to a_1 and a_2. Using Hamiltonian (2.2.1) for electrons and the identity $a_1^2 + a_2^2 = 1$ we find:

$$E = \langle \mathrm{cov};1\,1|H|\mathrm{cov};1\,1\rangle = 2h_{11} + h_{ll} + a_1^2 h_{11} + a_2^2 h_{ll} + 2\sqrt{2}a_1a_2t + a_1^2U + a_2^2U'. \tag{2.A.2}$$

Stationary points on the unit circle ($a_1^2 + a_2^2 = 1$) obey the equations:

$$\frac{\partial E}{\partial a_i} - \lambda\frac{\partial}{\partial a_i}(a_1^2 + a_2^2) = 0, \qquad \text{with} \quad i = 1, 2. \tag{2.A.3}$$

Applying (2.A.3) to (2.A.2) gives:

$$\begin{pmatrix} h_{11}+U-\lambda & \sqrt{2}t \\ \sqrt{2}t & h_{ll}+U'-\lambda \end{pmatrix} \begin{pmatrix} a_1 \\ a_2 \end{pmatrix} = \begin{pmatrix} 0 \\ 0 \end{pmatrix}, \tag{2.A.4}$$

or, setting $\lambda' = -\lambda + h_{11} + U$, using $\Delta = h_{11} + U - h_{ll} - U'$ and changing the overall sign:

$$\begin{pmatrix} -\lambda' & -\sqrt{2}t \\ -\sqrt{2}t & \Delta - \lambda' \end{pmatrix} \begin{pmatrix} a_1 \\ a_2 \end{pmatrix} = \begin{pmatrix} 0 \\ 0 \end{pmatrix}.$$

This eigenvalue equation is exactly the same as the eigenvalue equation of the HF matrix for the holes (Eq. (2.3.4)). There are thus two solutions: $(a_1, a_2, \lambda') = (c_1, c_2, -\sqrt{2}t\frac{c_2}{c_1})$ and $(a_1, a_2, \lambda') = (c_2, -c_1, \sqrt{2}t\frac{c_1}{c_2})$, with c_1 and c_2 as in Eqs. (2.3.8) and (2.3.9). To determine which one corresponds to the lowest energy, we multiply Eq. (2.A.4) in front with $\begin{pmatrix} a_1 & a_2 \end{pmatrix}$ and get:

$$a_1^2 h_{11} + a_1^2 U + a_2^2 h_{22} + a_2^2 U' + 2\sqrt{2}a_1 a_2 t = \lambda.$$

Using Eq. (2.A.2) this gives:

$$E = 2h_{11} + h_{ll} + \lambda = 3h_{11} + h_{ll} + U - \lambda'. \tag{2.A.5}$$

From Eq. (2.A.5) and the fact that $t\frac{c_2}{c_1}$ is always negative we conclude that the solution $(a_1, a_2, \lambda') = (c_1, c_2, -\sqrt{2}t\frac{c_2}{c_1})$ corresponds to the sought energy minimum of $|\mathrm{cov}; 1\,1\rangle$. Thus, the ROHF molecular orbitals in Eq. (2.A.1) are exactly equal to the HF orbitals in Eqs. (2.3.5), (2.3.6) and (2.3.7), found for the hole representation.

2.B Hamiltonian for holes in an Anderson-like basis $\{1, 2, l\}$

If an orthogonal transformation of the (real) orbitals of a general Hamiltonian

$$H = \sum_{i,j,\sigma} t_{ij} a^\dagger_{i\,\sigma} a_{j\,\sigma} + \frac{1}{2} \sum_{i,j,k,l} V_{ijkl} \sum_{\sigma,\sigma'} a^\dagger_{i\,\sigma} a^\dagger_{j\,\sigma'} a_{l\,\sigma'} a_{k\,\sigma} \tag{2.B.1}$$

is applied: $b_p = \sum_i c_{ip} a_i$ and $b^\dagger_p = \sum_i c_{ip} a^\dagger_i$, the Hamiltonian (2.B.1) transforms to:

$$H = \sum_{p,q,\sigma} \tilde{t}_{pq} b^\dagger_{p\,\sigma} b_{q\,\sigma} + \frac{1}{2} \sum_{p,q,r,s} \tilde{V}_{pqrs} \sum_{\sigma,\sigma'} b^\dagger_{p\,\sigma} b^\dagger_{q\,\sigma'} b_{s\,\sigma'} b_{r\,\sigma},$$

where

$$\tilde{t}_{pq} = \sum_{i,j} c_{ip} c_{jq} t_{ij}, \qquad \tilde{V}_{pqrs} = \sum_{i,j,k,l} c_{ip} c_{jq} c_{kr} c_{ls} V_{ijkl} \tag{2.B.2}$$

are the matrix elements in the new basis. For a general set of three localized orbitals in the present model, and thus in particular for the Anderson orbitals, the Hamiltonian (2.2.2) can therefore be written as:

$$
\begin{aligned}
H^{\text{holes}} = &\sum_{\sigma}\Big[\tilde{\Delta} n_{l\,\sigma} + \frac{1}{2}\tilde{U}' n_{l\,\sigma} n_{l\,-\sigma} + \frac{1}{2}\tilde{U}(n_{1\,\sigma}n_{1\,-\sigma} + n_{2\,\sigma}n_{2\,-\sigma})\Big] \\
&+ \sum_{\sigma,\sigma'}\Big[\tilde{K}_{1l}(n_{1\,\sigma}n_{l\,\sigma'} + n_{2\,\sigma}n_{l\,\sigma'}) + \tilde{K}_{12} n_{1\,\sigma} n_{2\,\sigma'}\Big] \\
&+ \sum_{\sigma}\Big[\tilde{t}_{1l}(b^{\dagger}_{1\,\sigma}b_{l\,\sigma} + b^{\dagger}_{l\,\sigma}b_{1\,\sigma} + b^{\dagger}_{2\,\sigma}b_{l\,\sigma} + b^{\dagger}_{l\,\sigma}b_{2\,\sigma}) + \tilde{t}_{12}(b^{\dagger}_{1\,\sigma}b_{2\,\sigma} + b^{\dagger}_{2\,\sigma}b_{1\,\sigma})\Big] \\
&+ \sum_{\sigma,\sigma'}\Big[-\tilde{J}_{1l}(b^{\dagger}_{1\,\sigma}b_{1\,\sigma'}b^{\dagger}_{l\,\sigma'}b_{l\,\sigma} + b^{\dagger}_{2\,\sigma}b_{2\,\sigma'}b^{\dagger}_{l\,\sigma'}b_{l\,\sigma}) - \tilde{J}_{12}b^{\dagger}_{1\,\sigma}b_{1\,\sigma'}b^{\dagger}_{2\,\sigma'}b_{2\,\sigma}\Big] \\
&+ \tilde{V}_{11ll}(b^{\dagger}_{1\,\sigma}b^{\dagger}_{1\,-\sigma}b_{l\,-\sigma}b_{l\,\sigma} + b^{\dagger}_{2\,\sigma}b^{\dagger}_{2\,-\sigma}b_{l\,-\sigma}b_{l\,\sigma} + b^{\dagger}_{l\,\sigma}b^{\dagger}_{l\,-\sigma}b_{1\,-\sigma}b_{1\,\sigma} \\
&+ b^{\dagger}_{l\,\sigma}b^{\dagger}_{l\,-\sigma}b_{2\,-\sigma}b_{2\,\sigma}) + \tilde{V}_{1122}(b^{\dagger}_{1\,\sigma}b^{\dagger}_{1\,-\sigma}b_{2\,-\sigma}b_{2\,\sigma} + b^{\dagger}_{2\,\sigma}b^{\dagger}_{2\,-\sigma}b_{1\,-\sigma}b_{1\,\sigma}) \\
&+ \sum_{\sigma}\Big[(b^{\dagger}_{1\,\sigma}b_{l\,\sigma} + b^{\dagger}_{l\,\sigma}b_{1\,\sigma})\left(\tilde{V}_{1ll}n_{l\,-\sigma} + \tilde{V}_{l111}n_{1\,-\sigma} + \tilde{V}_{12l2}n_2\right) \\
&\quad + (b^{\dagger}_{2\,\sigma}b_{l\,\sigma} + b^{\dagger}_{l\,\sigma}b_{2\,\sigma})\left(\tilde{V}_{1ll}n_{l\,-\sigma} + \tilde{V}_{l111}n_{2\,-\sigma} + \tilde{V}_{12l2}n_1\right) \\
&\quad + (b^{\dagger}_{1\,\sigma}b_{2\,\sigma} + b^{\dagger}_{2\,\sigma}b_{1\,\sigma})\left(\tilde{V}_{1222}(n_{2\,-\sigma} + n_{1\,-\sigma}) + \tilde{V}_{1l2l}n_l\right)\Big] \\
&+ \sum_{\sigma,\sigma'}\Big[\tilde{V}_{122l}(b^{\dagger}_{l\,\sigma}b^{\dagger}_{2\,\sigma'}b_{1\,\sigma'}b_{2\,\sigma} + b^{\dagger}_{1\,\sigma}b^{\dagger}_{2\,\sigma'}b_{l\,\sigma'}b_{2\,\sigma} + b^{\dagger}_{l\,\sigma}b^{\dagger}_{1\,\sigma'}b_{2\,\sigma'}b_{1\,\sigma} \\
&\quad + b^{\dagger}_{2\,\sigma}b^{\dagger}_{1\,\sigma'}b_{l\,\sigma'}b_{1\,\sigma}) + \tilde{V}_{1ll2}(b^{\dagger}_{1\,\sigma}b^{\dagger}_{l\,\sigma'}b_{2\,\sigma'}b_{l\,\sigma} + b^{\dagger}_{2\,\sigma}b^{\dagger}_{l\,\sigma'}b_{1\,\sigma'}b_{l\,\sigma})\Big] \\
&+ \sum_{\sigma}\Big[\tilde{V}_{122l}(b^{\dagger}_{2\,\sigma}b^{\dagger}_{2\,-\sigma}b_{l\,-\sigma}b_{1\,\sigma} + b^{\dagger}_{1\,\sigma}b^{\dagger}_{l\,-\sigma}b_{2\,-\sigma}b_{2\,\sigma} + b^{\dagger}_{1\,\sigma}b^{\dagger}_{1\,-\sigma}b_{l\,-\sigma}b_{2\,\sigma} \\
&\quad + b^{\dagger}_{2\,\sigma}b^{\dagger}_{l\,-\sigma}b_{1\,-\sigma}b_{1\,\sigma}) + \tilde{V}_{1ll2}(b^{\dagger}_{l\,\sigma}b^{\dagger}_{l\,-\sigma}b_{2\,-\sigma}b_{1\,\sigma} + b^{\dagger}_{2\,\sigma}b^{\dagger}_{2\,-\sigma}b_{l\,-\sigma}b_{l\,\sigma})\Big].
\end{aligned}
\tag{2.B.3}
$$

In Eq. (2.B.3) the $\tilde{V}_{ijkl}$ are the repulsion elements $\propto \langle i(1)j(2)|\frac{1}{r_{12}}|k(1)l(2)\rangle$. $\tilde{K}_{ij}$ and $\tilde{J}_{ij}$ stand for $\tilde{V}_{ijij}$ and $\tilde{V}_{ijji}$, respectively. The symmetry of the system (orbitals 1 and 2 are equivalent and interact identically with l) has been applied to reduce the number of different matrix elements in (2.B.3). (Note that $\tilde{V}_{11ll} = \tilde{V}_{1ll1} \equiv \tilde{J}_{1l}$ and the same for $\tilde{V}_{1122}$ but this substitution is not carried through for clarity.) The expressions for the matrix elements in the Hamiltonian (2.B.3) according to the transformation equations in (2.B.2) are listed in Table 2.1, along with approximate expressions for $|\frac{t}{\Delta}| \ll 1$. Note that $\tilde{t}_{1l}$ is exactly zero in the Anderson basis since it is an off-diagonal matrix element of the HF operator.

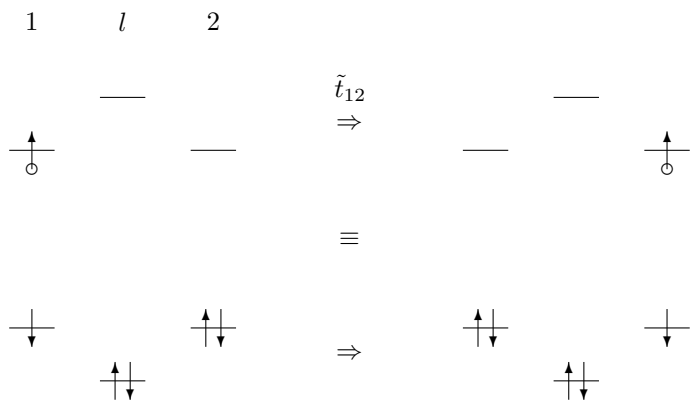

Figure 2.9: Schematic representation of the one-hole transfer process (upper part) and its equivalent electron transfer process (lower part). The orbitals on the centra 1, l and 2 are A_1, Ψ_{1+} and A_2 in Eqs. (2.3.10), (2.3.5) and (2.3.11), respectively.

We want to relate the one-hole transfer element $\tilde{t}_{12}$ of Hamiltonian (2.B.3) to the one-electron "kinetic transfer" integral b_{12} [1]. By its definition, $\tilde{t}_{12}$ is the matrix element of the Hamiltonian (2.B.3) between two one-hole configurations: one with the hole in the first Anderson magnetic orbital and the other with the hole in the second Anderson magnetic orbital, as depicted in the upper part of Fig. 2.9. The lower part of Fig. 2.9 represents exactly the same configurations in terms of electrons. The fact that a hole creation operator is actually defined as being exactly equal to an electron annihilation operator ensures that the phase relationship between electron configurations is unambiguously defined. Thus, if the first hole configuration in Fig. 2.9 is written as $b_{1\uparrow}|0_h\rangle$ and the second as $b_{2\uparrow}|0_h\rangle$ then the expressions for the corresponding electron configurations are found by writing out $|0_h\rangle$ in terms of electron occupation. If we choose $|0_h\rangle \equiv b^\dagger_{1\uparrow}b^\dagger_{1\downarrow}b^\dagger_{2\uparrow}b^\dagger_{2\downarrow}b^\dagger_{l\uparrow}b^\dagger_{l\downarrow}|0_e\rangle$, we have:

$$\begin{aligned} b_{1\uparrow}|0_h\rangle &\equiv b^\dagger_{1\downarrow}b^\dagger_{2\uparrow}b^\dagger_{2\downarrow}b^\dagger_{l\uparrow}b^\dagger_{l\downarrow}|0_e\rangle = -b^\dagger_{2\uparrow}b^\dagger_{1\downarrow}b^\dagger_{2\downarrow}b^\dagger_{l\uparrow}b^\dagger_{l\downarrow}|0_e\rangle \\ b_{2\uparrow}|0_h\rangle &\equiv b^\dagger_{1\uparrow}b^\dagger_{1\downarrow}b^\dagger_{2\downarrow}b^\dagger_{l\uparrow}b^\dagger_{l\downarrow}|0_e\rangle, \end{aligned} \tag{2.B.4}$$

Taking the Hamiltonian matrix elements between both states at the same side of Eq. (2.B.4) we find:

$$\tilde{t}_{12} = -(\tilde{F}^c_{12} + 2\tilde{V}_{1222} + 2\tilde{V}_{1l2l} - \tilde{V}_{1ll2}). \tag{2.B.5}$$

On the other hand, the Anderson parameter b_{12} is the matrix element for the transfer of one electron between the metal sites in the field of the diamagnetic lattice, as depicted in Fig. 2.10. Therefore,

$$b_{12} = \tilde{F}^c_{12} + 2\tilde{V}_{1l2l} - \tilde{V}_{1ll2}. \tag{2.B.6}$$

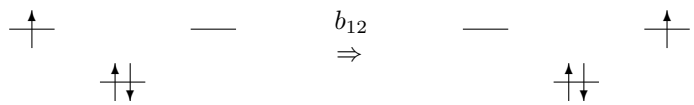

Figure 2.10: Schematic representation of the electron transfer process with matrix element b_{12}. The orbitals on the centra 1, l and 2 are A_1, Ψ_{1+} and A_2 in Eqs. (2.3.10), (2.3.5) and (2.3.11), respectively.

From Eqs. (2.B.5) and (2.B.6),

$$b_{12} = -(\tilde{t}_{12} + 2\tilde{V}_{1222}), \tag{2.B.7}$$

as used in Eq. (2.3.15).

2.C Evaluation of the perturbational exchange energy

In calculating the exchange energy in the Anderson approach to a certain order of perturbation, one can follow two procedures. The first consists of separately calculating the perturbational energies of the lowest triplet and singlet state and substracting one from the other. The second one makes use of an effective perturbation Hamiltonian that acts in the ground manifold, i.e. in the configurations with one hole in each magnetic orbital. This method is more convenient as it can easily be extended to systems with an unspecified number of magnetic centers. We have used the latter procedure to obtain exchange expressions up to fourth order, which are used in the plots. This appendix discusses some details of this procedure.

As was mentioned in the text, the Hamiltonian in Eq. (2.B.3) is split in two parts: $H^{\text{holes}} = H^0 + H'$, where H^0 consists of the first two lines of Eq. (2.B.3) and H' of the rest. The components of the effective perturbation Hamiltonian are then as specified in Eq. (2.3.12). The projection operators can be written out explicitly for the present model:

$$P_0 = \sum_{\sigma,\sigma'} n_{1\,\sigma} n_{2\,\sigma'}$$

$$\frac{P}{a^n} = \sum_{i=1}^{2} \left[\frac{n_{i\,\sigma} n_{i\,-\sigma}}{(\tilde{K}_{12} - \tilde{U})^n} + \sum_{\sigma,\sigma'} \frac{n_{i\,\sigma} n_{l\,\sigma'}}{(\tilde{K}_{12} - \tilde{\Delta} - \tilde{K}_{1l})^n} \right] + \frac{n_{l\,\sigma} n_{l\,-\sigma}}{(\tilde{K}_{12} - 2\tilde{\Delta} - \tilde{U}')^n},$$

with $n_{i\,\sigma} = b^{\dagger}_{i\,\sigma} b_{i\,\sigma}$. The expressions in Eq. (2.3.12) consist then of strings of creation and annihilation operators. Such strings of every length can however always be simplified to a maximum length of four using the anticommutation rules and the fact that in the ground manifold, one hole occupies each magnetic orbital. The resulting operators are connected with the on-site spin operators through the relation [1, 22]

$$\sum_{\sigma,\sigma'} b^{\dagger}_{1\,\sigma} b_{1\,\sigma'} b^{\dagger}_{2\,\sigma'} b_{2\,\sigma} = 2\hat{\mathbf{S}}_{\mathbf{1}}\hat{\mathbf{S}}_{\mathbf{2}} + \frac{1}{2}.$$

In the final exchange Hamiltonian, constant terms are discarded as they do not contribute to the relative energy splitting. We can also see here that the effective perturbation Hamiltonians in Eq. (2.3.12) do not need to be made Hermitian explicitly because they all simplify to the form $\hat{\mathbf{S}}_{\mathbf{1}}\hat{\mathbf{S}}_{\mathbf{2}}$, which is Hermitian. The first and second order exchange Hamiltonians were given in the text in Eqs. (2.3.13) and (2.3.14). For the third order we find:

$$\begin{aligned}
P_0 H' \frac{P}{a} H' \frac{P}{a} H' P_0 = -4\Bigg(& \frac{\tilde{V}_{1122}(\tilde{t}_{12} + \tilde{V}_{1222})^2}{(\tilde{U} - \tilde{K}_{12})^2} \\
& + \frac{2(\tilde{t}_{1l} + \tilde{V}_{122l} + \tilde{V}_{12l2})\tilde{V}_{1ll2}(\tilde{t}_{1l} + \tilde{V}_{1ll})}{(\tilde{\Delta} + \tilde{K}_{1l} - \tilde{K}_{12})(2\tilde{\Delta} + \tilde{U}' - \tilde{K}_{12})} + \frac{2\tilde{V}_{11ll}(\tilde{t}_{12} + \tilde{V}_{1222})\tilde{V}_{1ll2}}{(\tilde{U} - \tilde{K}_{12})(2\tilde{\Delta} + \tilde{U}' - \tilde{K}_{12})} \\
& + \frac{2(\tilde{t}_{12} + \tilde{V}_{1222})(\tilde{t}_{1l} + \tilde{V}_{122l} + \tilde{V}_{12l2})(\tilde{t}_{1l} + \tilde{V}_{122l} + \tilde{V}_{l111})}{(\tilde{U} - \tilde{K}_{12})(\tilde{\Delta} + \tilde{K}_{1l} - \tilde{K}_{12})} \\
& + \frac{\left(\tilde{V}^2_{122l} + (\tilde{t}_{1l} + \tilde{V}_{12l2})^2\right)(\tilde{t}_{12} + \tilde{V}_{1l2l} + \tilde{J}_{1l}) + 2\tilde{V}_{122l}(\tilde{t}_{1l} + \tilde{V}_{12l2})\tilde{V}_{1ll2}}{(\tilde{\Delta} + \tilde{K}_{1l} - \tilde{K}_{12})^2} \Bigg)\hat{\mathbf{S}}_{\mathbf{1}}\hat{\mathbf{S}}_{\mathbf{2}}
\end{aligned} \tag{2.C.1a}$$

$$\begin{aligned}
P_0 H' P_0 H' \frac{P}{a^2} H' P_0 = -2\tilde{J}_{12}\Bigg(& \frac{2(\tilde{t}_{12} + \tilde{V}_{1222})^2}{(\tilde{U} - \tilde{K}_{12})^2} \\
& + \frac{2\left(\tilde{V}^2_{122l} + (\tilde{t}_{1l} + \tilde{V}_{12l2})^2\right)}{(\tilde{\Delta} + \tilde{K}_{1l} - \tilde{K}_{12})^2} + \frac{\tilde{V}^2_{1ll2}}{(2\tilde{\Delta} + \tilde{U}' - \tilde{K}_{12})^2} \Bigg)\hat{\mathbf{S}}_{\mathbf{1}}\hat{\mathbf{S}}_{\mathbf{2}}
\end{aligned} \tag{2.C.1b}$$

In a similar way, one can obtain the lengthy fourth-order exchange expressions.[5]

Bibliography

[1] P. W. Anderson, Phys. Rev. **115**, 2 (1959)

[5] See Addendum A for the complete fourth-order exchange expressions.

[2] W. Geertsma, Physica B **212**, 50 (1995)

[3] W. Geertsma, J. Magn. Magn. Mater. **151**, 67 (1995)

[4] W. Koshibae, Y. Ohta, and S. Maekawa, Phys. Rev. B **50**, 3767 (1994)

[5] W. Geertsma and D. Khomskii, Phys. Rev. B **54**, 3011 (1996)

[6] V. Yushankhai, M. Wolf, K.-H. Müller, R. Hayn, and H. Rosner, Phys. Rev. B **62**, 14229 (2000)

[7] R. Hayn, V. A. Pashchenko, A. Stepanov, T. Masuda, and K. Uchinokura, Phys. Rev. B **66**, 184414 (2002)

[8] M. V. Mostovoy and D. I. Khomskii, Phys. Rev. Lett. **89**, 227203 (2002)

[9] E. Müller-Hartmann and A. Reischl, Eur. Phys. J. B **28**, 173 (2002)

[10] R. M. Eremina, M. V. Eremin, V. N. Glazkov, H.-A. K. von Nidda, and A. Loidl, Phys. Rev. B **68**, 014417 (2003)

[11] M. V. Mostovoy and D. I. Khomskii, Phys. Rev. Lett. **92**, 167201 (2004)

[12] P. M. Krstajić, F. M. Peeters, V. A. Ivanov, V. Fleurov, and K. Kikoin, Phys. Rev. B **70**, 195215 (2004)

[13] A. M. Oleś, L. F. Feiner, P. Horsch, and G. Khaliullin, Phys. Status Solidi B **243**, 89 (2006)

[14] R. Raghunathan, J.-P. Sutter, L. Ducasse, C. Desplanches, and S. Ramasesha, Phys. Rev. B **73**, 104438 (2006)

[15] F. Tuczek and E. I. Solomon, Inorg. Chem. **32**, 2850 (1993)

[16] C. A. Brown, G. J. Remar, R. L. Musselman, and E. I. Solomon, Inorg. Chem. **34**, 688 (1995)

[17] H. Weihe, H. U. Güdel, and H. Toftlund, Inorg. Chem. **39**, 1351 (2000)

[18] F. Tuczek and E. I. Solomon, Coord. Chem. Rev. **219-221**, 1075 (2001)

[19] C. J. Calzado, J. Cabrero, J.-P. Malrieu, and R. Caballol, J. Chem. Phys. **116**, 2728 (2002)

[20] C. J. Calzado, J. Cabrero, J.-P. Malrieu, and R. Caballol, J. Chem. Phys. **116**, 3985 (2002)

[21] P. W. Anderson, in *Magnetism*, Vol. 1, edited by G. T. Rado and H. Suhl (Academic Press, New York, 1963) p. 25

[22] P. W. Anderson, in *Solid State Physics*, Vol. 14 (Academic Press, London, 1963) p. 99

[23] W. Geertsma, Physica B **164**, 241 (1990)

[24] J. Zaanen and G. A. Sawatzky, Can. J. Phys. **65**, 1262 (1987)

[25] K.-I. Gondaira and Y. Tanabe, J. Phys. Soc. Jpn. **21**, 1527 (1966)

[26] J. Zaanen, G. A. Sawatzky, and J. W. Allen, Phys. Rev. Lett. **55**, 418 (1985)

[27] W. Geertsma, *Theory of d electrons in transition metal insulators*, Ph.D. thesis, University of Groningen, Groningen (1980)

[28] L. F. Chibotaru, J.-J. Girerd, G. Blondin, T. Glaser, and K. Wieghardt, J. Am. Chem. Soc. **125**, 12615 (2003)

[29] Z.-X. Shen, J. W. Allen, J. J. Yeh, J.-S. Kang, W. Ellis, W. Spicer, I. Lindau, M. B. Maple, Y. D. Dalichaouch, M. S. Torikachvili, J. Z. Sun, and T. H. Geballe, Phys. Rev. B **36**, 8414 (1987)

[30] P. J. Hay, J. C. Thibeault, and R. Hoffmann, J. Am. Chem. Soc. **97**, 4884 (1975)

[31] J. Zaanen and G. A. Sawatzky, J. Solid State Chem. **88**, 8 (1990)

Addendum A

Supplements to chapter 2

A.1 Fourth-order exchange Hamiltonian

In the paper the expressions of the exchange Hamiltonian in the Anderson basis were given explicitly up to third order of perturbation (Eqs. (2.3.13), (2.3.14) and (2.C.1)). The fourth-order term, which was used in the paper but not given there explicitly, is written out here. We recall from Eq. (2.3.12) that

$$\begin{aligned} H^{(4)}_{\mathrm{And}} = {} & P_0 H' \frac{P}{a} H' \frac{P}{a} H' \frac{P}{a} H' P_0 - P_0 H' \frac{P}{a} H' \frac{P}{a^2} H' P_0 H' P_0 \\ & - P_0 H' \frac{P}{a^2} H' \frac{P}{a} H' P_0 H' P_0 - P_0 H' \frac{P}{a} H' P_0 H' \frac{P}{a^2} H' P_0 \\ & + P_0 H' \frac{P}{a^3} H' P_0 H' P_0 H' P_0, \end{aligned} \tag{A.1.1}$$

with H', P, and P_0 as specified in section 2.C. The different terms in Eq. (A.1.1) are given on the next pages. We remark here that

$$P_0 H' \frac{P}{a} H' \frac{P}{a^2} H' P_0 H' P_0 = P_0 H' \frac{P}{a^2} H' \frac{P}{a} H' P_0 H' P_0$$

because

$$P_0 H' \frac{P}{a} H' \frac{P}{a^2} H' P_0 = (P_0 H' \frac{P}{a^2} H' \frac{P}{a} H' P_0)^\dagger = P_0 H' \frac{P}{a^2} H' \frac{P}{a} H' P_0. \tag{A.1.2}$$

The second equality in Eq. (A.1.2) follows from the hermiticity of the $\hat{\mathbf{S}}_\mathbf{1}\hat{\mathbf{S}}_\mathbf{2}$ operator, as discussed in section 2.C.

$$
\begin{aligned}
P_0H'\frac{P}{a}H'\frac{P}{a}H'\frac{P}{a}H'P_0 = 4\hat{\mathbf{S}}_\mathbf{1}\hat{\mathbf{S}}_\mathbf{2}\Bigg(&\frac{\tilde{V}_{1122}^2(\tilde{t}_{12}+\tilde{V}_{1222})^2}{(\tilde{U}-\tilde{K}_{12})^3}\\
&+\frac{2\Big\{\tilde{V}_{122l}(\tilde{t}_{1l}+\tilde{V}_{12l2})\Big[(\tilde{t}_{12}+\tilde{V}_{1l2l}+\tilde{J}_{1l})^2+\tilde{V}_{1ll2}^2\Big]+(\tilde{t}_{12}+\tilde{V}_{1l2l}+\tilde{J}_{1l})\tilde{V}_{1ll2}\Big[\tilde{V}_{122l}^2+(\tilde{t}_{1l}+\tilde{V}_{12l2})^2\Big]\Big\}}{(\tilde{\Delta}-\tilde{K}_{12}+\tilde{K}_{1l})^3}\\
&+\frac{2(\tilde{t}_{12}+\tilde{V}_{1222})(\tilde{t}_{1l}+\tilde{V}_{122l}+\tilde{V}_{l111})\Big[(\tilde{t}_{12}+\tilde{V}_{1222})(\tilde{t}_{1l}+\tilde{V}_{122l}+\tilde{V}_{l111})+\tilde{V}_{1122}(\tilde{t}_{1l}+\tilde{V}_{122l}+\tilde{V}_{12l2})\Big]}{(\tilde{U}-\tilde{K}_{12})^2(\tilde{\Delta}-\tilde{K}_{12}+\tilde{K}_{1l})}\\
&+\frac{(\tilde{t}_{1l}+\tilde{V}_{122l}+\tilde{V}_{12l2})(\tilde{t}_{1l}+\tilde{V}_{122l}+\tilde{V}_{l111})\Big[2(\tilde{t}_{12}+\tilde{V}_{1222})(\tilde{t}_{12}+\tilde{V}_{1l2l}+\tilde{J}_{1l}+\tilde{V}_{1ll2})+(\tilde{t}_{1l}+\tilde{V}_{122l}+\tilde{V}_{12l2})(\tilde{t}_{1l}+\tilde{V}_{122l}+\tilde{V}_{l111})\Big]}{(\tilde{U}-\tilde{K}_{12})(\tilde{\Delta}-\tilde{K}_{12}+\tilde{K}_{1l})^2}\\
&+\frac{2(\tilde{t}_{1l}+\tilde{V}_{122l}+\tilde{V}_{12l2})(\tilde{t}_{1l}+\tilde{V}_{1ll})\Big[\tilde{V}_{1ll2}(\tilde{t}_{12}+\tilde{V}_{1l2l}+\tilde{J}_{1l}+\tilde{V}_{1ll2})+(\tilde{t}_{1l}+\tilde{V}_{122l}+\tilde{V}_{12l2})(\tilde{t}_{1l}+\tilde{V}_{1ll})\Big]}{(\tilde{\Delta}-\tilde{K}_{12}+\tilde{K}_{1l})^2(2\tilde{\Delta}-\tilde{K}_{12}+\tilde{U}')}\\
&+\frac{\tilde{V}_{11ll}^2\tilde{V}_{1ll2}^2}{(\tilde{U}-\tilde{K}_{12})(2\tilde{\Delta}-\tilde{K}_{12}+\tilde{U}')^2}+\frac{2\tilde{V}_{1ll2}^2(\tilde{t}_{1l}+\tilde{V}_{1ll})^2}{(\tilde{\Delta}-\tilde{K}_{12}+\tilde{K}_{1l})(2\tilde{\Delta}-\tilde{K}_{12}+\tilde{U}')^2}+\frac{2\tilde{V}_{11ll}(\tilde{t}_{12}+\tilde{V}_{1222})\Big[\tilde{V}_{11ll}(\tilde{t}_{12}+\tilde{V}_{1222})+\tilde{V}_{1122}\tilde{V}_{1ll2}\Big]}{(\tilde{U}-\tilde{K}_{12})^2(2\tilde{\Delta}-\tilde{K}_{12}+\tilde{U}')}\\
&+2\Big\{2\tilde{t}_{12}(\tilde{t}_{1l}+\tilde{V}_{1ll})\Big[\tilde{V}_{11ll}(\tilde{V}_{122l}+\tilde{V}_{12l2})+\tilde{t}_{1l}(\tilde{V}_{11ll}+\tilde{V}_{1ll2})+\tilde{V}_{1ll2}(\tilde{V}_{122l}+\tilde{V}_{l111})\Big]+\tilde{V}_{11ll}\tilde{V}_{122l}(\tilde{V}_{122l}\tilde{V}_{1ll2}+\tilde{V}_{12l2}\tilde{V}_{1ll2})\\
&+\tilde{V}_{1ll2}\Big[\tilde{V}_{11ll}(\tilde{V}_{122l}+\tilde{V}_{12l2})+2\tilde{V}_{1222}\tilde{V}_{1ll}\Big]\tilde{V}_{l111}+2\tilde{V}_{1ll}\tilde{V}_{1222}(\tilde{V}_{122l}\tilde{V}_{11ll}+\tilde{V}_{12l2}\tilde{V}_{11ll}+\tilde{V}_{122l}\tilde{V}_{1ll2})\\
&+\tilde{t}_{1l}^2\Big[2\tilde{V}_{1222}\tilde{V}_{1ll2}+\tilde{V}_{11ll}(2\tilde{V}_{1222}+\tilde{V}_{1ll2})\Big]+\tilde{t}_{1l}\Big[2\tilde{V}_{1222}\tilde{V}_{1ll2}(\tilde{V}_{122l}+\tilde{V}_{1ll}+\tilde{V}_{l111})\\
&+\tilde{V}_{11ll}\Big(2\tilde{V}_{1222}(\tilde{V}_{122l}+\tilde{V}_{12l2}+\tilde{V}_{1ll})+\tilde{V}_{1ll2}(2\tilde{V}_{122l}+\tilde{V}_{12l2}+\tilde{V}_{l111})\Big)\Big]\Big\}\Big/(\tilde{U}-\tilde{K}_{12})(\tilde{\Delta}-\tilde{K}_{12}+\tilde{K}_{1l})(2\tilde{\Delta}-\tilde{K}_{12}+\tilde{U}')\Bigg)
\end{aligned}
$$

$$P_0H'\frac{P}{a}H'\frac{P}{a^2}H'P_0H'P_0 = 4\hat{\mathbf{S}}_\mathbf{1}\hat{\mathbf{S}}_\mathbf{2}\tilde{J}_{12}\Bigg(\frac{\tilde{V}_{1122}(\tilde{t}_{12}+\tilde{V}_{1222})^2}{(\tilde{U}-\tilde{K}_{12})^3}+\frac{(\tilde{t}_{12}+\tilde{V}_{1222})(\tilde{t}_{1l}+\tilde{V}_{122l}+\tilde{V}_{12l2})(\tilde{t}_{1l}+\tilde{V}_{122l}+\tilde{V}_{l111})}{(\tilde{U}-\tilde{K}_{12})(\tilde{\Delta}-\tilde{K}_{12}+\tilde{K}_{1l})^2}$$
$$+\frac{2\tilde{V}_{122l}(\tilde{t}_{1l}+\tilde{V}_{12l2})(\tilde{t}_{12}+\tilde{V}_{1l2l}+\tilde{J}_{1l})+\left[\tilde{V}_{122l}^2+(\tilde{t}_{1l}+\tilde{V}_{12l2})^2\right]\tilde{V}_{1ll2}}{(\tilde{\Delta}-\tilde{K}_{12}+\tilde{K}_{1l})^3}+\frac{(\tilde{t}_{1l}+\tilde{V}_{122l}+\tilde{V}_{12l2})\tilde{V}_{1ll2}(\tilde{t}_{1l}+\tilde{V}_{1lll})}{(\tilde{\Delta}-\tilde{K}_{12}+\tilde{K}_{1l})(2\tilde{\Delta}-\tilde{K}_{12}+\tilde{U}')^2}$$
$$+\frac{(\tilde{t}_{12}+\tilde{V}_{1222})(\tilde{t}_{1l}+\tilde{V}_{122l}+\tilde{V}_{12l2})(\tilde{t}_{1l}+\tilde{V}_{122l}+\tilde{V}_{l111})}{(\tilde{U}-\tilde{K}_{12})^2(\tilde{\Delta}-\tilde{K}_{12}+\tilde{K}_{1l})}+\frac{\tilde{V}_{11ll}(\tilde{t}_{12}+\tilde{V}_{1222})\tilde{V}_{1ll2}}{(\tilde{U}-\tilde{K}_{12})(2\tilde{\Delta}-\tilde{K}_{12}+\tilde{U}')^2}$$
$$+\frac{\tilde{V}_{11ll}(\tilde{t}_{12}+\tilde{V}_{1222})\tilde{V}_{1ll2}}{(\tilde{U}-\tilde{K}_{12})^2(2\tilde{\Delta}-\tilde{K}_{12}+\tilde{U}')}+\frac{(\tilde{t}_{1l}+\tilde{V}_{122l}+\tilde{V}_{12l2})\tilde{V}_{1ll2}(\tilde{t}_{1l}+\tilde{V}_{1lll})}{(\tilde{\Delta}-\tilde{K}_{12}+\tilde{K}_{1l})^2(2\tilde{\Delta}-\tilde{K}_{12}+\tilde{U}')}\Bigg)$$

$$P_0H'\frac{P}{a}H'P_0H'\frac{P}{a^2}H'P_0 = 4\hat{\mathbf{S}}_\mathbf{1}\hat{\mathbf{S}}_\mathbf{2}\Bigg(\frac{4(\tilde{t}_{12}+\tilde{V}_{1222})^4}{(\tilde{U}-\tilde{K}_{12})^3}+\frac{8\tilde{V}_{122l}(\tilde{t}_{1l}+\tilde{V}_{12l2})\left[\tilde{V}_{122l}^2+(\tilde{t}_{1l}+\tilde{V}_{12l2})^2\right]}{(\tilde{\Delta}-\tilde{K}_{12}+\tilde{K}_{1l})^3}+\frac{\tilde{V}_{1ll2}^4}{(2\tilde{\Delta}-\tilde{K}_{12}+\tilde{U}')^3}$$
$$+\frac{2(\tilde{t}_{12}+\tilde{V}_{1222})^2(\tilde{t}_{1l}+\tilde{V}_{122l}+\tilde{V}_{12l2})^2}{(\tilde{U}-\tilde{K}_{12})(\tilde{\Delta}-\tilde{K}_{12}+\tilde{K}_{1l})^2}+\frac{2(\tilde{t}_{12}+\tilde{V}_{1222})^2(\tilde{t}_{1l}+\tilde{V}_{122l}+\tilde{V}_{12l2})^2}{(\tilde{U}-\tilde{K}_{12})^2(\tilde{\Delta}-\tilde{K}_{12}+\tilde{K}_{1l})}+\frac{2(\tilde{t}_{12}+\tilde{V}_{1222})^2\tilde{V}_{1ll2}^2}{(\tilde{U}-\tilde{K}_{12})(2\tilde{\Delta}-\tilde{K}_{12}+\tilde{U}')^2}$$
$$+\frac{(\tilde{t}_{1l}+\tilde{V}_{122l}+\tilde{V}_{12l2})^2\tilde{V}_{1ll2}^2}{(\tilde{\Delta}-\tilde{K}_{12}+\tilde{K}_{1l})(2\tilde{\Delta}-\tilde{K}_{12}+\tilde{U}')^2}+\frac{2(\tilde{t}_{12}+\tilde{V}_{1222})^2\tilde{V}_{1ll2}^2}{(\tilde{U}-\tilde{K}_{12})^2(2\tilde{\Delta}-\tilde{K}_{12}+\tilde{U}')}+\frac{(\tilde{t}_{1l}+\tilde{V}_{122l}+\tilde{V}_{12l2})^2\tilde{V}_{1ll2}^2}{(\tilde{\Delta}-\tilde{K}_{12}+\tilde{K}_{1l})^2(2\tilde{\Delta}-\tilde{K}_{12}+\tilde{U}')}\Bigg)$$

$$P_0H'\frac{P}{a^3}H'P_0H'P_0H'P_0 = 2\hat{\mathbf{S}}_\mathbf{1}\hat{\mathbf{S}}_\mathbf{2}\tilde{J}_{12}^2\Bigg(\frac{2(\tilde{t}_{12}+\tilde{V}_{1222})^2}{(\tilde{U}-\tilde{K}_{12})^3}+\frac{4\tilde{V}_{122l}(\tilde{t}_{1l}+\tilde{V}_{12l2})}{(\tilde{\Delta}-\tilde{K}_{12}+\tilde{K}_{1l})^3}+\frac{\tilde{V}_{1ll2}^2}{(2\tilde{\Delta}-\tilde{K}_{12}+\tilde{U}')^3}\Bigg)$$

A.2 The status of the three-orbital exchange model

The three-orbital M-L-M exchange model was introduced at the beginning of the quantum mechanics era (perhaps first by H. A. Kramers) to investigate the microscopic origin of exchange interaction in different systems. Since then it has remained the basic theoretical tool for the rationalization of mechanisms of exchange interactions because it includes the basic electronic interactions which govern the exchange coupling in both molecules and solids. In particular, it describes naturally the superexchange interaction and its two basic contributions, the kinetic and potential exchange [1].

It is well known [2] that besides the antiferromagnetic kinetic and the ferromagnetic potential exchange contributions there are also the ferromagnetic kinetic exchange contribution (the Goodenough mechanism) and the spin polarization exchange contribution (the RKKY mechanism). The situations when the latter play an important role are well known. Thus the Goodenough mechanism is important when the electron transfer from magnetic orbitals on one M center to some empty orbitals on another M center is stronger than the electron transfer between the magnetic orbitals of the two centers. The spin polarization becomes important when the two magnetic centers are separated by a relatively large diamagnetic bridge, in which case the kinetic and potential exchange contributions are relatively less important because their strength decays quickly with the distance between the centers. Both these additional mechanisms cannot be treated within the basic M-L-M model because only a single orbital is included on each M and L. On the other hand, in strongly coupled metal pairs, like Cu(II)-O(II)-Cu(II) fragments of high-Tc superconductors, the Goodenough and spin polarization contribution are not important and the basic exchange model is sufficient to describe the exchange coupling.

The strongest electronic interaction which is not included explicitly in the M-L-M model is the electric polarization induced during the virtual electron transfer between the M centers. This interaction (V') can reduce the intracenter interelectron repulsion (U_0) by ca. 10 eV [1]. However, as stated by Anderson, these effects can be included into the M-L-M model by using the renormalized bielectronic parameter: $U = U_0 - V'$, which is assumed in the present work. Other parameters entering the M-L-M model are also renormalized in a similar way.

Finally, we would like to repeat that the aim of this chapter is only to analyze the validity of the Anderson orbital approximation and of the VBCI approximation for the treatment of exchange interaction. The conclusions on their applicability which we reach here go beyond the M-L-M model and can be extended also to all-electron treatments. For instance, in the work by P. de Loth, P. Cassoux, J. P. Daudey and J. P. Malrieu [3], who performed an all-electron perturbational

treatment of exchange interactions within Anderson's orbital approximation, it was noted that the convergence of the perturbation series was not perfect (see also [4], p.159). In view of the results obtained in the present chapter it seems quite probable that the reason for that resides in the Anderson approximation.

Bibliography

[1] P. W. Anderson, Phys. Rev. **115**, 2 (1959)

[2] P. W. Anderson, in *Magnetism*, Vol. 1, edited by G. T. Rado and H. Suhl (Academic Press, New York, 1963) p. 25

[3] P. de Loth, P. Cassoux, J. P. Daudey, and J. P. Malrieu, J. Am. Chem. Soc. **103**, 4007 (1981)

[4] O. Kahn, *Molecular Magnetism* (VCH Publishers, New York, 1993)

Chapter 3

Elucidation of the magnetism of $[Co_2PdCl_2(dpa)_4]$: origin of a large temperature-domain of TIP-behavior

Abstract The recently synthesized heterotrimetallic complex $[Co_2PdCl_2(dpa)_4]$ shows an unusual temperature-independent paramagnetism, extending over the whole experimental temperature range (0–300 K) [1]. We explain this behavior from a microscopic approach, using ligand field theory and Anderson's kinetic exchange theory, treating the non-magnetic Pd^{II} as a ligand. The orbital degeneracy of the Co^{II} ions is taken into account in the construction of the model Hamiltonian. The extension of the TIP behavior, compared to mononuclear Co^{II} compounds, over the whole temperature domain, is explained by the quenching of magnetic moments in thermally populated levels by strong antiferromagnetic exchange interaction.

3.1 Introduction

Anisotropic magnetic properties of transition metal complexes attract increasing interest last years, first of all in connection with the design of efficient single-molecule magnets [2]. Among molecular compounds exhibiting strong magnetic anisotropy, those containing Co^{II} ions present us with problems defying understanding in terms of simple spin Hamiltonians, which have been very successfull in the field of molecular magnetism. Today, the possibilities of Co^{II} ions in the search for materials with desired magnetic properties are explored intensively. Theoretical investigations into the nature of the magnetic behavior

W. Van den Heuvel and L. F. Chibotaru, Inorg. Chem. **48**, 7557 (2009)

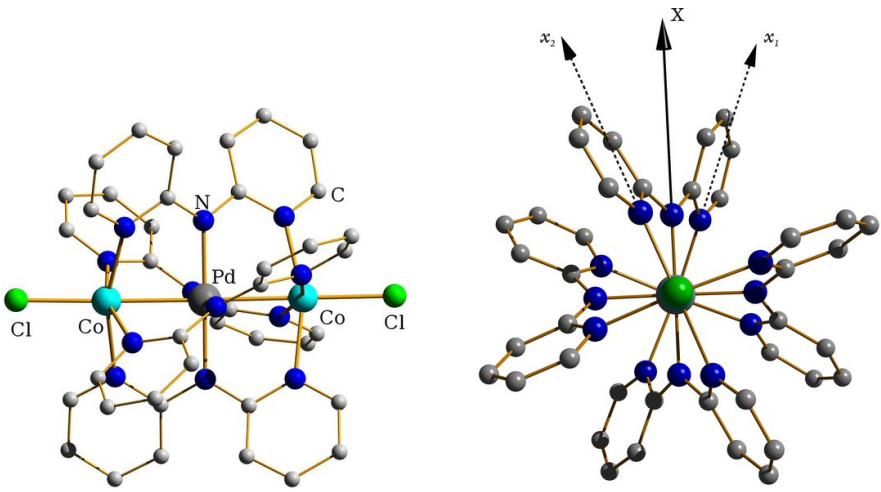

Figure 3.1: Side and axial view of $[Co_2PdCl_2(dpa)_4]$. The dashed lines show the local x-axes on the Co sites, while the solid line shows the X-axis of the molecular coordinate system.

of such compounds are therefore very desirable, in particular for pointing out the limitations of the simple spin Hamiltonians.

This paper deals with the theoretical analysis of the magnetism of the recently synthesized heterotrimetallic complex $[Co_2PdCl_2(dpa)_4]$ [1]. In this complex, the two magnetic Co^{II} ions are separated by and collinear with the nonmagnetic Pd^{II} ion. They are held together by 4 dpa ligands and two Cl^- ions, forming a complex with D_4 symmetry (Fig. 3.1). The coupling between the Co^{II} ions was shown to be antiferromagnetic and stronger than in any preceding Co^{II} dinuclear complex [1]. The magnetic susceptibility of this complex is almost temperature-independent from 0 K to 300 K, as follows from the linear behavior of χT (Fig. 3.5) [1]. The explanation of this behavior will be the subject of the present paper.

To analyze experimental data theoretically, exhange interactions between transition metal ions with local anisotropies are usually modelled with a spin Hamiltonian, working in the local spin states. For example, when the local symmetry is tetragonal around the local z axis, one uses

$$\hat{H} = \sum_{i,j} J_{ij} \hat{\mathbf{S}}_i \cdot \hat{\mathbf{S}}_j + \sum_i D_i \hat{S}_{iz}^2. \tag{3.1.1}$$

Inherent in this Hamiltonian are the assumptions that the local ground states are not orbitally degenerate and that spin-orbit coupling can be accounted for

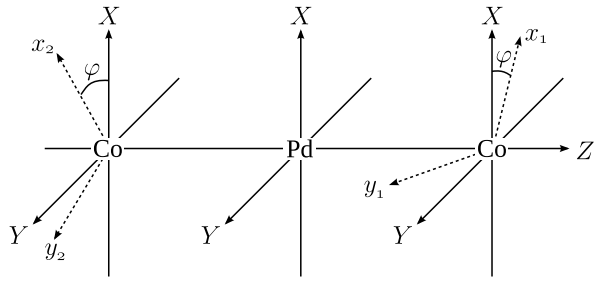

Figure 3.2: Local coordinate systems x_1y_1Z and x_2y_2Z on the Co(1) and Co(2) sites, respectively, and the molecular coordinate system XYZ.

by second-order perturbation theory. In a (distorted) octahedral ligand field, high-spin Co^{II} ($S = 3/2$) does not belong to this class of systems because of its threefold orbital (quasi)degeneracy, leading to unquenched orbital momentum in the ground state, together with a relatively strong spin-orbit coupling constant ($\zeta \approx 500\,\mathrm{cm}^{-1}$). This makes the actual situation far from the pure spin limit and a more detailed Hamiltonian is called for.

The theoretical framework for the study of exchange-coupled transition metal ions is already established: it consists of a combination of ligand field theory and Anderson's kinetic exchange theory [3]. In the case of orbitally degenerate ions the exchange interaction is described by a spin-orbital Hamiltonian which is, in general, anisotropic [4, 5]. In the context of molecular magnetism spin-orbital exchange models have already been applied for several high-symmetry binuclear complexes [6–9]. Theoretical model studies of the exchange coupling between high-spin Co^{II} ions based on these theories have been reported [10, 11]. In this paper, we apply this theory to explain the magnetism of the $[Co_2PdCl_2(dpa)_4]$ complex. On the basis of considerations of geometry and electronic configuration, a model Hamiltonian is derived and subsequently used to calculate magnetic properties of the complex. With essentially only two parameters, a satisfactory fit of the magnetic susceptibility can be obtained, although it is recognized that the available experimental information does not suffice to assess the correctness of the model completely.

We start with the construction of the model Hamiltonian in the next section, followed by a discussion of its spectrum in some limiting cases in Section 3.3. The application to the title complex is presented in Section 3.4.

3.2 The model Hamiltonian

Let us consider the structure of the CoPdCo complex first. The three metal ions are hold together in a linear chain by 4 dipyridylamido (dpa) ligands that are helically wound around the chain. Two Cl^- ions are coordinated axially to the cobalt ions. The local symmetry group on the cobalt sites is C_4, with the Z axis as shown in Fig. 3.2. Due to the helical nature of the coordinating dpa groups, the local axes on the Co sites are rotated through Z with respect to each other, as shown in Figs. 3.1 and 3.2. They make an angle of φ with the molecular coordinate system XYZ. Bond distances and magnetic measurements indicate that both Co^{II} ($3d^7$) ions are in the high-spin state (S=3/2) while Pd^{II} ($4d^8$) is in the closed-shell low-spin state (S=0) [1].

The octahedral $^4T_1$ ground states of the two Co^{II} ions will serve as basis functions for the effective Hamiltonian. They are a linear combination of two configurational strong-field states:

$$|^4T_1\rangle = c_1|t_2^5\, e^2\ {}^4T_1\rangle + c_2|t_2^4\, e^3\ {}^4T_1\rangle.$$

The contribution of the $t_2^4\, e^3$ configuration is at most 20 % (low-field limit) and goes to 0 % in the strong-field limit. Note that the three spatial components of $|^4T_1\rangle$ are defined with respect to the local coordinate system on the Co site (See Fig. 3.2). Let $|^4{T_1}^{(i)}\rangle$ denote the $^4T_1$ state on Co(i), then we have:

$$\begin{aligned} \mathrm{Co}(1): &\quad \left\{|^4{T_1}^{(1)}x_1\rangle,\ |^4{T_1}^{(1)}y_1\rangle,\ |^4{T_1}^{(1)}Z\rangle\right\} \\ \mathrm{Co}(2): &\quad \left\{|^4{T_1}^{(2)}x_2\rangle,\ |^4{T_1}^{(2)}y_2\rangle,\ |^4{T_1}^{(2)}Z\rangle\right\}. \end{aligned}$$

The on-site tetragonal ligand field and spin-orbit coupling are considered in the first order of perturbation theory. According to the T-P correspondence a $^4T_1$ term can be replaced by a spherical ^4P term. For one center the resulting Hamiltonian is [12]

$$\hat{H}_1 = \Delta(\hat{L}_{1z}^2 - 2/3) - \frac{1}{3}\zeta\gamma\hat{\mathbf{L}}_1 \cdot \hat{\mathbf{S}}_1, \tag{3.2.1}$$

where ζ is the spin-orbit coupling constant, γ accounts for the correspondence between the T_1 and P states, and Δ is the tetragonal splitting (Fig. 3.3). The factor γ depends both on the orbital reduction factor κ and on the composition of the $^4T_1$ states in terms of $t_2^5\, e^2$ and $t_2^4\, e^3$ configurations. It obeys: $-3/2\kappa < \gamma < -\kappa$ [12, 13].

We suppose now that the Pd ion can be treated as a ligand in the theory of superexchange interactions, as was the case for diamagnetic metal ions in other trinuclear complexes [14]. This means that states on the Pd ion will not

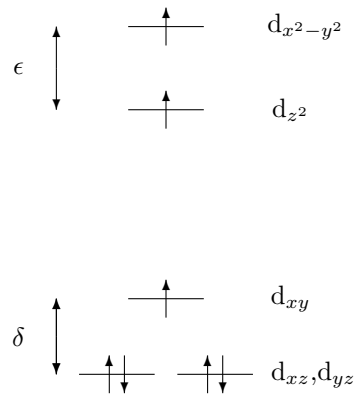

Figure 3.3: Schematic representation of the $|^4\mathrm{T}_1 z, M_S = 3/2\rangle$ component of the $\mathrm{t}_2^5\,\mathrm{e}^2$ configuration on $\mathrm{Co^{II}}$. The tetragonal splitting parameter in $\hat{H}_1$ is given by $\Delta = \delta c_1^2 - (\delta + 3/4\epsilon)c_2^2$.

be considered in the model treatment; the role of the 4d orbitals of Pd is to provide hybridization to the 3d orbitals of Co (and, therefore, pathways for kinetic exchange), a role that is normally played only by nonmetallic ligands. The origin of the strong antiferromagnetic exchange interaction in the present complex can than be understood as follows: in the ground-state configuration of $\mathrm{Co^{II}}$, the $3\mathrm{d}_{z^2}$ orbital is singly occupied and has an interaction with the $4\mathrm{d}_{z^2}$ orbital on Pd, resulting in a pathway for antiferromagnetic exchange interaction between the spins on the two Co sites [3]. The fact that this antiferromagnetic interaction is much stronger than in conventional dinuclear Co complexes is due to the large spatial extension of 4d orbitals (better σ-overlap between d_{z^2} orbitals) and the possibility of near-resonance between the d_{z^2} orbitals on Co and Pd. This interpretation is consistent with the exchange interaction in the isostructural complex $[\mathrm{Cu_2Pd(dpa)_4Cl_2}]$, which was found to be much smaller than in the cobalt compound [15]. The d_{z^2} orbital on $\mathrm{Cu^{II}}$ is indeed doubly occupied, so that the mechanism described above is not available there.

Expressions for the exchange Hamiltonian between corner-shared bioctahedral $\mathrm{Co^{II}}$ dimers have been derived within the Anderson kinetic exchange theory by Palii et al. [10]. In terms of the kinetic transfer parameter t_σ [3] and an averaged charge transfer energy U, the Hamiltonian for exchange between the $3\mathrm{d}_{z^2}$ orbitals is

$$\hat{H}_{\mathrm{exch},\sigma} = \frac{4}{9}\frac{t_\sigma^2}{U}\left(1 - \frac{3}{4}c_2^2\hat{L}_{1z}^2\right)\left(1 - \frac{3}{4}c_2^2\hat{L}_{2z}^2\right)\hat{\mathbf{S}}_1 \cdot \hat{\mathbf{S}}_2 + \frac{9}{16}c_2^4\hat{L}_{1z}^2\hat{L}_{2z}^2$$

The orbital-dependent anisotropic terms come into $\hat{H}_{\mathrm{exch},\sigma}$ by the fact that,

for $|^4\mathrm{T}_1 x\rangle$ and $|^4\mathrm{T}_1 y\rangle$, the $3\mathrm{d}_{z^2}$ orbital is in part doubly occupied in the $\mathrm{t}_2^4\,\mathrm{e}^3$ configuration, therefore reducing the exchange interaction in comparison with $|^4\mathrm{T}_1 z\rangle$. An estimation of c_2^2 can be obtained from the complex $[\mathrm{Co}(\mathrm{NH}_3)_6]^{2+}$, for which $c_2^2 \approx 0.08$ [12]. The anisotropic part of $\hat{H}_{\mathrm{exch},\sigma}$, which is $O(c_2^2)$, can thus be considered as a small perturbation on the isotropic Heisenberg Hamiltonian $J_\sigma \hat{\mathbf{S}}_1 \cdot \hat{\mathbf{S}}_2$. Anticipating the results in Section 3.4, where we will find that the ground state is well separated from excited states, we can ignore this perturbation without introducing appreciable error in the magnetic susceptibility: at low temperature, only the ground state is occupied, on which the perturbation has little effect, while at higher temperatures the perturbation becomes irrelevant to the susceptibility [12].

The transfer of π-type (d_{xz} and d_{yz}) and δ-type (d_{xy} and $\mathrm{d}_{x^2-y^2}$) electrons can also be mediated by the Pd ion. The corresponding kinetic transfer parameters t_π and t_δ are progressively smaller than t_σ because, in perturbation theory, they are proportional to the square of the overlap between the Co and Pd orbitals, which is respectively of the π-π and δ-δ type. The smallness of these direct overlaps in comparison with the σ-σ-overlap leads us to regard the π- and δ-type exchange interactions as small perturbations, which, by the argument of the previous paragraph, can be ignored for the present purpose.

Likewise, several smaller interactions, such as ligand fields of lower symmetry, and the Coulomb repulsion between sites, which leads to an energy differentiation akin to exciton dispersion, can be omitted from the Hamiltonian.

In writing down the total Hamiltonian of the dimer in a magnetic field $\mathbf{B}$, attention must be paid to the fact that the local coordinate axes are not parallel. The cylindrical symmetry of the local and exchange Hamiltonians ensures however that, by applying the T-P correspondence

$$
\begin{aligned}
{}^4\mathrm{P}^{(1)}{}_X &\sim \cos\varphi\, |{}^4\mathrm{T}_1{}^{(1)} x_1\rangle + \sin\varphi\, |{}^4\mathrm{T}_1{}^{(1)} y_1\rangle \\
{}^4\mathrm{P}^{(1)}{}_Y &\sim -\sin\varphi\, |{}^4\mathrm{T}_1{}^{(1)} x_1\rangle + \cos\varphi\, |{}^4\mathrm{T}_1{}^{(1)} y_1\rangle \\
{}^4\mathrm{P}^{(1)}{}_Z &\sim |{}^4\mathrm{T}_1{}^{(1)} Z\rangle,
\end{aligned}
$$

on Co(1) and

$$
\begin{aligned}
{}^4\mathrm{P}^{(2)}{}_X &\sim \cos\varphi\, |{}^4\mathrm{T}_1{}^{(2)} x_2\rangle - \sin\varphi\, |{}^4\mathrm{T}_1{}^{(2)} y_2\rangle \\
{}^4\mathrm{P}^{(2)}{}_Y &\sim \sin\varphi\, |{}^4\mathrm{T}_1{}^{(2)} x_2\rangle + \cos\varphi\, |{}^4\mathrm{T}_1{}^{(2)} y_2\rangle \\
{}^4\mathrm{P}^{(2)}{}_Z &\sim |{}^4\mathrm{T}_1{}^{(2)} Z\rangle,
\end{aligned}
$$

on Co(2), the total effective Hamiltonian, written in the molecular coordinate system XYZ (Fig. 3.2), is independent of the angle φ:

$$\hat{H} = \Delta\left(\hat{L}_{1z}^2 + \hat{L}_{2z}^2 - 4/3\right) - \frac{1}{3}\zeta\gamma\left(\hat{\mathbf{L}}_1\cdot\hat{\mathbf{S}}_1 + \hat{\mathbf{L}}_2\cdot\hat{\mathbf{S}}_2\right) + J_\sigma\hat{\mathbf{S}}_1\cdot\hat{\mathbf{S}}_2 + \mu_B\left[2\left(\hat{\mathbf{S}}_1+\hat{\mathbf{S}}_2\right)+\gamma\left(\hat{\mathbf{L}}_1+\hat{\mathbf{L}}_2\right)\right]\cdot\mathbf{B}, \quad (3.2.2)$$

working in the space of $|LSM_LM_S\rangle_1\cdot|LSM_LM_S\rangle_2$ states ($L=1$ and $S=3/2$), which are defined in the same XYZ coordinate system. We remark here that the obtained exchange Hamiltonian ($J_\sigma\hat{\mathbf{S}}_1\cdot\hat{\mathbf{S}}_2$) is the isotropic Heisenberg interaction between real spins, which was tentatively introduced by Lines in a model for the thermodynamic properties of cobalt clusters [16]. The above derivation confirms the correctness of Lines' model for the present compound, but underlines at the same time the fact that this correctness is not trivial and cannot be expected to hold in every case.

Before applying Hamiltonian (3.2.2) to the problem at hand, we will consider some properties of its spectrum.

3.3 Exchange spectrum in some limiting cases

To gain a better insight into the meaning of the Hamiltonian in Eq. (3.2.2), it is useful to consider some special cases that are covered by this Hamiltonian in a zero magnetic field. The most convenient approach is to start from the spectrum of the single Co^{II} ions, described by the Hamiltonian in Eq. (3.2.1). Because this Hamiltonian has cylindrical symmetry around the z-axis, the eigenstates are labeled by a rotational quantum number M_J, the pairs $\pm M_J$ being degenerate (Kramers degeneracy). A plot of the energy levels as a function of Δ is presented in Fig. 3.4. Three limiting regimes are apparent: $\frac{\Delta}{|\gamma\zeta|} >> 1, = 0$ and $<< -1$. In each of these, the lowest states of the dimer can be described by an Hamiltonian of lower dimension if the exchange interaction is much smaller than the intrasite interactions.

Consider first the case where Δ is positive and large and the ground state is a spin-only state (^{4}A in the point group C_4), corresponding to the electron configuration drawn in Fig. 3.3. In this space, the effective Hamiltonian has the form of the well known spin Hamiltonian in Eq. (3.1.1):

$$\hat{H} = J\hat{\mathbf{S}}_1\cdot\hat{\mathbf{S}}_2 + D\left(\hat{S}_{1z}^2 + \hat{S}_{2z}^2\right),$$

with $J = J_\sigma$, $D = \frac{\gamma^2\zeta^2}{9\Delta}$, and $S_1 = S_2 = 3/2$. The exchange interaction retains the isotropic form, while the effect of spin-orbit coupling is a positive zero-field splitting.

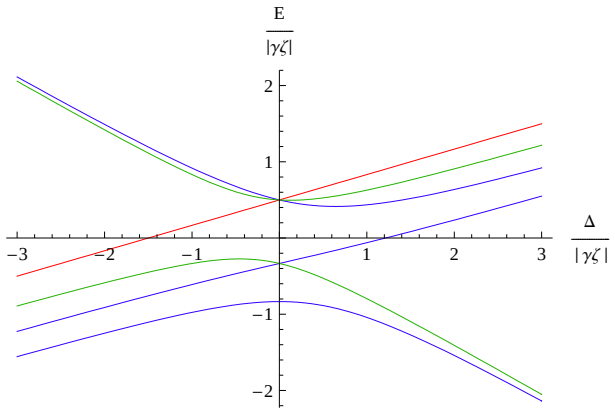

Figure 3.4: Spectrum of the uncoupled Co^{II} ions (Hamiltonian Eq. (3.2.1)) as a function of the tetragonal splitting Δ. (Adapted from [12].) The $^4T_1$ ground state is split by spin-orbit coupling and a tetragonal ligand field in six Kramers doublets, each of which is represented by a single line in the figure. States are identified by the rotational quantum number M_J. Blue: $M_J = \pm 1/2$, green: $M_J = \pm 3/2$, red: $M_J = \pm 5/2$.

For the second case, we set $\Delta = 0$. The intra-site Hamiltonian Eq. (3.2.1) has now spherical symmetry. The eigenstates correspond to quantum numbers of total angular momentum $J = 5/2$, $3/2$, and $1/2$, separated according to the Landé interval rule. The ground state is the doublet $J = 1/2$ (Fig. 3.4). If we assign to this state an effective spin, $\tilde{s} = 1/2$, and evaluate the exchange interaction to first order, we obtain the exchange Hamiltonian in a four-dimensional space:

$$\hat{H} = J\hat{\tilde{\mathbf{s}}}_1 \cdot \hat{\tilde{\mathbf{s}}}_2, \tag{3.3.1}$$

where $J = \frac{25}{9} J_\sigma$, as one can find from the Landé g factor. Again, the isotropic form of the exchange coupling is retained, although in another space.

In the third case, Δ is large and negative, whereby the ground state has orbital momentum along the z axis (^4E in the point group C_4). Spin-orbit coupling splits this state in four equidistant doublets (Fig. 3.4), the lowest of which consists of the states $|M_L M_S\rangle = |-1\ \tfrac{3}{2}\rangle$ and $|1\ -\tfrac{3}{2}\rangle$. These are assigned as respectively $\tilde{s}_z = +1/2$ and $\tilde{s}_z = -1/2$ components of an effective $\tilde{s} = 1/2$ spin. The exchange Hamiltonian is found to be (again in a four dimensional space):

$$\hat{H} = J\hat{\tilde{s}}_{1z}\hat{\tilde{s}}_{2z}, \tag{3.3.2}$$

with $J = 9J_\sigma$. In contrast to the previous case (Eq. (3.3.1)), this Hamiltonian is of the anisotropic Ising type. In general, for $\Delta < 0$, the exchange Hamiltonian

will be a linear combination of an isotropic (Eq. (3.3.1)) and an anisotropic (Eq. (3.3.2)) part.

The parent Hamiltonian Eq. (3.2.2) contains thus as limiting cases a variety of interactions in a more familiar form, ranging from isotropic spin-spin coupling with zero-field splitting to the anisotropic Ising Hamiltonian. We want to emphasize again that, for these derivations, the exchange interaction was supposed to be small with respect to the interactions on the single cobalt sites. Only then can the lowest eigenstates of each cobalt site form a good model space for an exchange Hamiltonian with reduced dimensions. We will find in the next section that such an approximation can not be made for the $[Co_2PdCl_2(dpa)_4]$ complex so that a spin-only Hamiltonian, as was used in Ref. [1], is not adequate here.

3.4 Magnetic susceptibility of $[Co_2PdCl_2(dpa)_4]$

Properties dependent on temperature are calculated by diagonalizing Hamiltonian (3.2.2) and applying Boltzmann statistics. The spin-orbit coupling constant ζ is taken to be 500 cm^{-1} [12]. The three unknowns that are left (Δ, γ, and J_σ) should be determined from comparison with experiment, remembering the restriction on γ discussed in Section 3.2.

The procedure is applied to the average magnetic susceptibility of $[Co_2PdCl_2(dpa)_4]$, for which experimental data are available [1]. The best correspondence is obtained with the following parameters[1]:

$$|\Delta| = 100\,cm^{-1},\ J_\sigma = 100\,cm^{-1},\ \gamma = -1.1 \tag{3.4.1}$$

The corresponding plots of χ and χT are presented in Fig. 3.5, together with the experimental curves. The value found for γ is typical for high-spin Co^{II} complexes [11, 13]. We should note here that the effect of changing γ was found to be merely a shift of χ, almost independent of temperature. The essential form of χ depends thus on the values of J_σ and Δ alone. The exchange constant J_σ is strongly antiferromagnetic, as we expected (see Section 3.2). On the other hand, the tetragonal ligand-field splitting Δ is smaller than expected, considering the highly heterogeneous coordination environment of the Co ions. The sign of Δ will be commented on later.

From Fig. 3.5 it is clear that the calculated χ values at low temperature are incompatible with the steep increase of the experimental χ and support thereby the conclusion that this increase is due to a paramagnetic impurity in the sample [1]. The most important result however, is to be inferred from the

[1] These parameters were not determined by a least-square fitting but only by visual comparison. A more precise fitting is unnecessary for the present purpose.

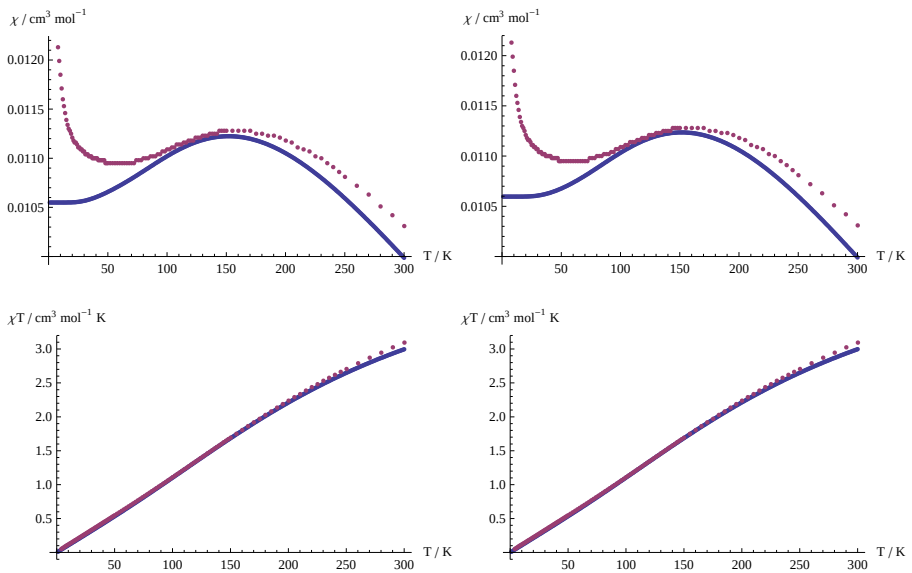

(a) $\Delta = +100\ \mathrm{cm}^{-1}$ (b) $\Delta = -100\ \mathrm{cm}^{-1}$

Figure 3.5: Calculated (blue) and experimental [1] (red) magnetic susceptibility curves of $[Co_2PdCl_2(dpa)_4]$ as a function of the temperature. The sign of Δ can not be determined from this comparison. The calculated susceptibility confirms that the steep increase of the experimental susceptibility below 50 K has to be attributed to a paramagnetic impurity in the sample [1]. ($J_\sigma = 100\,\mathrm{cm}^{-1}$, $\zeta = 500\,\mathrm{cm}^{-1}$, and $\gamma = -1.1$)

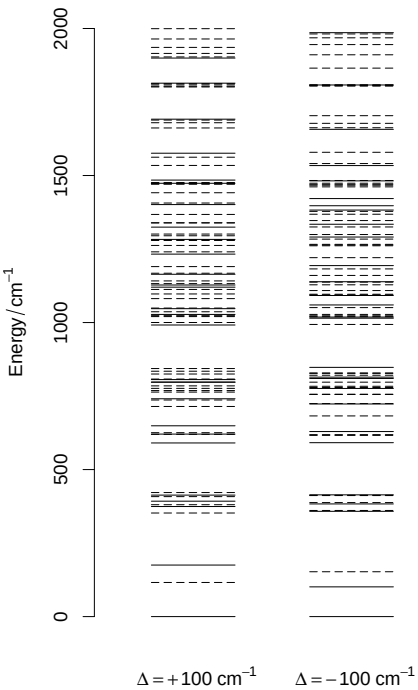

Figure 3.6: Energy levels of the model Hamiltonian (3.2.2) in a zero magnetic field. Full lines represent nondegenerate levels, and dashed lines represent twofold degenerate levels ($J_\sigma = 100\,\mathrm{cm}^{-1}$, $\zeta = 500\,\mathrm{cm}^{-1}$, and $\gamma = -1.1$).

curves of χT in Fig. 3.5; the linearity of χT points to a strong temperature independent paramagnetism (TIP) in the compound, extending over the whole temperature range. This behavior is recovered completely by the theoretical model. The value of the TIP in this compound is about 0.01 $\mathrm{cm}^3\,\mathrm{mol}^{-1}$, which is 100 times larger than common values in mononuclear complexes [17].

To clarify the TIP behavior, we refer to a plot of the energy levels in Fig. 3.6. The three lowest levels, one of which is twofold degenerate, are clearly separated from higher levels. In the range of temperatures considered here (below 300 K), only these three ground levels are populated appreciably, and their properties will therefore determine the observed magnetism.

A qualitative understanding of the origin of these states can be gained by considering the limit of weak exchange coupling (J_σ small). With $|\Delta|$=100 cm^{-1}, we are in a regime very close to the octahedral limit (center of Fig. 3.4). According to the discussion in Section 3.3, an effective Hamiltonian can be

written that couples the ground-state Kramers doublets on each cobalt site:

$$\hat{H} = J_a \hat{\tilde{\mathbf{s}}}_1 \cdot \hat{\tilde{\mathbf{s}}}_2 + J_b \hat{\tilde{s}}_{1z} \hat{\tilde{s}}_{2z}. \tag{3.4.2}$$

The J_a term couples the doublets spherically in a triplet state and a singlet ground state (the exchange is still antiferromagnetic). The J_b term results from the deviation from octahedral symmetry, and splits the triplet in rotational components $m_{\tilde{s}} = 0$ and $m_{\tilde{s}} = \pm 1$. A perturbational approach shows that [10] $J_b = -\frac{40}{9}\frac{\Delta}{|\gamma\zeta|}J_\sigma$. This expression, which is correct in the weak exchange limit, predicts that the relative order of the second and third level depends on the sign of Δ. This same ordering is found in the present case of strong exchange coupling (Fig. 3.6). At least formally then, the lowest energy levels can be described by the Hamiltonian (3.4.2), although the composition of the states is certainly not the one implied by the weak-coupling limit: the strong exchange interaction ($J_\sigma \hat{\mathbf{S}}_1 \cdot \hat{\mathbf{S}}_2$) will mix the ground Kramers doublets on the cobalt sites to an important extent with higher doublets. The model space of Hamiltonian (3.4.2), consisting only of the ground-state Kramers doublets, is therefore incapable of representing the real states accurately. In this respect, the effective Hamiltonian (3.4.2) is not considered to be appropriate for the present system.

To exemplify the deviation from the weak-coupling limit, we consider the z component[2] of the magnetic moment in the twofold degenerate level ($m_{\tilde{s}} = \pm 1$). Fig. 3.7 shows how this moment decreases with an increase in the strength of the exchange interaction: from 3.6 μ_B at $J_\sigma = 0$ cm^{-1} (that is, for two independent cobalt ions) to 0.7 μ_B at $J_\sigma = 100$ cm^{-1}, a quenching that is to be attributed to the tendency of the antiferromagnetic exchange interaction to align the spin moments antiparallel (and, through spin-orbit coupling, also the orbital moments). The strong reduction of this magnetic moment is part of the explanation of the TIP behavior, to which we come now.

The magnetic properties of the lowest levels are most conveniently analyzed with the help of the Van Vleck equation, which expresses the susceptibility in terms of the zero-field molecular states:

$$\chi = \frac{1}{3}\frac{N_A}{\sum_n g_n e^{-\varepsilon_n/kT}} \times \sum_{\alpha=x,y,z} \sum_n \left(\sum_{i,j\in\{n\}} \frac{|\langle n_i|\hat{\mu}_\alpha|n_j\rangle|^2}{kT} + 2\sum_{m\neq n} \sum_{\substack{i\in\{n\} \\ j\in\{m\}}} \frac{|\langle n_i|\hat{\mu}_\alpha|m_j\rangle|^2}{\varepsilon_m - \varepsilon_n} \right) e^{-\varepsilon_n/kT}$$

The term between brackets denotes the susceptibility of one level $\{n\}$ with degeneracy g_n and energy ε_n. It is a sum of two parts: the first is due to

[2] Because of the symmetry of the molecule, x and y components of the magnetic moment vanish in every state.

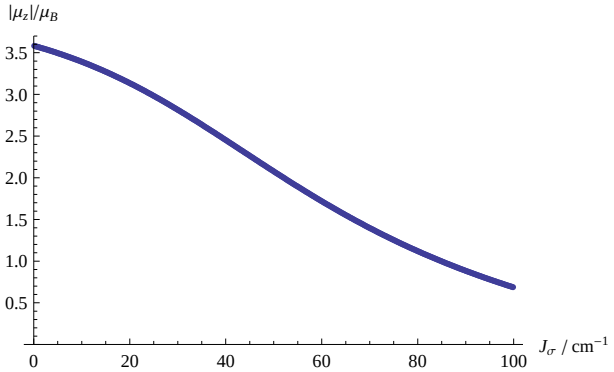

Figure 3.7: z component of the magnetic moment of the lowest twofold degenerate state of Hamiltonian (3.2.2) in a zero magnetic field, as a function of the antiferromagnetic exchange interaction ($\Delta = +100\,\mathrm{cm}^{-1}$, $\zeta = 500\,\mathrm{cm}^{-1}$, and $\gamma = -1.1$)

permanent magnetic moments in the level and is inversely proportional to temperature (note that permament magnetic moments are only possible in degenerate levels, i.e. for $g_n \geq 2$); the second part is due to magnetic moments that are *induced* by the magnetic field. TIP is usually due to the latter part, when only the ground state is thermally occupied [17]. In the present case, however, we have seen that two more levels can be populated, one of which is twofold degenerate. The fact that the TIP is hardly affected by these states is explained by two observations: first, the susceptibility due to induced magnetic moments is almost the same in these levels and has a value of ≈ 0.01 cm^3 mol^{-1}. Second, the permanent magnetic moment in the degenerate level is small ($\approx 0.7\ \mu_B$, see Fig. 3.7). At the temperatures where this level becomes populated, the contribution of this moment to the susceptibility is small in comparison with the 0.01 cm^3 mol^{-1} of the induced moments; it does contribute to the maximum of χ at 150 K, which is only about 7 % higher than the value at 0 K (Fig. 3.5). In the χT curve, this deviation is hardly noticed. We understand here that the quenching of the magnetic moment in the degenerate level, as described in the previous paragraph, is essential for the manifestation of the TIP behavior. Overall, we conclude that the magnetic susceptibility is dominated by the contribution of the induced magnetic moments, which are equal in the thermally occupied states, resulting in a temperature-independent behavior. Fig. 3.8 illustrates that the contribution of the induced magnetic moments is by far the most important: the susceptibility due to the permanent moments (red curve) is very small in comparison with the total susceptibility (blue curve).

It is important to note that the large TIP can not solely be attributed to the coupling of the Co^{II} ions. In fact, a TIP contribution of the same order

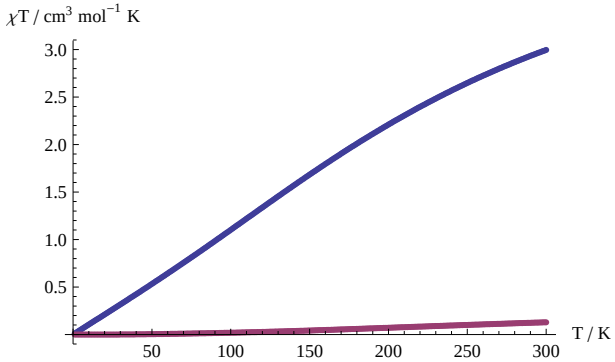

Figure 3.8: Contributions to the calculated magnetic susceptibility. The blue curve is the total χT, the red curve is the part of χT due to permanent magnetic moments. The difference equals the contribution of the induced magnetic moments ($\Delta = +100\,\mathrm{cm}^{-1}$, $J_\sigma = 100\,\mathrm{cm}^{-1}$, $\zeta = 500\,\mathrm{cm}^{-1}$, and $\gamma = -1.1$).

of magnitude is already present in free, octahedral high-spin Co^{II} complexes. There, χT is linear up to ≈ 100 K and flattens at higher temperatures due to population of the $J = 3/2$ level [11]. The origin of this TIP is the induced magnetic moments in the ground-state $J = 1/2$ level. The peculiarity of the present dimer lies in the fact that the TIP behavior is extended over the whole experimental temperature range, making it more manifest.

As was indicated in Eq. (3.4.1), the sign of Δ could not be determined from the comparison with experiment. This is clear from Fig. 3.5, where we show the calculated curves for positive Δ on the left and those for negative Δ on the right. A differentiation between both cases can only be made by looking at the components of χ along the molecular Z axis and perpendicular to it, as shown in Fig. 3.9, where the calculated components are plotted for both signs of Δ. The magnetic anisotropy $(\chi_{||} - \chi_\perp)$ is clearly dependent on the sign of Δ, although the average susceptibility $\chi = \frac{\chi_{||}+2\chi_\perp}{3}$ does not change. Note that, for Δ=$-$100 cm^{-1}, the anisotropy is also predicted to change sign as a function of temperature. Unfortunately, there are no experimental data to confront these predictions with. Oriented crystal measurements on this compound would provide information that could lead to a more decisive test of the theoretical model.

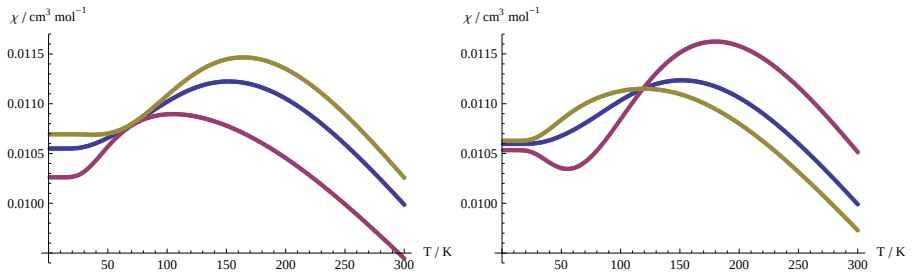

(a) $\Delta = +100\ \mathrm{cm}^{-1}$ (b) $\Delta = -100\ \mathrm{cm}^{-1}$

Figure 3.9: Calculated componenents of magnetic susceptibility: $\chi_{||}$ (red), $\chi_{\perp}$ (yellow), and χ (blue) ($J_\sigma = 100\,\mathrm{cm}^{-1}$, $\zeta = 500\,\mathrm{cm}^{-1}$, and $\gamma = -1.1$).

3.5 Conclusion

From a microscopic approach to the electronic structure of $[Co_2PdCl_2(dpa)_4]$ we have derived a model Hamiltonian that takes into account both spin and orbital degeneracy of the Co^{II} ions. By considering the nonmagnetic Pd^{II} ion as a ligand that transfers exchange interaction between the Co^{II} ions, the dominant contribution to the exchange Hamiltonian was found to be of the isotropic Heisenberg type between real spins. The calculated magnetic susceptibility shows a satisfactory agreement with experiment. In particular, the strong temperature-independent paramagnetism is recovered completely (Fig. 3.5). The parameters derived from this comparison confirm that the Co ions are coupled by a strong antiferromagnetic exchange interaction [1]. The tetragonal ligand field splitting was found to be small ($|\Delta| = 100\ \mathrm{cm}^{-1}$) and its sign could not be determined from the available experimental data.

The observed TIP in this complex results from a quenching of permanent magnetic moments together with an almost constant magnetic polarizibility in thermally populated levels. This should be contrasted with the usual origin of TIP, which is a nonmagnetic ground state, thermally isolated from excited states.

It should be emphasized that to explain the magnetism of this compound, a conventional spin-only Hamiltonian is not appropriate. The relative strength of the interactions do not allow for a reduction of the size of the model space. The lack of a generic spin-Hamiltonian approach remains a major problem in the study of magnetic compounds with unquenched orbital momenta.

Although Co^{II} is known for its highly anisotropic behavior, this property does not emerge in the compound studied in this paper. The reason is that Δ,

which is the only parameter in Eq. (3.2.2) that induces anisotropy, is too small: its effect is quenched by the strong exchange interaction, which is isotropic (Eq. (3.2.2)). To obtain strong magnetic anisotropy, Δ should be made large and negative. On the other hand, if the σ-exchange pathway can be eliminated by suitable choice of ligands, while retaining the π-exchange pathways, the exchange Hamiltonian will be anisotropic, and the Heisenberg Hamiltonian will be inadequate.

Bibliography

[1] M.-M. Rohmer, I. P.-C. Liu, J.-C. Lin, M.-J. Chiu, C.-H. Lee, G.-H. Lee, M. Bénard, X. López, and S.-M. Peng, Angew. Chem. Int. Ed. **46**, 3533 (2007)

[2] D. Gatteschi, R. Sessoli, and J. Villain, *Molecular Nanomagnets* (Oxford University Press, Oxford, 2006)

[3] P. W. Anderson, Phys. Rev. **115**, 2 (1959)

[4] K. I. Kugel and D. I. Khomskii, Sov. Phys. Usp. **25**, 231 (1982)

[5] Y. Tokura and N. Nagaosa, Science **288**, 462 (2000)

[6] P. D. W. Boyd, M. Gerloch, J. H. Harding, and R. G. Woolley, Proc. R. Soc. Lond. A. **360**, 161 (1978)

[7] A. Ceulemans, L. F. Chibotaru, G. A. Heylen, K. Pierloot, and L. G. Vanquickenborne, Chem. Rev. **100**, 787 (2000)

[8] V. S. Mironov, L. F. Chibotaru, and A. Ceulemans, J. Am. Chem. Soc. **125**, 9750 (2003)

[9] J. J. Borrás-Almenar, J. M. Clemente-Juan, E. Coronado, A. V. Palii, and B. S. Tsukerblat, J. Phys. Chem. A **102**, 200 (1998)

[10] A. V. Palii, B. S. Tsukerblat, E. Coronado, J. M. Clemente-Juan, and J. J. Borrás-Almenar, J. Chem. Phys. **118**, 5566 (2003)

[11] F. Lloret, M. Julve, J. Cano, R. Ruiz-Garcia, and E. Pardo, Inorg. Chim. Acta **361**, 3432 (2008)

[12] J. S. Griffith, *The Theory of Transition-Metal Ions* (Cambridge University Press, Cambridge, 1964)

[13] J. M. Herrera, A. Bleuzen, Y. Dromzée, M. Julve, F. Lloret, and M. Verdaguer, Inorg. Chem. **42**, 7052 (2003)

[14] L. F. Chibotaru, J.-J. Girerd, G. Blondin, T. Glaser, and K. Wieghardt, J. Am. Chem. Soc. **125**, 12615 (2003)

[15] I. P.-C. Liu, G.-H. Lee, S.-M. Peng, M. Bénard, and M.-M. Rohmer, Inorg. Chem. **46**, 9602 (2007)

[16] M. E. Lines, J. Chem. Phys. **55**, 2977 (1971)

[17] O. Kahn, *Molecular Magnetism* (VCH Publishers, New York, 1993)

Chapter 4

The decorated Ising chain in molecular magnetism

Abstract The application of the bond-decorated Ising model [1] to magnetic chains and rings containing lanthanide ions is investigated. The lanthanide plays the role of Ising ion. The required conditions on the crystal-field spectrum of the lanthanide ion for the model to be valid are discussed and found to be in agreement with several recent *ab initio* calculations on Dy^{3+} centers. The magnetic properties of two actual examples (a $[DyCuMoCu]_\infty$ chain [2] and a Dy_4Cr_4 ring [3]) in arbitrarily directed magnetic field are obtained by a transfer-matrix solution of the decorated Ising model. g-factors of the metal ions are directly imported from *ab initio* results, while exchange coupling constants are fitted to experiment. Agreement with experiment is found to be good to satisfactory, if one includes a correction (from *ab initio* results) for susceptibility (and sometimes also magnetization) to account for the presence of excited Kramers doublets on Dy^{3+}. A parallel is drawn between the spectrum of the simple and the decorated Ising chain.

4.1 Introduction

In a 1959 paper M. E. Fisher introduced the general bond-decorated Ising model as one example of a set of exactly solvable transformations of spin-1/2 Ising models [1]. A bond-decorated Ising model has an "arbitrary statistical mechanical system" inserted in every original Ising bond. The partition function of this decorated model is related to the partition function of the original or bare Ising model by the addition of a prefactor and a renormalization of the

W. Van den Heuvel and L. F. Chibotaru, unpublished manuscript

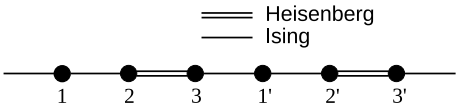

Figure 4.1: The Ising-Heisenberg chain discussed in Ref. [4] (showing only two unit cells). The bonds of the Ising chain (1-1'-1"- ...) are decorated with Heisenberg dimers (2-3), (2'-3'), ... The partition function of this chain is exactly solvable.

coupling constants and magnetic moments (the Ising model is supposed to be in a parallel magnetic field). Knowledge of the partition function of a given Ising model thus allows one to obtain the partition function of any bond-decorated version of that Ising model.

More recently, Strečka and Jaščur have used the method of bond-decoration to investigate the thermodynamics of mixed Ising-Heisenberg chains in parallel magnetic fields where the decorating unit is a spin dimer or trimer with anisotropic Heisenberg coupling (see Fig. 4.1) [4, 5]. The partition function of these chains is readily obtained from the known partition function of the Ising chain and the energy levels of the decorating unit. Therefore they could calculate exact magnetic properties and theoretically show, for example, the existence of magnetization plateaus in certain bond-alternating chains.

The convenience of the decorated Ising chain as a theoretical model for spin chains derives of course from the relative ease with wich exact solutions are obtained, in contrast for example with the pure Heisenberg chain, for which no exact partition function has been found. Up to now, this property of solvability has been the prime motive for the study of these chains in the literature. Indeed, in Ref. [4] the decorated Ising chain was considered as a substitute for the intractable Heisenberg model, and in Ref. [5] the principle reason for the introduction of Ising bonds—to replace the more reasonable Heisenberg bonds—in a chain of Cu^{2+} ions appears to have been the desire to obtain a solvable model. This approach can be applied to any type of Heisenberg chain with a repeating unit: replace enough—preferably ferromagnetic—Heisenberg bonds by Ising bonds to obtain a decorated Ising chain that is solved easily and, in some cases, exhibits thermodynamic properties that are qualitatively comparable with those of the original chain [6, 7].

However, the role of the decorated Ising chain in the field of one-dimensional magnetism is not confined to that of simplification of realistic quantum spin chains. In this paper we show that some new molecular rings and chains are real examples of decorated Ising systems. Concretely, we treat a [DyCuMoCu] infinite chain [2] and a $(DyCr)_4$ tetrameric ring [3]. These compounds were recently synthesized in the course of the ongoing synthetic efforts to make new

and better single-chain magnets (SCMs) and single-molecule magnets (SMMs), whose characteristic property is a blocking or slow relaxation of magnetization at low temperatures.[1] We will not be concerned here with these dynamic aspects of their magnetism but only with their static magnetic properties. A necessary property of SMMs and SCMs is a magnetic anisotropy, or some preferred direction of the magnetic moment. One line of approach is to introduce anisotropy by means of lanthanide ions, whether or not in combination with transition metal ions [10, 11]. The two compounds considered here are products of this approach, with dysprosium as lanthanide ion.

The Dy^{3+} ion plays a crucial role in these systems; it depends on the ground state of this ion in its ligand environment whether the system is a decorated Ising system or not and consequently, whether its partition function is exactly solvable or not. The ground Kramers doublet of Dy^{3+} must have complete uniaxial magnetic anisotropy[2] and must be separated from excited Kramers doublets by an amount that is large compared with the exchange coupling (typically, this separation must be 100 cm^{-1} or more). The required information on the ground and excited doublets of the Dy^{3+} monomer can be derived from *ab initio* calculations on the monomer complex, isolated from the polynuclear compound [2, 3].

The [DyCuMoCu] chain and the $(DyCr)_4$ ring are shown to be decorated Ising chains in an arbitrarily directed magnetic field. The magnetic properties, in particular powder magnetization and susceptibility, are calculated with the help of the transfer-matrix method, which is a bit more general and convenient for numerical computation than the renormalization of the Ising parameters, which was used by Fisher and also Strečka and Jaščur. The results compare reasonably well with experiment and allow to determine values for the exchange coupling constants. At higher temperatures, the excited Kramers doublets (or Stark levels) of Dy^{3+} contribute to the magnetism. This is corrected for in an approximate way by adding this contribution, calculated *ab initio* for the monomeric complex, to the results of the decorated Ising model.

4.2 Theoretical Background

4.2.1 Decorated Ising chain and transfer matrix solution

The decorated Ising chain may be divided into units delimited by the Ising spins, as in Fig. 4.2. The Hamiltonian of the decorated Ising chain (or ring) of

[1] For single molecule magnetism see [8], for single chain magnetism see [9].

[2] By complete uniaxial anisotropy we mean that only one g-factor of the Kramers doublet is not zero; for example $g_x = g_y = 0$ and $g_z \neq 0$.

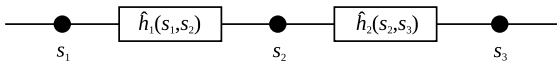

Figure 4.2: Part of the decorated Ising chain. In each Ising bond is inserted an arbitrary statistical mechanical system [1] or decorating unit that interacts only with the two Ising spins s_i at the vertices of the bond. The Ising spin variables commute with the Hamiltonian and have definite values in the eigenstates of the chain.

length n may accordingly be written as follows:

$$\hat{H} = \hat{h}_1(s_1, s_2) + \hat{h}_2(s_2, s_3) + \hat{h}_3(s_3, s_4) + \ldots + \hat{h}_n(s_n, s_{n+1}), \tag{4.2.1}$$

where the subhamiltonians $\hat{h}_i$ correspond to units of the chain. If the chain is closed into a ring, periodic boundary conditions apply by identifying the last with the first spin: $s_{n+1} \equiv s_1$. The Ising spins s_i commute with the subhamiltonians and the subhamiltonians commute with each other:

$$[s_i, \hat{h}_j] = 0 \quad \text{and} \quad [\hat{h}_i, \hat{h}_j] = 0. \tag{4.2.2}$$

It is further assumed that there is no direct interaction between the decorating units themselves, i.e. two different $\hat{h}_i$ have no variables in common, except for an s_i when they are neighbors. In writing Eq. (4.2.1) we made use of the fact that the Ising spins are conserved variables and may be considered as parameters rather than operators. In the case of spin-1/2, they take on the values $+1/2$ and $-1/2$, so that to each decorating unit there correspond 4 different subhamiltonians $\hat{h}_i(s_i, s_{i+1})$.[3]

Since there is no direct interaction between the decorating units of the chain, the subhamiltonians $\hat{h}_i$ in Eq. (4.2.1) work—for a given set of s_i values—on disjunct spaces. An eigenfunction of $\hat{H}$ is then simply a direct product of n independent eigenfunctions, one of each $\hat{h}_i$. The corresponding energy is:

$$E = \varepsilon_{1k_1}(s_1, s_2) + \varepsilon_{2k_2}(s_2, s_3) + \varepsilon_{3k_3}(s_3, s_4) + \ldots + \varepsilon_{nk_n}(s_n, s_{n+1}), \tag{4.2.3}$$

where $\varepsilon_{ik_i}(s_i, s_{i+1})$ is the k_i-th energy level of $\hat{h}_i(s_i, s_{i+1})$.

Following Ref. [1] we write the partition function of one decorating unit for fixed s_i and s_{i+1} on the bond vertices:

$$\psi_i(s_i, s_{i+1}) = \sum_k \exp[-\beta\varepsilon_{ik}(s_i, s_{i+1})], \tag{4.2.4}$$

[3] In what follows, no use is made of the angular momentum properties of the s_i. In fact, any parameter that takes on a finite number of values can serve as s_i in Eq. (4.2.1). In practice however, s_i represents most commonly a Kramers doublet, which is most often described as an effective spin-1/2. This is the case for the examples considered in this paper.

where $\beta = 1/kT$. The total partition function for the chain is then given by

$$\mathcal{Z}_n = \sum_{s_1, s_2, \ldots, s_{n+1}} \psi_1(s_1, s_2)\psi_2(s_2, s_3)\ldots\psi_n(s_n, s_{n+1}). \tag{4.2.5}$$

This is the well-known form of a transfer-matrix solution [12]. Each decorated bond (or pair of neighboring Ising spins) is represented by a transfer matrix T_i whose elements are the $\psi_i(s_i, s_{i+1})$, the values of s_i labeling the rows and the values of s_{i+1} labeling the columns. Explicitly for the spin-1/2 decorated Ising chain:

$$T_i = \begin{pmatrix} \psi_i(+\frac{1}{2}, +\frac{1}{2}) & \psi_i(+\frac{1}{2}, -\frac{1}{2}) \\ \psi_i(-\frac{1}{2}, +\frac{1}{2}) & \psi_i(-\frac{1}{2}, -\frac{1}{2}) \end{pmatrix} \tag{4.2.6}$$

Since most applications deal either with rings or very long chains, the boundaries can be identified ($s_{n+1} \equiv s_1$) and expression (4.2.5) can be written as the trace of a matrix product:

$$\mathcal{Z}_n = \mathrm{Tr}(T_1 T_2 \ldots T_n). \tag{4.2.7}$$

This is the most general expression for the partition function of a decorated Ising chain. If the chain has translational symmetry the partition function is expressed in terms of eigenvalues [12]. Suppose that the chain is a repetition of identical decorated Ising bonds, then the T_i are all the same, so that

$$\mathcal{Z}_n = \mathrm{Tr}(T_1^n) = \sum_i \lambda_i^n, \tag{4.2.8}$$

where the λ_i are the eigenvalues of T_1. According to Perron's theorem on positive matrices, the eigenvalue λ_0 with largest modulus is real, positive and nondegenerate [13]. This yields the simple but exact result for the free energy per unit cell of the infinite chain:

$$f = -kT \lim_{n\to\infty} \frac{\ln \mathcal{Z}_n}{n} = -kT \ln \lambda_0. \tag{4.2.9}$$

If a unit cell of the chain is spanned by p decorated bonds instead of one then it is only necessary to combine p transfer matrices into one new transfer matrix $\widetilde{T} = T_1 T_2 \ldots T_p$, with largest eigenvalue $\tilde{\lambda}_0$, to be used in Eqs. (4.2.8) and (4.2.9), with n replaced by n/p. This situation arises, for example, when the local easy axes on the Ising ions are not parallel but canted with respect to each other.

The solution in terms of transfer matrices, Eq. (4.2.7), is not limited to decorated spin-1/2 Ising chains. It is valid for chains having Ising spins of any multiplicity or a combination of Ising spins with different multiplicities, in wich case the dimension of the transfer matrix is different from two by two. This demonstrates that the transfer matrix is more versatile than the method of renormalization of Ising Hamiltonian parameters, which is limited to the spin-1/2 case by the

number of available parameters [1]. For the moment however, the possibility to include Ising spins of higher multiplicity is only of theoretical interest, since no molecular realizations of such systems are known. Another advantage of the transfer matrix method is that it can be readily extended to include next-neirest neighbor bonds between the Ising spins. To this end, the transfer matrix has to be enlarged so that it does not jump from one Ising spin to the next, but from one *pair* of Ising spins to the next pair [12].

4.2.2 Dy^{3+} as Ising spin

We are interested in this paper in molecular chains or rings that can be described by a decorated Ising model. This means that their low-energy spectrum can be modeled to satisfactory accuracy by an effective Hamiltonian that has the properties described in Section 4.2.1. It has been noted there that the composition of the decorating unit is basically arbitrary and we need therefore not consider the properties of that part. Instead, our attention goes here to the molecular realization of the Ising spin (s_i in Eq. (4.2.1)). We focus on Dy^{3+} because this ion is used in the two examples studied below, but the discussion applies equally well to several other trivalent lanthanides and possibly also to some heavy transition metal ions.

It is known that lanthanide ions in a coordination environment are often well described by crystal field theory applied to the ground $|LSJ\rangle$ level. One assumes that J, L, and S remain good quantum numbers. Dy^{3+} is a Kramers ion that belongs to the second half of the lanthanide series, whose ground level is ${}^6\mathrm{H}_{15/2}$ (f^9), with associated Landé factor $g = 4/3$. This multiplet splits into 8 Kramers doublets by the crystal field perturbation (except for high-symmetric environments belonging to the T, O, or K point groups, which split the multiplet in less than 8 levels). It will be useful to view each Kramers doublet as an effective spin-1/2 with its own g-factors (3 in number) and corresponding magnetic axes. For example, take the Kramers doublet $|M_J = \pm 15/2\rangle$ (of the ${}^6\mathrm{H}_{15/2}$ level), quantized with respect to the z axis. Its g factors are $g_z = 2(4/3)(15/2) = 20$ and $g_x = g_y = 0$.

If the action of the crystal field on Dy^{3+} is such that the lowest Kramers doublet is separated from the next one by an energy that is large compared to the energy of interaction with the magnetic field and the exchange interaction with neighboring ions, we can omit all excited Kramers doublets from the Hamiltonian and keep only the lowest doublet. In this way Dy^{3+} is described by a spin of 1/2 and every interaction in which it takes part enters the Hamiltonian as a linear combination of the three spin operators s_x, s_y, and s_z.[4] If we now

[4]Linear combination in a general sense: the coefficients of the expansion may be operators working in other spaces.

want Dy^{3+} to be an Ising spin, defined by the first commutation relation in Eq. (4.2.2), it is clear that only one of these spin components, say s_z or simply s, may actually appear in the Hamiltonian. In other words, there must be no interaction that creates an off-diagonal matrix element between the two components of the Kramers doublet (because the Pauli matrix of s_z is diagonal). This can be shown to be true with high accuracy if the lowest Kramers doublet is $|M_J = \pm 15/2\rangle$.

The two interactions of importance here are the Zeeman interaction with the magnetic field and the exchange interaction with other magnetic ions. The Zeeman Hamiltonian follows directly from the g factors of the Kramers doublet (vide supra), and is

$$-\mu_{\mathrm{B}} g_z s_z B_z, \tag{4.2.10}$$

where B_z is the the z component of the applied magnetic field. Note that the field may be applied in any direction, but it is only the z component that interacts with the Kramers doublet because $g_x = g_y = 0$. The vanishing of g_x and g_y in $|M_J = \pm 15/2\rangle$ follows from the selection rule stating that a vector operator (the magnetic moment in this case) cannot connect states for which M_J differs by more than one unit. We will sometimes refer to the z axis as the anisotropy axis, to stress that it is the only magnetic axis with nonvanishing g factor.

To evaluate the effect of exchange interaction, we must first take a closer look at the composition of the Kramers doublet. In terms of the Russel-Saunders states $|M_S\rangle|M_L\rangle$ we have

$$\begin{aligned} |+15/2\rangle &= |+5/2\rangle|+5\rangle \\ |-15/2\rangle &= |-5/2\rangle|-5\rangle. \end{aligned} \tag{4.2.11}$$

In a basic (super)exchange process between two magnetic centers, one electron of each center takes part. If we look at one center, the process removes an electron with certain spin projection (up or down) and puts it back on the center either with the same or with opposite spin projection [14]. This gives rise to the selection rule $\Delta M_S = 0, \pm 1$. If the exchange interaction is to connect both components of the Kramers doublet in Eq. (4.2.11), at least five successive processes are needed, for $\Delta M_S = \pm 5$. In other words, not one but five electron spins have to be flipped to connect $|+15/2\rangle$ with $|-15/2\rangle$. If the basic exchange process (i.e. the one for which $\Delta M_S = 0, \pm 1$) occurs in, say, kth order[5] of perturbation theory then an off-diagonal matrix element between the two components can only appear in $(5k)$th order of perturbation theory. It is therefore reasonable to assume that the off-diagonal matrix element is negligibly small compared to the diagonal matrix elements ($\Delta M_S = 0$) so that the effect

[5]For example, "potential exchange" in 1st order, "kinetic exchange" in 2nd order, etc.

of exchange interaction on the Kramers doublet is accurately described by the s_z spin operator only.

Note that we derived the selection rule for exchange interaction on the basis of the spin quantum number M_S only, without paying attention to the angular momentum quantum number M_L, although M_L changes even more than M_S between the states of the Kramers doublet (4.2.11). The existence and precise form of a selection rule for M_L depends on the spatial symmetry of the exchange problem under consideration. ΔM_L is therefore not as useful as ΔM_S for predicting the vanishing of certain matrix elements of exchange interaction. Note however that, even in the lowest symmetry, there is a maximum to the amount that M_L can change in the basic exchange process described in the previous paragraph: within the f orbitals, a one-electron process can bring about at most a change of $\Delta M_L = \pm 6$. So we would have, in general, that a basic exchange process can induce the following changes in a lanthanide state:

$$\begin{aligned} &\Delta M_S = 0, \pm 1 \\ &|\Delta M_L| \leq 6. \end{aligned} \tag{4.2.12}$$

Thus at least two steps of this kind are needed to bridge $\Delta M_L = \pm 10$, but at least five are needed to bridge $\Delta M_S = \pm 5$. So in this case, the selection rule of M_S gives the stronger result and leads to the conclusions—reached in the last paragraph—on the matrix elements of exchange interaction in the Kramers doublet (4.2.11).

We can now derive the precise form of that part of the effective Hamiltonian that refers to the exchange interaction between a Dy^{3+} ion (with ground state (4.2.11)) and another magnetic center. We consider two cases, which we shall encounter in the examples in Sections 4.3 and 4.4: in the first case the other center is another Dy^{3+} ion; in the second case the other center is an ion with an isotropic spin moment $\mathbf{S}$. Consider first the exchange interaction with another Dy^{3+} ion. We assume that the second Dy^{3+} has the same property of uniaxiality as the first one and that it also shares all other relevant properties discussed in the previous paragraphs. Then both ions are represented by a spin-1/2 doublet with a local anisotropy axis $\hat{\mathbf{z}}_i$ ($i = 1, 2$) and we already know that the effect of exchange interaction in each doublet is proportional to s_{z_i}. Therefore the exchange Hamiltonian is necessarily of the form

$$-J s_{z_1} s_{z_2}, \tag{4.2.13}$$

where it is understood that the first spin belongs to ion 1 and the second to ion 2. Note that $\hat{\mathbf{z}}_1$ and $\hat{\mathbf{z}}_2$ need not be parallel with each other.

As a second case, consider the interaction between Dy^{3+} (anisotropy axis $\hat{\mathbf{z}}_1$) and an isotropic spin $\mathbf{S}_2$. The latter may typically be a transition metal ion with quenched orbital momentum. We found that the exchange processes that

contribute do not change the spin projection on the Dy^{3+} ion ($\Delta M_{S_1} = 0$, quantization axis $\hat{\mathbf{z}}_1$), and that this result is independent of the exchange partner. It is also known that every exchange process commutes with the total spin (the matrix elements involved are spin-independent matrix elements of kinetic, potential, and Coulomb energy [14]), so that $\Delta M_{S_1} + \Delta M_{S_2} = 0$. It follows then that $\Delta M_{S_2} = 0$, or, the exchange Hamiltonian commutes with the z_1 component of $\mathbf{S}_2$. The simplest expression compatible with this requirement is

$$- J s_{z_1} S_{z_1}, \tag{4.2.14}$$

where s naturally represents Dy^{3+} and S represents $\mathbf{S}_2$. The interaction is of Ising form with the anisotropy axis of Dy^{3+} as Ising axis. Note that, when $S_2 > 1/2$, higher powers of S_{z_1} may enter the Hamiltonian. Considering exchange interaction as a perturbation however, one can usually assume that the lowest order contribution, Eq. (4.2.14), is the leading term.

There are other cases conceivable, for example dipole-dipole interaction between the moment of Dy^{3+} and a neighboring moment. One will always find, as above, that the Hamiltonian is a product of s_z (belonging to Dy^{3+}) and a part that belongs to the other ion and whose form depends on the kind of the other ion and on the details of the interaction.

We have now obtained that a Dy^{3+} ion, if its ground state is $|M_J = \pm 15/2\rangle$, fairly well separated from excited states, interacts with the magnetic field and with neighboring ions as an Ising spin-1/2, in the sense that the interaction is always proportional to s_z, as expressed in the Eqs. (4.2.10), (4.2.13) and (4.2.14). This means that a chain-like molecular structure having Dy^{3+} ions of this kind at regular positions in the chain would meet the requirements of a decorated Ising chain, given in part by Eqs. (4.2.1) and (4.2.2). It remains of course to be shown that $|M_J = \pm 15/2\rangle$ can indeed be the ground state of a coordinated Dy^{3+} ion in a polynuclear complex.

At first sight, this seems rather unlikely. $|M_J = \pm 15/2\rangle$ is an eigenstate of cylindrical symmetry. Within lanthanide f^n states, the crystal field is effectively cylindrical if there is, at least, a fourfold rotation-inversion axis (S_4) or an eightfold rotation axis (C_8) [15]. S_4 symmetry has been obtained, for example, in mononuclear bis(phtalocyaninato) sandwich complexes of the lanthanides [16]. Even when such high symmetry is attained, the ground state is not necessarily the cylindrical doublet with highest $|M_J|$ value [16]. Apart from that, the symmetry of the coordination sphere of a lanthanide ion in a polynuclear, possibly heterometallic, complex or chain is usually much lower or even completely absent. Such is the case for the two examples considered in this paper. On the basis of symmetry alone, there is thus no reason to expect $|M_J = \pm 15/2\rangle$ to be an eigenstate, let alone the ground state. Nevertheless, recent *ab initio* calculations have revealed the unexpected result that the

ground state of several low-symmetry complexes of Dy^{3+} is very close to $|M_J = \pm 15/2\rangle$ [2,3,17–19]. They used the multiconfigurational, wavefunction-based CASSCF/RASSI-SO method, to obtain accurate wavefunctions for several of the lowest Kramers doublets. Calculation of the principal g factors of these states gives an indication of their composition. It was found in several cases that the ground doublet has g_z close to, but lower than 20, and g_x and g_y close to 0 [2,3,17,18]. This corresponds to a doublet mainly composed of $|M_J = \pm 15/2\rangle$.

With evidence of *ab ibitio* calculations it is thus possible to identify Dy^{3+} in certain coordination environments as an Ising spin-1/2 (to a good approximation). We will use this information to identify the compounds in Sections 4.3 and 4.4 as decorated Ising chains (or rings).

To conclude this section we remark that one cannot deduce from the vanishing of two g factors alone that a Kramers doublet will behave as an Ising spin. It will, of course, in its interaction with the magnetic field (Eq. (4.2.10)), but this will not, in general, be true for the exchange interaction. Take again the example of Dy^{3+}, supposing the ground state is the Kramers doublet $|M_J = \pm 7/2\rangle$. It is perfectly uniaxial because $g_x = g_y = 0$ and $g_z = 9\frac{1}{3}$. A closer look at the expansion of $|M_J = \pm 7/2\rangle$ in terms of the Russel-Saunders states $|M_L\rangle|M_S\rangle$ shows, however, that the selection rules in Eq. (4.2.12) permit a matrix element to exist between $|+7/2\rangle$ and $|-7/2\rangle$, therefore introducing non-Ising terms (i.e. s_x and s_y) in the same order of perturbation theory as the Ising term in the exchange Hamiltonian.

4.2.3 Nature of the eigenstates and level crossings

There exists a similarity between the spectra of the decorated and undecorated Ising chains at which we want to take a closer look here. We suppose infinite, periodic chains, or periodic, even-membered rings (In odd-membered rings spin-frustration complicates the picture). We also limit ourselves to chains with Ising spins of 1/2.

The undecorated, or simple, Ising chain in a magnetic field B parallel with the z axis is given by Eq. (4.2.1) and

$$\hat{h}_i = -J s_i s_{i+1} - \mu_B g s_i B, \tag{4.2.15}$$

where s_i is the z component of $\mathbf{s}_i$ ($s_i = \pm 1/2$). We assume, without loss of generality, $B \geq 0$. The eigenstates of the chain are spin *configurations* like $(\uparrow\uparrow\downarrow\uparrow\downarrow \ldots)$ etc. Of the 2^n eigenstates only two distinct ones can be the ground state: the ferromagnetic (F) and the antiferromagnetic (AF):

$$\begin{aligned} \mathrm{F} &: (\uparrow\uparrow\uparrow\uparrow \ldots) \quad \text{if} \quad J > 0, \\ \mathrm{AF} &: (\uparrow\downarrow\uparrow\downarrow \ldots) \quad \text{if} \quad J < 0 \quad \text{and} \quad \mu_B g B < |J|. \end{aligned} \tag{4.2.16}$$

When $B = 0$ time-reversal symmetry makes every state degenerate with the state formed by flipping all the spins. This degeneracy is meant to be implied in (4.2.16), where only one of two states is shown in each case. Only the two AF states remain degenerate when $B \neq 0$. When $J < 0$ a ground state level crossing occurs from AF to F when B is increased. At the point of crossing ($\mu_{\mathrm{B}} g B = |J|$), every state that has not less spins up than spins down (i.e. $M = \sum_i s_i \geq 0$) has the same energy. These include AF ($M = 0$) and F ($M = n/2$), but also an infinite number of intermediate-M states, which however can never be the ground state at any other value of B. Thus the ground state of the Ising chain is either F or AF, and they are degenerate, together with an infinite number of other states, at the crossing point.

We now decorate the Ising bonds with identical but arbitrary units to obtain a periodic decorated Ising chain. The spectrum is given by Eq. (4.2.3). Since the chain is periodic, the spectrum of the individual units $\hat{h}_i$ is independent of i and the energies may be written as ε_k, with k ranging over the eigenstates of $\hat{h}_i$. There are four sets of ε_k: $\varepsilon_k(\uparrow\uparrow)$, $\varepsilon_k(\uparrow\downarrow)$, $\varepsilon_k(\downarrow\uparrow)$ and $\varepsilon_k(\downarrow\downarrow)$, in an obvious notation. Notice that the eigenstates of this chain can still be classified according to the configuration of the *Ising* spins: $(\uparrow\uparrow\downarrow\uparrow\downarrow\dots)$ etc., which follows from the fact that all the s_i and $\hat{H}$ form a commuting set of observables. Per Ising configuration there are of course many eigenstates, determined by the choice of ε_k on every unit cell. Two states belonging to different Ising configurations can never interact.

An interesting question is whether the same rules hold for the ground state of the decorated Ising chain as did for the simple Ising chain. The answer is yes; the ground state is either F or AF (reffering to the Ising spin configuration) and a crossing between them is possible, with the same number and kind of degenerate states as in the simple Ising chain. To show this, we have to consider only the lowest eigenstate belonging to each of the 2^n possible Ising spin configurations. In these states every unit is in its lowest possible state for the given orientation of the neighboring Ising spins: $\varepsilon_1(s, s')$ (we assume this energy to be nondegenerate), so that the total energy of the chain state is

$$E = n_{\uparrow\uparrow}\varepsilon_1(\uparrow\uparrow) + n_{\downarrow\downarrow}\varepsilon_1(\downarrow\downarrow) + n_{\downarrow\uparrow}\varepsilon_1(\downarrow\uparrow) + n_{\uparrow\downarrow}\varepsilon_1(\uparrow\downarrow), \tag{4.2.17}$$

where $n_{\uparrow\uparrow}$ denotes the number of pairs of neighboring Ising spins that are both spin up, etc. For example, in the F configuration in Eq. (4.2.16), $n_{\uparrow\uparrow} = n$ (periodic boundary conditions are assumed), while in the AF configuration, $n_{\uparrow\uparrow} = 0$. The eigenstates we have just described, with energy (4.2.17), are in an obvious one-to-one correspondence with the eigenstates of the simple Ising chain. The ground state is found by minimizing (4.2.17) with respect to the $n_{ss'}$, under the restrictions

$$\begin{aligned} n_{\uparrow\uparrow} + n_{\downarrow\downarrow} + n_{\downarrow\uparrow} + n_{\uparrow\downarrow} &= n \\ n_{\downarrow\uparrow} &= n_{\uparrow\downarrow}. \end{aligned} \tag{4.2.18}$$

The first relation states that the total number of Ising spins (or, equivalently, unit cells) is n. The second relation follows from the fact that, in a cyclic spin configuration, every $\downarrow\uparrow$ pair must eventually be followed by a $\uparrow\downarrow$ pair, possibly after a number of $\uparrow\uparrow$ pairs. Another restriction is that whenever $n_{\uparrow\uparrow}$ and $n_{\downarrow\downarrow}$ are both not zero, $n_{\downarrow\uparrow}$ (and by Eq. (4.2.18) also $n_{\uparrow\downarrow}$) must be at least one. Using (4.2.18) we can rewrite Eq. (4.2.17) as

$$\begin{aligned} E = {} & n_{\uparrow\uparrow}\Big(\varepsilon_1(\uparrow\uparrow) - \frac{1}{2}[\varepsilon_1(\uparrow\downarrow) + \varepsilon_1(\downarrow\uparrow)]\Big) \\ & + n_{\downarrow\downarrow}\Big(\varepsilon_1(\downarrow\downarrow) - \frac{1}{2}[\varepsilon_1(\uparrow\downarrow) + \varepsilon_1(\downarrow\uparrow)]\Big) \\ & + \frac{n}{2}[\varepsilon_1(\uparrow\downarrow) + \varepsilon_1(\downarrow\uparrow)], \end{aligned} \tag{4.2.19}$$

where we see that only the average $[\varepsilon_1(\uparrow\downarrow) + \varepsilon_1(\downarrow\uparrow)]/2$ of the "antiparallel" energies enters the equation. The last term is a constant and can be discarded for the purpose of relative energy considerations.

We can now derive the values of $n_{\uparrow\uparrow}$ and $n_{\downarrow\downarrow}$ for the ground state of the chain, keeping in mind that $\varepsilon_1(s, s')$ is a function of the magnetic field $\mathbf{B}$. Suppose then, first, that $\mathbf{B} = 0$. Time reversal symmetry asserts that $\varepsilon_1(\uparrow\uparrow) = \varepsilon_1(\downarrow\downarrow)$ and $\varepsilon_1(\uparrow\downarrow) = \varepsilon_1(\downarrow\uparrow)$. It is simple to see that, depending on the relative ordering of $\varepsilon_1(\uparrow\uparrow)$ and $\varepsilon_1(\uparrow\downarrow)$, E is minimal in the F configuration ($n_{\uparrow\uparrow} = n$ or $n_{\downarrow\downarrow} = n$; $n_{\uparrow\downarrow} = n_{\downarrow\uparrow} = 0$) when $\varepsilon_1(\uparrow\uparrow) < \varepsilon_1(\uparrow\downarrow)$ or in the AF configuration ($n_{\uparrow\uparrow} = n_{\downarrow\downarrow} = 0$; $n_{\uparrow\downarrow} = n_{\downarrow\uparrow} = n/2$) when $\varepsilon_1(\uparrow\uparrow) > \varepsilon_1(\uparrow\downarrow)$ (we exclude the possibility of equality of both energies from the discussion; $\varepsilon_1(\uparrow\uparrow) = \varepsilon_1(\uparrow\downarrow)$ would correspond, in the simple Ising chain (4.2.15), with $J = 0$). When $\mathbf{B} \neq 0$, time reversal symmetry is not operative, and we have, in general, four different energies $\varepsilon_1(s, s')$. The equation (4.2.19) shows that the configuration that minimizes E is determined by the sign of the two terms in round brackets; if both are positive, then $n_{\uparrow\uparrow} = n_{\downarrow\downarrow} = 0$ (AF configuration); if at least one of them is negative, then either $n_{\uparrow\uparrow} = n$ or $n_{\downarrow\downarrow} = n$ (F configuration), depending on whether respectively $\varepsilon_1(\uparrow\uparrow)$ or $\varepsilon_1(\downarrow\downarrow)$ is lower.

Finally, the magnetic field can induce a transition from the AF to a F ground state configuration, say with all Ising spins up. This happens when

$$\varepsilon_1(\uparrow\uparrow) = \frac{1}{2}[\varepsilon_1(\uparrow\downarrow) + \varepsilon_1(\downarrow\uparrow)], \tag{4.2.20}$$

and $\varepsilon_1(\uparrow\uparrow) < \varepsilon_1(\downarrow\downarrow)$. At this point, the ground state configurations are all the solutions $\{n_{\downarrow\downarrow} = 0, 0 \leq n_{\uparrow\uparrow} \leq n\}$, exactly the same as in the simple Ising chain.

We find thus a complete analogy between the simple and the decorated Ising chain as far as the ground state Ising spin configuration is concerned. The only possible configurations are the fully antiferromagnetically aligned and the fully ferromagnetically aligned configurations. No "intermediate" configuration can

be the ground state. The only exception is the crossing point between AF and F, where there is a high degeneracy of configurations. These conclusions are independent of the nature of the decorating unit.

Although the decorated Ising model predicts that the AF and F ground states are both doubly degenerate (in zero field), this degeneracy is not a result of the spatial symmetry: in the cyclic group C_n, the two AF components combine into irreducible representations (irrep) A and B, while the two F components transform as two A irreps. Introduction of neglected terms in the Hamiltonian, that destroy the Ising property, could split these ground state components.

The decorated Ising chain affords a second kind of level crossing, not present in the simple Ising chain. It arises from the crossing of levels *within* a decorating unit. A ground state crossing can result in which the Ising spin configuration remains the same but the state corresponding to $\varepsilon_1(s, s')$ crosses with the state corresponding to $\varepsilon_2(s, s')$. More precisely this happens in the F configuration when $\varepsilon_1(\uparrow\uparrow) = \varepsilon_2(\uparrow\uparrow)$ and in the AF configuration when $\frac{1}{2}[\varepsilon_1(\uparrow\downarrow) + \varepsilon_1(\downarrow\uparrow)] = \frac{1}{2}[\varepsilon_2(\uparrow\downarrow) + \varepsilon_2(\downarrow\uparrow)]$. The previous paragraphs have shown that we do not need to consider other configurations for the ground state. Again a high degeneracy (2^n) accompanies the level crossing.

Level crossings are usually connected with the presence of good quantum numbers. For the Ising-type crossings, the relevant conserved quantities are the n Ising spins $\{s_i\}$. The crossing of energy levels within the decorating unit should be associated with a conserved variable that is *internal* to that unit, much the same as in isolated molecules. In Section 4.3 we will encounter an example where both transitions—Ising type and internal type—occur in a magnetic field.

4.2.4 Magnetization and susceptibility of powder samples

The magnetization M and magnetic susceptibility χ of one molecule or a collection of identically oriented molecules follow directly from the free energy f. Let $\mathbf{B}$ be the magnetic field and μ and ν represent Cartesian components x, y, z, then [20]

$$M_\mu = -\frac{\partial f}{\partial B_\mu}$$
$$\chi_{\mu\nu} = -\left.\frac{\partial^2 f}{\partial B_\mu \partial B_\nu}\right|_{B\to 0},$$

apart from a constant factor depending on the desired system of units.

In the next sections we will be comparing our theoretical results with measurements performed on powder samples of the crystalline compounds. We need

to know how the previous two equations have to be adapted to this situation. A powder consists of a large number of microscopic crystals, assumed to be oriented randomly with respect to any chosen reference frame. It follows that one has to average out over all directions. For χ this gives the simple result [21]

$$\chi_p = (\chi_{xx} + \chi_{yy} + \chi_{zz})/3. \tag{4.2.21}$$

For M, on the other hand, an integration is necessary. Applying a magnetic field to a powder is equivalent to applying the field to one molecule over all directions and averaging out the result. The quantity to be averaged is the component of the magnetization along the axis of the applied field, because, in the rotationally symmetric powder–field system, only this component does not cancel out [21]. Let θ and ϕ be the polar angles of the magnetic field vector with respect to a molecular reference frame, then the free energy is a function of θ, ϕ, and the strength of the field, B: $f(\theta, \phi, B)$. The projection of the magnetization on the field direction $\hat{\mathbf{e}}_B$ is

$$\hat{\mathbf{e}}_B \cdot \mathbf{M}(\theta, \phi, B) = -\frac{\partial f(\theta, \phi, B)}{\partial B}. \tag{4.2.22}$$

Averaging Eq. (4.2.22) over one hemisphere gives the powder magnetization

$$M_p(B) = \frac{1}{2\pi} \int_0^{2\pi} \int_0^{\pi/2} -\frac{\partial f(\theta, \phi, B)}{\partial B} \sin\theta \, d\theta \, d\phi. \tag{4.2.23}$$

Let us see how the powder averaging affects the magnetization curve for a simple Ising chain. Take a spin-1/2 infinite antiferromagnetic Ising chain with anisotropy axes parallel with each other and with the z axis, and uniaxial g-factors ($g_x = g_y = 0$ and $g_z \equiv g$). This could for example be realized by a chain of identical Dy^{3+} units (see Section 4.2.2). The Hamiltonian is given by Eq. (4.2.1), substituting

$$\hat{h}_i = -J s_i s_{i+1} - \mu_B g s_i B \cos\theta, \tag{4.2.24}$$

where $B\cos\theta$ is the z component of the magnetic field, and $J < 0$. Defining $j \equiv J/k$ and $b \equiv \mu_B g B/k$, the magnetization, which has only a nonzero z component, is [12]

$$M_z = \frac{\mu_B g}{2} \frac{\sinh[b\cos\theta/2T]}{\sqrt{\sinh^2[b\cos\theta/2T] + e^{-j/T}}}.$$

The projection on the field direction (Eq. (4.2.22)) is $M_z \cos\theta$. Plugging this in Eq. (4.2.23) and substituting $u = \cos\theta$ yields the powder magnetization of the Ising chain

$$M_p = \frac{\mu_B g}{2} \int_0^1 \frac{\sinh[bu/2T]}{\sqrt{\sinh^2[bu/2T] + e^{-j/T}}} u \, du. \tag{4.2.25}$$

Because the Hamiltonian in Eq. (4.2.24) does not depend on ϕ, this variable has been integrated out in Eq. (4.2.25).

Figs. 4.3 and 4.4 show plots of M_z and M_p versus magnetic field, for coupling constant $j = -1\,\mathrm{K}$. The steplike appearance of M_z is associated with the ground state crossing that occurs at $b\cos\theta = |j|$. At that point, the antiferromagnetic ground state (or rather ground state Ising doublet) is replaced by the ferromagnetic state (all spins up). Consequently, the magnetization jumps from zero to the saturation value of 0.5, as seen in Fig. 4.3. The magnetization of a powder sample of the same Ising chain is shown in Fig. 4.4. Before the crossing point, M_p behaves qualitatively the same as M_z. After the crossing point however, M_p is seen to reach only slowly its saturation value, which is half of the saturation value of M_z, viz. 0.25. The limiting curve of M_p as $T \to 0\,\mathrm{K}$ can be calculated exactly from Eq. (4.2.25):

$$M_p\Big|_{T\to 0} = \begin{cases} 0 & \text{if } b \le |j| \\ \dfrac{\mu_\mathrm{B} g}{4}\left(1 - \dfrac{|j|^2}{b^2}\right) & \text{if } b > |j|. \end{cases} \tag{4.2.26}$$

(This is of course only valid for the antiferromagnetic case $j < 0$.) In Fig. (4.4), this limiting curve is very closely approximated by the curve at $T = 0.01\,\mathrm{K}$. Clearly, the sharp step of M_z transforms in the powder to the concave form diplayed by M_p. This is understood from the fact that, in a powder, for a given field $b > |j|$, there is always a fraction of molecules that is not magnetized (in the sense that they are in the antiferromagnetic ground state) because they are oriented so with respect to the field, that $b\cos\theta < |j|$ (see Fig. 4.3). The powder saturates only when every molecule is fully magnetized, and this happens only for $b \to \infty$. Therefore, M_p (at $0\,\mathrm{K}$) does not abruptly saturate at the crossover point, but increases slowly to saturation.

4.2.5 Corrections for excited Kramers doublets

In deriving the exchange Hamiltonian in Section 4.2.2 we assumed that only the lowest Kramers doublet on Dy^{3+} took part. This is certainly a good approximation when the gap between the lowest and the second-lowest Kramers doublet is much larger then the strength of the exchange interaction. However, the excited Kramers doublets often have to be taken into account to a certain degree of approximation if a comparison with experimental data on susceptibility and magnetization is desired. The crystal field splitting of the ${}^6\mathrm{H}_{15/2}$ level is of the order of kT at room temperature. This gives rise to two effects: (i) a thermal population of excited Kramers doublets, and (ii) a modification of the lowest Kramers doublet as a function of the applied magnetic field by interaction with the excited doublets.

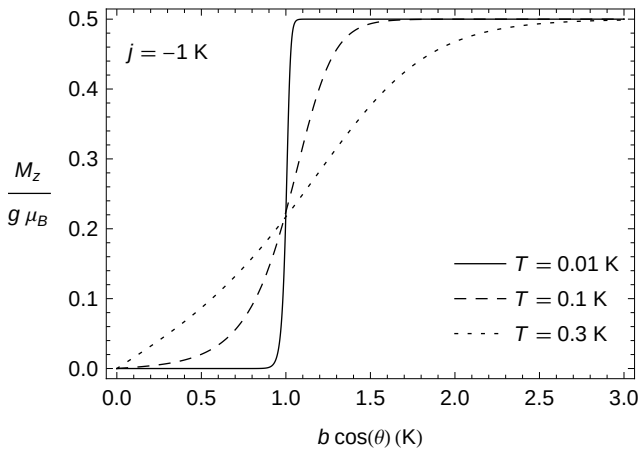

Figure 4.3: Magnetization versus field for the antiferromagnetic Ising chain, defined in Eq. (4.2.24). The curve approaches a perfect step as $T \to 0\,\mathrm{K}$.

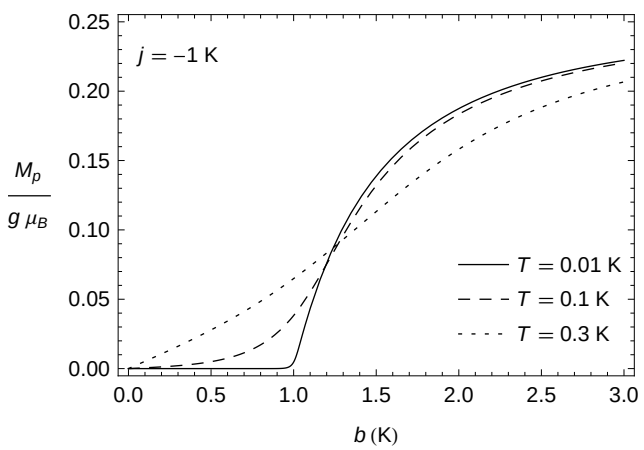

Figure 4.4: Magnetization of a powder sample of antiferromagnetic Ising chains. Compare with Fig. 4.3. The low temperature limiting curve is given in Eq. (4.2.26).

Effect (i) is mainly visible in the temperature dependence of χT: for a single Dy^{3+} center, χT increases monotonically with increasing temperature, from the value of the ground doublet at 0 K to the saturation value of ${}^6H_{15/2}$ at higher temperatures. Effect (ii) gives rise to temperature-independent paramagnetism (TIP). It is visible at temperatures sufficiently low so that only the ground doublet is occupied. It gives a linear increase of χT with T and a linear increase of the magnetization M with the applied field B.

In the simplest approximation, the contribution of the excited Kramers doublets to the magnetic properties of the chain is equal to the contribution they have to the properties of the single, isolated Dy^{3+} ion in the same ligand environment it has in the chain. Let χ_{DIC} and M_{DIC} denote susceptibility and magnetization derived from the decorated Ising chain model, and let χ_{Dy} denote the susceptibility of the Dy^{3+} center and $\mu'_{Dy}B$ the magnetic moment induced by B in the ground doublet of the Dy^{3+} center, then the corrected properties are (supposing one Dy^{3+} ion per unit cell)

$$\chi T = \chi_{DIC} T + \Big(\chi_{Dy} T - \chi_{Dy} T\big|_{T=0}\Big), \tag{4.2.27a}$$

$$\chi = \chi_{DIC} + \frac{1}{T}\Big(\chi_{Dy} T - \chi_{Dy} T\big|_{T=0}\Big), \tag{4.2.27b}$$

$$M = M_{DIC} + \mu'_{Dy} B. \tag{4.2.27c}$$

The last equation assumes that only the ground doublet of Dy^{3+} is occupied. This is correct at the temperature at which magnetization curves are usually recorded (e.g. 2 K). If necessary, corrections due to other magnetic ions can be added in the same way. χ_{Dy} and μ'_{Dy} can be obtained from multiconfigurational *ab initio* calculations [2, 3, 17, 18], or, in oligonuclear complexes, experimentally by replacing certain magnetic ions with diamagnetic ions [22].

The equations (4.2.27) are evidently correct in the limit of vanishing exchange interactions. The assumption we make is that the exchange interactions are sufficiently small for these corrections to remain valid. A more accurate approach should take into consideration the fact that the excited Kramers doublets also participate in the exchange interaction with neighbors. This is however out of the scope of the decorated Ising model.

4.3 [DyCuMoCu]$_\infty$ chain

We now turn our attention to two actual examples of decorated Ising models based on Dy^{3+}: a chain, treated in this section, and a four-ring treated in the following section. The problem is approached as follows: the Hamiltonian for the chain in a magnetic field is formulated, with the help of the considerations

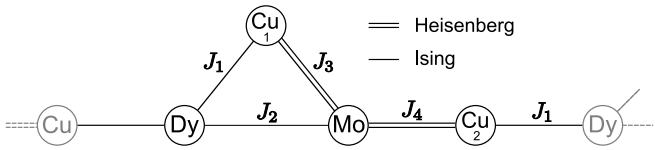

Figure 4.5: Scheme of one unit cell (black) of the $[\mathrm{DyCuMoCu}]_\infty$ chain, showing type of exchange interactions and labeling of exchange constants. See Ref. [2] for the complete molecular structure.

in Section 4.2.2. Values of the g factors of the magnetic ions are taken directly from *ab initio* calculations, reported elsewhere [2, 3]. This leaves the exchange coupling constants as parameters of the model, to be fitted by comparison with experimental magnetization and susceptibility data. (In Section 4.4, the direction of the anisotropy axis contributes one extra parameter.)

The [DyCuMoCu] chain was recently synthesized and details of its chemical composition and structure are given in Ref. [2].[6] The crystal structure was found to consist of parallel linear chains each made of [DyCuMoCu] unit cells. Fig. 4.5 shows how the metal ions are connected by ligand bridges. Multiconfigurational CASSCF/RASSI-SO calculations have been performed on each of the four metal ions in their ligand environment, suitably disconnected from the rest of the chain (details of the calculations can be found in Ref. [2] and the accompanying Supplementary Information). Most important for us is that the Dy^{3+} center was found to have a ground Kramers doublet, separated by 141 cm^{-1} from the second doublet, and characterized by complete uniaxial anisotropy:

$$\mathrm{Dy}^{3+}: \qquad g_z = 19.6, \quad g_x = 0, \quad g_y = 0. \tag{4.3.1}$$

(Actually g_x and g_y were calculated about 0.03, which can be ignored.) The value of $g_z = 19.6$ shows that this doublet is only slightly perturbed from the $|M_J = \pm 15/2\rangle$ doublet of the ${}^6\mathrm{H}_{15/2}$ level, the latter having $g_z = 20$. Together with the fact that the energy gap to the second Kramers doublet is about ten times larger than the exchange interaction (as we will find later), these results indicate that the Dy^{3+} ion will behave as an Ising spin, as described in Section 4.2.2. As a side-note we may add that the total splitting of the ${}^6\mathrm{H}_{15/2}$ level was calculated to be 560 cm^{-1}, which is indeed of the order of room-temperature kT (see Section 4.2.5).

Both Cu^{2+} (d^9) and Mo^{5+} (d^1) have a spin = 1/2, orbitally nondegenerate ground state, well separated ($> 15000\,cm^{-1}$) from higher states. The two Cu^{2+} ions in the unit cell reside in almost identical environments [2] and have therefore virtually the same properties. The calculated g factors are tetragonal:

[6] The molecular structure is pictured in Addendum B.

$g_\parallel = 2.33$, $g_\perp = 2.07$ for Cu^{2+} and $g_\parallel = 2.00$, $g_\perp = 1.95$ for Mo^{5+}. To avoid unnecessary complications we will regard these ions as isotropic spins with root-mean square g factors

$$\begin{aligned} Cu^{2+}: &\qquad g_{Cu} = 2.16, \\ Mo^{5+}: &\qquad g_{Mo} = 1.97. \end{aligned}$$

This approximation will not have important consequences for the magnetic properties, which are largely dominated by the high Dy^{3+} moment anyway.

We introduce exchange interaction between metal ions directly connected by ligand bridges. Dy^{3+} interacts with its three neighbors via the Ising Hamiltonian Eq. (4.2.14). Interaction between the isotropic spins is given by the Heisenberg Hamiltonian $-J_{ij}\mathbf{S}_i \cdot \mathbf{S}_j$. Fig. 4.5 shows the exchange configuration, with single bonds representing Ising interaction and double bonds representing Heisenberg interaction. Note that we have approximated the Dy-Cu_1 and Dy-Cu_2 coupling strengths to be equal (J_1), following the approximate local symmetry of the Dy-Cu pairs [2].

It is now possible to see that the chain is indeed a decorated Ising chain: The [CuMoCu] unit decorates each Dy-Dy bond and the Dy^{3+} Ising spins form nodes in the chain that separate the [CuMoCu] units from each other. The total Hamiltonian in a magnetic field $\mathbf{B}$ is then given by Eq. (4.2.1) and

$$\begin{aligned} \hat{h}_i(s_i^z, s_{i+1}^z) = &-J_1 s_i^z S_{i\mathrm{Cu}_1}^z - J_2 s_i^z S_{i\mathrm{Mo}}^z - J_3 \mathbf{S}_{i\mathrm{Cu}_1} \cdot \mathbf{S}_{i\mathrm{Mo}} - J_4 \mathbf{S}_{i\mathrm{Mo}} \cdot \mathbf{S}_{i\mathrm{Cu}_2} \\ &- J_1 S_{i\mathrm{Cu}_2}^z s_{i+1}^z - \mu_\mathrm{B} g_\mathrm{Dy} s_i^z B_z - \mu_\mathrm{B} (g_\mathrm{Cu} \mathbf{S}_{i\mathrm{Cu}_1} + g_\mathrm{Mo} \mathbf{S}_{i\mathrm{Mo}} + g_\mathrm{Cu} \mathbf{S}_{i\mathrm{Cu}_2}) \cdot \mathbf{B}, \end{aligned} \tag{4.3.2}$$

where s_i^z is shorthand for $s_{i\mathrm{Dy}}^z$ and g_Dy is the g_z factor of Dy^{3+} (Eq. (4.3.1)). The z axis is the anisotropy axis of the Dy^{3+} center. We have not specified its direction with respect to the chain axis but this is not important here because there are no other axes in the problem (the Dy^{3+} anisotropy axes are parallel by translational symmetry and we have assumed Cu^{2+} and Mo^{5+} isotropic). All the spins in Eq. (4.3.2) are spins of 1/2.

The Hamiltonian exhibits some symmetry. It is rotationally invariant around z, if $\mathbf{B}$ is rotated simultanuously. We may therefore restrict $\mathbf{B}$ to lie in a plane through z, say the xz plane. This simplifies calculation of the powder magnetization Eq. (4.2.23). When $\mathbf{B}$ is directed along the z axis, the z component of the total spin *in* each decorating unit is conserved:

$$S_i^z = S_{i\mathrm{Cu}_1}^z + S_{i\mathrm{Mo}}^z + S_{i\mathrm{Cu}_2}^z, \qquad [S_i^z, \hat{H}(\mathbf{B} \parallel \hat{\mathbf{z}})] = 0. \tag{4.3.3}$$

We also note that in this case the Zeeman Hamiltonian commutes *almost* with $\hat{H}$. It would commute exactly when $g_\mathrm{Cu} = g_\mathrm{Mo}$, for then the last term in Eq. (4.3.2) reduces to $-\mu_\mathrm{B} g_\mathrm{Cu} S_i^z B_z$.

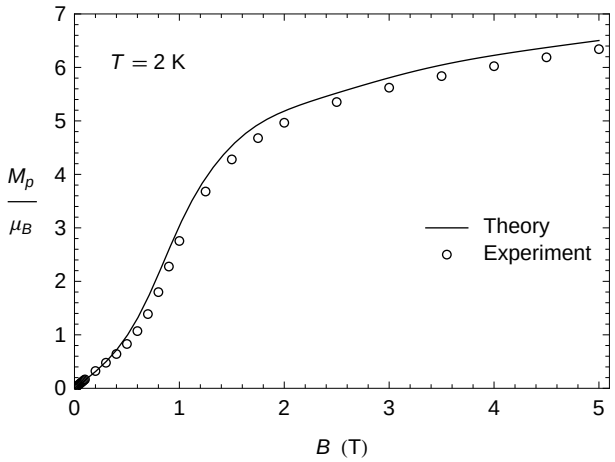

Figure 4.6: Powder magnetization of $[\mathrm{DyCuMoCu}]_\infty$.

We let the length of the chain go to infinity: $n \to \infty$. To solve for the thermodynamic properties we are only required to find the eigenvalues $\varepsilon_k(s, s')$ of Eq. (4.3.2) (See Section 4.2.1), with $k = 1 \ldots 8$, corresponding to the 2^3 possible states of the [CuMoCu] spin unit. This is done by 4 numerical 8×8 matrix diagonalizations, one for each (s, s') pair.

We can now compare the theory with experiment. Powder magetization (at 2 K) and susceptiblity data have been recorded [2]. We recall that we have to correct the theoretical curves before comparing with experiment according to Eq. (4.2.27). The corrections are provided by the *ab initio* calculations [2]. μ'_{Dy} turns out to be $0.03\,\mu_{\mathrm{B}}/\mathrm{T}$. The accompanying correction in Eq. (4.2.27c) is never more than 2.5% of M_p. We ignore this correction. We do however correct χ_p as in Eqs. (4.2.27a) and (4.2.27b).

Closest agreement with experiment was found for the following values of the exchange constants (plots in Figs. 4.6 and 4.7):

$$J_1 = 15.3\,\mathrm{cm}^{-1},\ J_2 = -8.0\,\mathrm{cm}^{-1},\ J_3 = -8.3\,\mathrm{cm}^{-1},\ J_4 = 11.8\,\mathrm{cm}^{-1}. \quad (4.3.4)$$

These were obtained by a least-squares fit of χ_p followed by a small manual adjustment to improve the fit of M_p while not distorting that of χ_p appreciably. (The least-squares fit of χ_p gave $J_1 = 15.7\,\mathrm{cm}^{-1}$, $J_2 = -8.3\,\mathrm{cm}^{-1}$, $J_3 = -6.3\,\mathrm{cm}^{-1}$, $J_4 = 11.8\,\mathrm{cm}^{-1}$.) There are, as far as we know, no data in the literature to directly compare the values in Eq. (4.3.4) with. However, an experimental study is available of a (Dy^{3+}, Cu^{2+}) dinuclear complex in which the bridging ligand is the same as in this chain [22]. The authors found a ferromagnetic interaction. A superficial analysis of the susceptibility curve

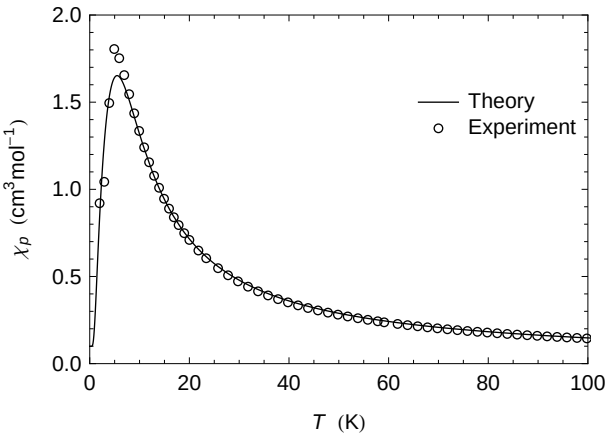

Figure 4.7: Powder magnetic susceptibility of [DyCuMoCu]$_\infty$. The theoretical curve contains the correction for excited Kramers doublets, Eq. (4.2.27b).

in that paper using the Ising Hamiltonian we use in this paper, yields $J_1 = 15 \pm 5\,\mathrm{cm}^{-1}$. The other values in (4.3.4) are difficult to assess. Some evidence from DFT calculations is given in [2]. Certainly, no confidence should be attached to the numbers in decimal places in (4.3.4).

The effect of the excited Kramers doublets of Dy^{3+} is most clearly seen in the $\chi_p T$ curve (Fig. 4.8). The curve shows a steady increase above 50 K which is not predicted by our decorated Ising model, but is indeed due to the thermal population of the Kramers doublets that originate from the $^6\mathrm{H}_{15/2}$ level. We can obtain the expected high-temperature limit of $\chi_p T$ by considering the metal ions as independent spins. χ_p is given by Eq. (4.2.21). The susceptibility components $\chi_{\alpha\alpha}$ of an angular momentum multiplet J with principal g-factors g_α ($\alpha = x, y, z$) are given by [23]

$$\chi_{\alpha\alpha} = \frac{N_A \mu_\mathrm{B}^2}{3kT} g_\alpha^2 J(J+1). \tag{4.3.5}$$

Summing over Dy^{3+} ($^6\mathrm{H}_{15/2}$, $g_{15/2} = 4/3$), Cu_1, Mo, and Cu_2 (all are isotropic) gives

$$\chi_p T = \frac{N_A \mu_\mathrm{B}^2}{3k} \left(g_{15/2}^2 \frac{15}{2}\frac{17}{2} + (g_{\mathrm{Cu}}^2 + g_{\mathrm{Mo}}^2 + g_{\mathrm{Cu}}^2)\frac{1}{2}\frac{3}{2} \right) = 15.4 \frac{\mathrm{cm}^3\,\mathrm{K}}{\mathrm{mol}}.$$

A similar calculation, only including the lowest Kramers doublet of Dy^{3+}, with g-factors as in Eq. (4.3.1), gives $13.2\,\mathrm{cm}^3\,\mathrm{K\,mol}^{-1}$. The correction supplied by the *ab initio* calculations to account for this difference, is seen to nicely cover the high-temperature part of the experimental curve.

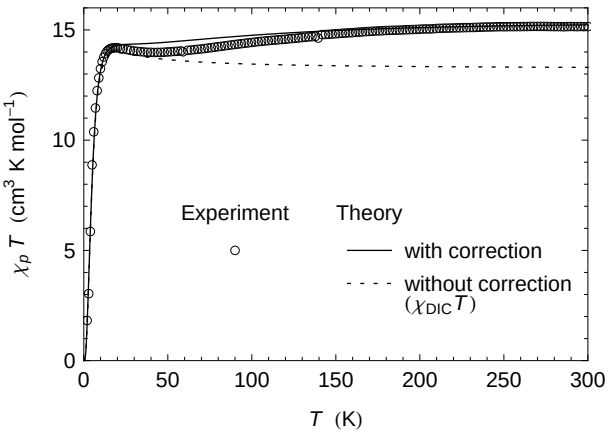

Figure 4.8: Powder magnetic susceptibility of $[\mathrm{DyCuMoCu}]_\infty$. The necessity of the correction for excited Kramers doublets, Eq. (4.2.27a), is shown.

One notices that $\chi_p T$ shows a slight depression around 40 K which is not entirely reproduced by the theory. This might indicate a failure of the simple approximation we used to include the excited Kramers doublets. Eq. (4.2.27a) is certainly correct at very high temperatures, when the exchange interactions are irrelevant, and at very low temperatures, when the excited Kramers doublets are not occupied. If these two regions do not overlap, however, there is a temperature window between, in which excited doublets start to get occupied while exchange interaction is not quite negligible yet. In that case, the exchange interaction of the occupied excited doublet(s) with other ions should be taken into account. Such an interaction of antiferromagnetic type could possibly depress $\chi_p T$ as observed.

We shall now describe some features of the spectrum of the chain, paying attention to the properties described in Section 4.2.3. Consider the chain without magnetic field. The exchange parameters in Eq. (4.3.4) predict a ground state that has an AF Ising spin configuration. This is in accordance with the susceptiblility measurements, which show that $\chi T \to 0$ as $T \to 0$, requiring a nonmagnetic ground state (Fig. 4.8). The ground state is indeed nonmagnetic because $|\varepsilon_1(\uparrow\downarrow)\rangle$ is the time-reversed state of $|\varepsilon_1(\downarrow\uparrow)\rangle$. Let M_S denote an eigenvalue of S^z (Eq. (4.3.3)): $M_S \in \{-3/2, -1/2, 1/2, 3/2\}$. S_i^z is conserved so M_S may be used to label the eigenstates $|\varepsilon_k(s, s')\rangle$ (we may leave out the index i because all units of the chain are identical). For the ground state, we find $M_S = -1/2$ in $|\varepsilon_1(\uparrow\downarrow)\rangle$ and $M_S = 1/2$ in $|\varepsilon_1(\downarrow\uparrow)\rangle$.

Since the ground state is AF, we might expect that in a magnetic field a crossover will occur to a F ground state. This is indeed what happens. The

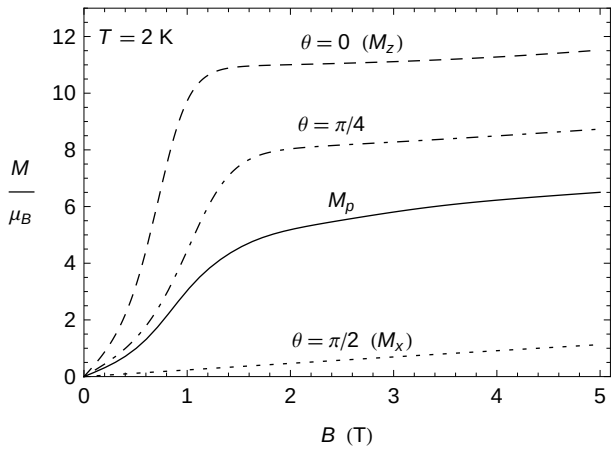

Figure 4.9: Theoretical magnetization of [DyCuMoCu]$_\infty$. The powder magnetization M_p (See also Fig. 4.6) is compared with Cartesian components of magnetization at three directions of the applied field. θ is the angle between $\mathbf{B}$ and the z axis. The components shown are the projections of $\mathbf{M}$ on the field direction, as in Eq. (4.2.22). M_p is the average of this component over all directions θ.

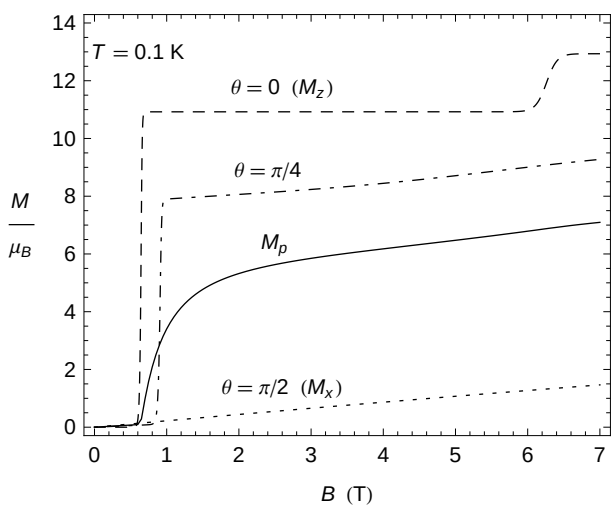

Figure 4.10: Theoretical magnetization of [DyCuMoCu]$_\infty$. Same as Fig. 4.9 but at lower temperature and to higher field.

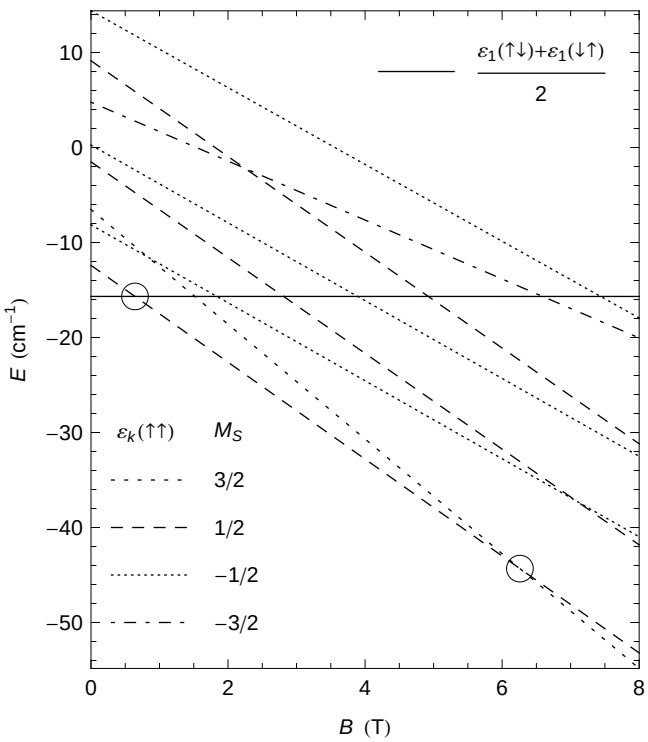

Figure 4.11: Eigenvalues of $\hat{h}(s, s')$ (Eq. (4.3.2)) in a magnetic field *parallel* with the z axis ($\theta = 0$). Circles indicate ground state level crossings. The ground state of the chain is AF in zero field (left), switches to F at 0.64 T and undergoes an internal level crossing at 6.3 T, marked by a change of the internal quantum number M_S from 1/2 to 3/2. Both crossings can be seen in the $\theta = 0$ magnetization curve in Fig. 4.10. Note that the energy curves appear as straight lines, although, with the exception of $M_S = \pm 3/2$, they are not exactly so, because the Zeeman Hamiltonian does not *completely* commute with the total Hamiltonian.

convex increase of M_p in Fig. 4.6 points to a flip of the Dy^{3+} spins to a parallel configuration. This is inferred from the value of the magnetization, which approaches $6\,\mu_B$ at 5 T. The [CuMoCu] unit alone can only contribute a maximum of $(2.16 + 1.97 + 2.16)/2 = 3.15\,\mu_B$. The strong increase must come from the contribution of the large Dy^{3+} moments.

The behavior of magnetization along certain directions of applied field is shown in Fig. 4.9. The AF $\rightarrow$ F transition is most clearly seen when the field is applied along z ($\theta = 0$); the transition occurs below 1 T. After 1 T, M_z reaches an approximately constant plateau at $\approx 11\,\mu_B$. The saturation value of magnetization in direction $0 \leq \theta \leq \pi/2$ is $(19.6\cos\theta + 2.16 + 1.97 + 2.16)/2$. This gives $12.9\,\mu_B$ for $\theta = 0$, which shows that M_z has not quite reached its maximum at 5 T.

The positions of level crossings become more sharply defined on lowering the temperature (Fig. 4.10). Here we also see that M_z undergoes a second transition at 6.3 T, after wich it reaches saturation. This transition is connected with a level crossing *in* the [CuMoCu] unit (see Section 4.2.3) from $M_S = 1/2$ to $M_S = 3/2$, as opposed to the first transition, at 0.64 T, which is of the Ising type, described by Eq. (4.2.20). The latter is the analogue of the transition in the AF simple Ising chain (Fig. 4.3), while the "internal" transition has no such analogue but is unique to the decorated Ising chain. The relevant energy level diagram is shown in Fig. 4.11. Note that, for fields not parallel to z (for example, $\theta = \pi/4$ in Fig. 4.10, M_S is not a quantum number and the internal level crossing turns into an avoided crossing. This does not apply for the Ising level crossing because the Ising spins are always conserved. Only when the field is applied perpendicular to z ($\theta = \pi/2$ in Fig. 4.10) does the AF $\rightarrow$ F transition not occur because the Dy^{3+} spins do not interact with perpendicular fields.

The low-temperature limit of the powder magnetization in Fig. 4.10 may be compared with that of the simple Ising chain in Fig. 4.4. The resemblence is clear; the decorated chain is different in the small linear increase of M_p before the transition, and the more linear approach to saturation, which lies at $(19.6/2 + 2.16 + 1.97 + 2.16)/2 = 8.0\,\mu_B$. Both are due to TIP interaction in the [CuMoCu] unit, the effect of which is most clearly seen in the M_x curve in Fig. 4.10.

To conclude this section we remark that the mentioned similarity with the magnetization of the simple Ising chain is a consequence of the very high magnetic moment of the Dy^{3+} spins in comparison with the [CuMoCu] unit. The dominance of Dy^{3+} is most dramatically shown in the components of χT (Fig. 4.12). An application of Eq. (4.3.5) shows that the high-temperature limit of $\chi_{xx}T$ is $\frac{N_A\mu_B^2}{3k}(2.16^2 + 1.97^2 + 2.16^2)\frac{1}{2}\frac{3}{2} = 1.24\,\mathrm{cm^3\,K\,mol^{-1}}$, while that of $\chi_{zz}T$ is $\frac{N_A\mu_B^2}{3k}(19.6^2 + 2.16^2 + 1.97^2 + 2.16^2)\frac{1}{2}\frac{3}{2} = 37.2\,\mathrm{cm^3\,K\,mol^{-1}}$.

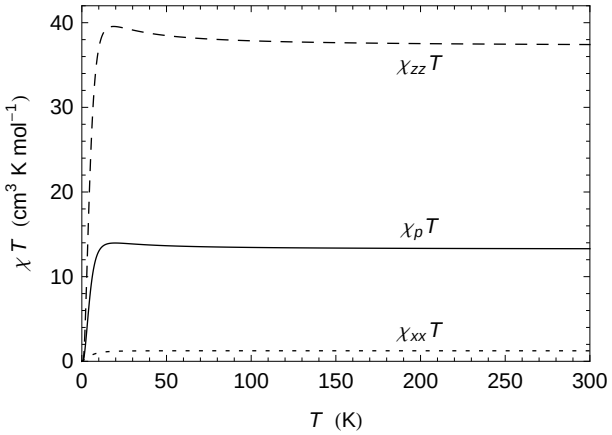

Figure 4.12: Theoretical susceptibility of $[\mathrm{DyCuMoCu}]_\infty$, without correction for excited Kramers doublets. The powder $\chi_p T$ (see also Fig. 4.8) is compared with the Cartesian components of χT. z is the direction of the anisotropy axis of Dy^{3+}, x is any direction perpendicular to z. $\chi_p = (\chi_{zz} + 2\chi_{xx})/3$.

4.4 Dy_4Cr_4 ring

As a second example we describe in this section the application of the decorated Ising model to a ring-shaped Dy_4Cr_4 molecule [3]. Dy_4Cr_4 consists of alternating Dy^{3+} and Cr^{3+} ions forming a closed ring. The four Dy^{3+} ions lie in a plane. The Cr^{3+} ions are positioned alternatingly above and below this plane,[7] "decorating" the Dy-Dy bonds. The molecule has D_{2d} symmetry, the Dy^{3+} ions lying on C_2 axes and the Cr^{3+} ions lying on the mirror planes. We choose a molecular reference frame XYZ so that Z coincides with the S_4 axis and X and Y coincide with the two C_2 axes of D_{2d} (Fig. 4.13).

Ab initio calculations have been performed in the same way as for the [DyCuMoCu] chain [3]. From these, we take again the g-factors of the ground doublet of Dy^{3+} and of the isotropic ground state spin multiplet of Cr^{3+} (d^3, $S = 3/2$):

$$\begin{aligned} \mathrm{Dy}^{3+}: &\qquad g_z = 19.8, \quad g_x = 0, \quad g_y = 0, \\ \mathrm{Cr}^{3+}: &\qquad g_{\mathrm{Cr}} = 1.97. \end{aligned} \tag{4.4.1}$$

The Dy^{3+} Kramers doublet is again very close to the $|M_J = \pm 15/2\rangle$ state, permitting the use of the Ising model. However, the same calculation predicted the second Kramers doublet at $73\,\mathrm{cm}^{-1}$, not very high compared with exchange interaction, which we found in the previous section $\approx 10\,\mathrm{cm}^{-1}$. This should

[7] The molecular structure is pictured in Addendum B.

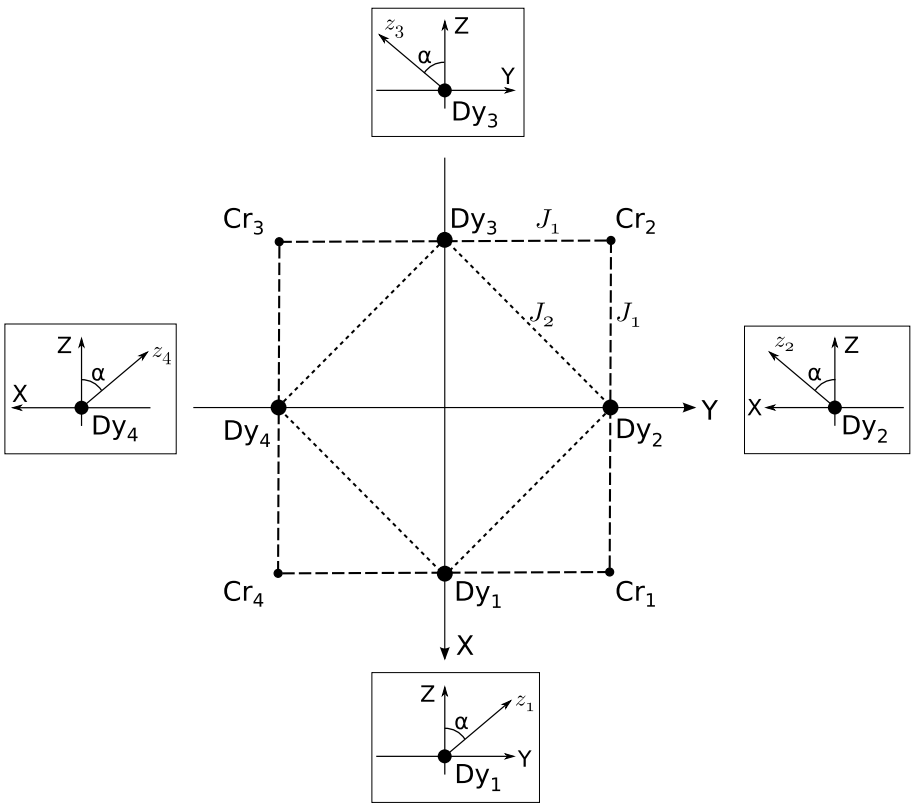

Figure 4.13: Schematic representation of the Dy_4Cr_4 molecule indicating numbering of atoms and exchange coupling constants. The boxes show the orientation of the local anisotropy axes on Dy sites, when viewed from the poles of the X and Y axes. The Z axis points out of the center of the scheme.

be seen as a warning that our treatment of the excited Kramers doublets as "innocent" may not be entirely correct here, and thus may lead to discrepancies with experiment. In this respect we must also note that the results of the *ab initio* calculations are not always conclusive on the nature of the Kramers doublets, owing to the uncertainties connected with the necessary simplifications that have to be introduced to meet the size limitations of the computational method. In the present case, for instance, some calculations produced ground state Kramers doublets on Dy^{3+} that are not quite as uniaxial as in Eq. (4.4.1), with $g_{x,y}$ values of perhaps 1 or 2 [24]. The decorated Ising model would be unusable in this case. This adds an extra uncertainty to the use of the method. In the following we will assume the results in Eq. (4.4.1) to be correct, and proceed to apply the decorated Ising model to this problem.

Direct ligand bridges connect each Dy^{3+} with two neighboring Cr^{3+} ions and two neighboring Dy^{3+} ions. Exchange interaction between these pairs is introduced (Eqs (4.2.13) and (4.2.14)). The Hamiltonian is then given by Eq. (4.2.1): $\hat{H} = \hat{h}_1 + \hat{h}_2 + \hat{h}_3 + \hat{h}_4$, and

$$\hat{h}_i(s_i^{z_i}, s_{i+1}^{z_{i+1}}) = -J_1(s_i^{z_i} S_i^{z_i} + s_{i+1}^{z_{i+1}} S_i^{z_{i+1}}) - J_2 s_i^{z_i} s_{i+1}^{z_{i+1}} - \mu_{\mathrm{B}}(g_{\mathrm{Dy}} s_i^{z_i} B^{z_i} + g_{\mathrm{Cr}} \mathbf{S}_i \cdot \mathbf{B}), \quad (4.4.2)$$

where $s_i^{z_i}$ denotes the Ising spin-1/2 variable on Dy_i and $S_i^{z_i}$ denotes the projection of the spin of Cr_i on the magnetic anisotropy axis of Dy_i (for numbering, see Fig 4.13). Similarly, B^{z_i} is the projection of the magnetic field on the anisotropy axis of Dy_i. g_{Dy} is the g_z factor of Dy^{3+} (Eq. (4.4.1)).

An interesting difference with the [DyCuMoCu] chain is that here, in Dy_4Cr_4, the four anisotropy axes z_i are not, in general, parallel, a result of point instead of translational symmetry. The orientation of the local anisotropy axis on Dy^{3+}, being one of the g-tensor eigenaxes, is restricted by the local C_2 symmetry to be either parallel with, or orthogonal to the local C_2 axis. The first possibility can be excluded on the basis of the experiment; with the z_i pointing radially outwards at each Dy_i, the ground state of the whole molecule is necessarily nonmagnetic, because the local moments add up to zero, independent of whether the ground state is F or AF with respect to the Ising spins (Section 4.2.3). The experimental susceptibility measurement however indicates a magnetic ground state (nonzero intercept on the vertical axis in Fig. 4.14). We must therefore choose the second case and let the anisotropy axis on each Dy be orthogonal to the local C_2 axis and make an angle of α with the molecular Z-axis. (See Fig. 4.13) By applying the symmetry elements of D_{2d} to one of these anisotropy axes, one obtains the other three. When $\alpha = 0$ the four axes are parallel and point in the same direction as Z. We note that the *ab initio* calculations yielded $\alpha = 35°$. We will need some flexibility in our model however, so we leave α as a parameter that will be determined from comparison with experiment.

In terms of the molecular coordinate system, the projections on the local anisotropy axes are a function of α:

$$\begin{aligned} S_i^{z_1} &= \cos(\alpha) S_i^Z + \sin(\alpha) S_i^Y \\ S_i^{z_2} &= \cos(\alpha) S_i^Z + \sin(\alpha) S_i^X \\ S_i^{z_3} &= \cos(\alpha) S_i^Z - \sin(\alpha) S_i^Y \\ S_i^{z_4} &= \cos(\alpha) S_i^Z - \sin(\alpha) S_i^X . \end{aligned} \tag{4.4.3}$$

The same relations hold for the magnetic field, after replacing S_i by B.

The fact that only exchange interactions of Ising type appear in Eq. (4.4.2) makes it possible to find analytical solutions of the eigenvalues and the partition function. From Eqs. (4.4.2) and (4.4.3) we see that the part of $\hat{h}_i$ that involves S_i is a projection of $\mathbf{S}_i$ on the vector

$$- J_1(s_i \hat{\mathbf{z}}_i + s_{i+1} \hat{\mathbf{z}}_{i+1}) - g_{\mathrm{Cr}} \mu_{\mathrm{B}} \mathbf{B}, \tag{4.4.4}$$

where $\hat{\mathbf{z}}_i$ is the unit vector along the anisotropy axis of Dy_i (the superscripts z_i on s_i are left out for clarity from now on). The vector (4.4.4) defines the quantization axis of $\mathbf{S}_i$, which depends on the states on the neighboring Dy^{3+} sites (s_i, s_{i+1}). The stronger the coupling (J_1) with Dy, the stronger will be the deviation of the quantization axis from the direction of $\mathbf{B}$ (given that $\mathbf{B} \neq 0$ of course). The eigenvalues of $\hat{h}_i$ are then

$$\varepsilon_{iM_S}(s_i, s_{i+1}) = b_i M_S - J_2 s_i s_{i+1} - \mu_{\mathrm{B}} g_{\mathrm{Dy}} s_i B^{z_i}, \quad (M_S = -S, \ldots, S), \tag{4.4.5}$$

where

$$b_i = \sqrt{\frac{J_1^2}{2}(1 + 4 s_i s_{i+1} \cos^2 \alpha) + 2 J_1 \mu_{\mathrm{B}} g_{\mathrm{Cr}} (s_i B^{z_i} + s_{i+1} B^{z_{i+1}}) + \mu_{\mathrm{B}}^2 g_{\mathrm{Cr}}^2 B^2} \tag{4.4.6}$$

is the length of the vector in Eq. (4.4.4). Some remarks should be made on the solutions. Eqs. (4.4.6) and (4.4.3) (replace S_i by B) show that the spectrum in Eq. (4.4.5) is not the same for every unit i, as it was in the [DyCuMoCu] chain, unless $\mathbf{B}$ is applied along the Z axis. This means that also the transfer matrices T_i will be different and that we have to use Eq. (4.2.7) instead of Eq. (4.2.8) for the partition function. A second remark concerns the quantum number M_S. The lowest energy in Eq. (4.4.5) is always given by $M_S = -S$, but note that the axis to which this quantization refers is not invariant; in particular, it changes with strength and direction of applied field, so that M_S does not represent a real conserved quantity that could be responsible for level crossings of the "internal" type. Such crossings do not occur in Dy_4Cr_4.

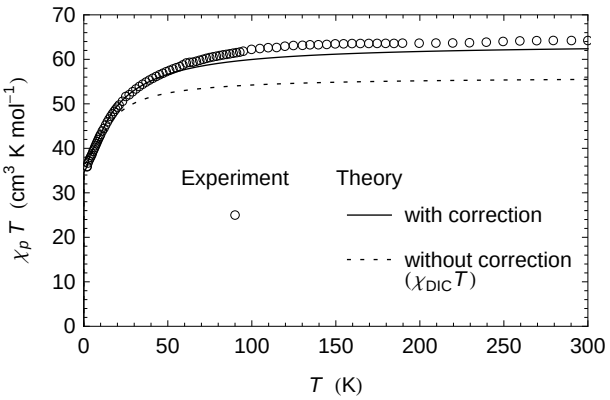

Figure 4.14: Powder magnetic susceptibility of Dy_4Cr_4. The correction on the theory refers to Eq. (4.2.27a).

We conclude the solution by finding the partition function $\mathcal{Z}$. Substituting Eq. (4.4.5) in Eq. (4.2.4) we find

$$\begin{aligned}\Psi_i(s_i, s_{i+1}) &= \sum_{M_S=-S}^{S} e^{-\beta\varepsilon_{iM_S}} \\ &= \frac{\sinh[\beta b_i(2S+1)/2]}{\sinh[\beta b_i/2]} \exp[\beta(J_2 s_i s_{i+1} + \mu_{\mathrm{B}} g_{\mathrm{Dy}} s_i B^{z_i})]\end{aligned}$$

With T_i as defined in Eq. (4.2.6), we obtain the partition function

$$\mathcal{Z} = \mathrm{Tr}(T_1 T_2 T_3 T_4).$$

Let us now compare the theoretical results with experiment. A great amount of information on the values of the parameters α, J_1 and J_2 can be obtained by inspection of the powder $\chi_p T$ curve (Fig. 4.14). The nonzero intercept $\chi_p T|_{T\to 0} = 34.6\,\mathrm{cm^3\,K\,mol^{-1}}$ indicates a magnetic ground state [23]. Now from the general theory we know that the ground state is either F ($\uparrow\uparrow\uparrow\uparrow$) or AF ($\uparrow\downarrow\uparrow\downarrow$) with respect to the Dy^{3+} spins.[8] AF is nonmagnetic so we decide that the ground state must be F.

[8]This result, which was found in Section 4.2.3 for a periodic ring or chain, is valid here because we are considering the eigenstates of Dy_4Cr_4 in the *absence* of magnetic field, in which case the ring is effectively cyclic symmetric.

Incidentally, we can precisely delineate the regions in parameter space where the ground state is F or AF:

$$\mathrm{F}\ (\uparrow\uparrow\uparrow\uparrow) : J_2 > -\sqrt{2}S\left(\sqrt{1+\cos^2\alpha} - \sin\alpha\right)|J_1|, \tag{4.4.7a}$$

$$\mathrm{AF}(\uparrow\downarrow\uparrow\downarrow) : J_2 < -\sqrt{2}S\left(\sqrt{1+\cos^2\alpha} - \sin\alpha\right)|J_1|. \tag{4.4.7b}$$

A second piece of information comes from the increase of $\chi_p T$ with increasing temperature. This is partly but not completely due to the occupation of excited Kramers doublets, as one can show by substracting this contribution obtained from the *ab initio* calculations (not shown here). There must still be an antiferromagnetic interaction to explain the increase. Since the Dy^{3+} are already known to be ferromagnetically coupled, the only possibility is that the Cr^{3+} spins couple antiferromagnetically with Dy^{3+}, or: $J_1 < 0$.

With this information, we can determine the angle α. At 0 K, χT is determined by the magnetic moment in the ground state only [23,25]. In the F ($\uparrow\uparrow\uparrow\uparrow$) state, $\chi_{XX}T|_{T\to 0} = \chi_{YY}T|_{T\to 0} = 0$ by symmetry and

$$\chi_{ZZ}T|_{T\to 0} = \frac{N_A\mu_B^2}{k}\left|\left\langle F\middle| g_{\mathrm{Dy}}\cos\alpha\sum_{i=1}^{4} s_i + g_{\mathrm{Cr}}\sum_{i=1}^{4} S_i^Z\middle| F\right\rangle\right|^2, \tag{4.4.8}$$

so $\chi_p T|_{T\to 0} = \frac{1}{3}\chi_{ZZ}T|_{T\to 0}$. With the help of Eqs. (4.4.3)–(4.4.6) and the fact that, in the ground state, $M_S = -S$ in Eq. (4.4.5), we can evaluate Eq. (4.4.8) to find

$$\chi_p T|_{T\to 0} = \frac{N_\mathrm{A}\mu_\mathrm{B}^2}{3k} 4\cos^2\alpha\left(g_{\mathrm{Dy}} + \mathrm{sgn}(J_1)2\sqrt{2}g_{\mathrm{Cr}}S\frac{1}{\sqrt{1+\cos^2\alpha}}\right)^2.$$

This is a strictly decreasing function of α that can be used to derive α from the experimental value $\chi_p T|_{T\to 0} = 34.6\,\mathrm{cm^3\,K\,mol^{-1}}$, and the knowledge that $\mathrm{sgn}(J_1) = -1$. This gives

$$\alpha = 49^\circ.$$

The remaining exchange coupling constants J_1 and J_2 are determined by comparing the experimental [3] and theoretical curves for powder magnetization and susceptibility. The corrections for excited Dy^{3+} Kramers doublets are provided by the *ab initio* calculations and applied following Eq. (4.2.27). $\mu'_{\mathrm{Dy}} = 0.2\,\mu_\mathrm{B}/\mathrm{T}$ (for the whole molecule), a non-negligible linear contribution to magnetization, which is due to the low-lying excited Kramers doublets.

Best agreement was found for

$$J_1 = -7.8\,\mathrm{cm^{-1}}, \quad J_2 = 5.3\,\mathrm{cm^{-1}}.$$

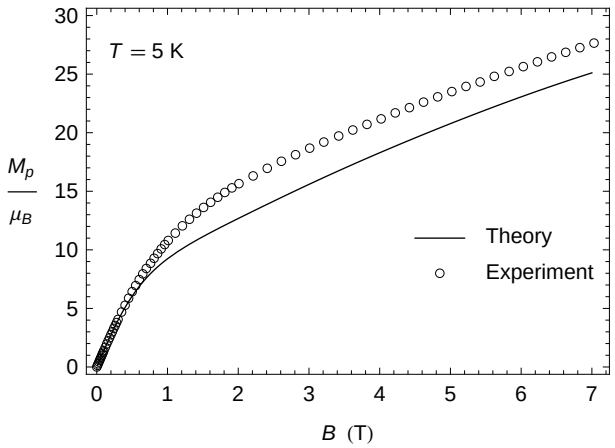

Figure 4.15: Powder magnetization of Dy_4Cr_4. A linear corrections of $0.2\,\mu_B/T$ has been added to the theoretical curve, according to Eq. (4.2.27c).

The comparison is shown in Figs. 4.14 and 4.15. Note that the magnetic properties are reported per mole or molecule of Dy_4Cr_4 and not per DyCr unit. Note also that $\mathrm{sgn}(J_1) = -1$ and that J_2 satifies Eq. (4.4.7a).

The agreement of magnetization curves (Fig. 4.15) is not as good as it was for the $[DyCuMoCu]_\infty$ chain, although the qualitative properties seem to correspond. In particular, we mention the strong linear increase of M_p at higher fields ($\approx 2.6\,\mu_b/T$), which is due to the slow orientation of the Cr^{3+} spins to the magnetic field (see discussion connected with Eq. (4.4.4)) (and, to a small extent, to the correction of $0.2\,\mu_b/T$).

As was mentioned before, the discrepancies are not unexpected given a low-lying first excited Kramers doublet of Dy^{3+}, which could undermine the assumptions underlying the decorated Ising model. Note also that we could not take the *ab initio* value of 35° for α. Leaving α as a parameter can be seen as a partial compensation for the inaccuracies of the model and the *ab initio* results.

4.5 Conclusion

We have shown that the decorated Ising model is a valid model for the magnetic properties of certain lanthanide-containing magnetic compounds, if the crystal field spectrum of the lanthanide ion satisfies certain properties, discussed in Section 4.2.2. The most important of these is the requirement of a ground state Kramers doublet with completely uniaxial magnetic anisotropy (this statement

is simplified, see Section 4.2.2 for the correct details). It is a remarkable fact that precisely this property has been established by multiconfigurational *ab initio* calculations on several Dy^{3+} centers that are part of polynuclear molecular magnets. Perhaps the best known example is the Dy_3 triangle, where the Ising properties of Dy^{3+} were used to explain the nature of the ground state [17].

We have focussed on Dy^{3+} as lanthanide ion because this is a much-used lanthanide in current synthetic research in molecular magnetism (witness both compounds in this paper) and because computational results showing that it meets the requirements for an Ising spin are available. However, there is no reason to assume that the findings are unique to Dy^{3+}. We expect that other lanthanides with high momentum (e.g. Er^{3+}) will exhibit the same uniaxial anisotropy in certain ligand environments and that examples of decorated Ising chains based on lanthanides other than Dy^{3+} will be found in the future.[9]

It has been mentioned several times already that the identification of the compounds as decorated Ising chains or rings depends strongly on the results of the *ab initio* calculations on the lanthanide fragment, which are needed to predict whether the ground state Kramers doublet has the required Ising properties. Given the uncertainties connected with these results, the application of the decorated Ising model remains always open to doubt. *A posteriori* checking of the agreement with experiment helps to confirm the correctness of the model.

Bibliography

[1] M. E. Fisher, Phys. Rev. **113**, 969 (1959)

[2] D. Visinescu, A. M. Madalan, M. Andruh, C. Duhayon, J.-P. Sutter, L. Ungur, W. Van den Heuvel, and L. F. Chibotaru, Chem. Eur. J. **15**, 11808 (2009)

[3] J. Rinck, G. Novitchi, W. Van den Heuvel, L. Ungur, Y. Lan, C. E. Anson, L. F. Chibotaru, and A. K. Powell, (unpublished)

[4] J. Strečka and M. Jaščur, Czech. J. Phys. **52**, A37 (2002)

[5] J. Strečka, M. Jaščur, M. Hagiwara, and K. Minami, Phys. Rev. B **72**, 024459 (2005)

[6] D. Antonosyan, S. Bellucci, and V. Ohanyan, Phys. Rev. B **79**, 014432 (2009)

[7] V. Ohanyan, Condens. Matter Phys. **12**, 343 (2009)

[9] See also Chapter 5.

[8] D. Gatteschi, R. Sessoli, and J. Villain, *Molecular Nanomagnets* (Oxford University Press, Oxford, 2006)

[9] C. Coulon, H. Miyasaka, and R. Clérac, in *Single-Molecule Magnets and Related Phenomena*, Structure and Bonding, Vol. 122, edited by R. Winpenny (Springer-Verlag, Berlin, 2006) pp. 163–206

[10] M. Andruh, J.-P. Costes, C. Diaz, and S. Gao, Inorg. Chem. **48**, 3342 (2009)

[11] R. Sessoli and A. K. Powell, Coord. Chem. Rev. **253**, 2328 (2009)

[12] J. M. Yeomans, *Statistical Mechanics of Phase Transitions* (Oxford University Press, Oxford, 1992)

[13] R. A. Horn and C. R. Johnson, *Matrix analysis* (Cambridge University Press, Cambridge, 1993)

[14] P. W. Anderson, Phys. Rev. **115**, 2 (1959)

[15] A. Abragam and B. Bleany, *Electron Paramagnetic Resonance of Transition Ions* (Clarendon Press, Oxford, 1970)

[16] N. Ishikawa, M. Sugita, T. Okubo, N. Tanaka, T. Iino, and Y. Kaizu, Inorg. Chem. **42**, 2440 (2003)

[17] L. F. Chibotaru, L. Ungur, and A. Soncini, Angew. Chem. **47**, 4126 (2008)

[18] L. Ungur, W. Van den Heuvel, and L. F. Chibotaru, New J. Chem. **33**, 1224 (2009)

[19] K. Bernot, J. Luzon, L. Bogani, M. Etienne, C. Sangregorio, M. Shanmugam, A. Caneschi, R. Sessoli, and D. Gatteschi, J. Am. Chem. Soc. **131**, 5573 (2009)

[20] J. H. Van Vleck, *The Theory of Electric and Magnetic Susceptibilities* (Oxford University Press, London, 1932)

[21] J. F. Nye, *Physical Properties of Crystals* (Oxford University Press, Oxford, 1985)

[22] J.-P. Costes, F. Dahan, A. Dupuis, and J.-P. Laurent, Chem. Eur J. **4**, 1616 (1998)

[23] O. Kahn, *Molecular Magnetism* (VCH Publishers, New York, 1993)

[24] L. Ungur, personal communication

[25] J. S. Griffith, *The Theory of Transition-Metal Ions* (Cambridge University Press, Cambridge, 1964)

Addendum B

Supplements to chapter 4

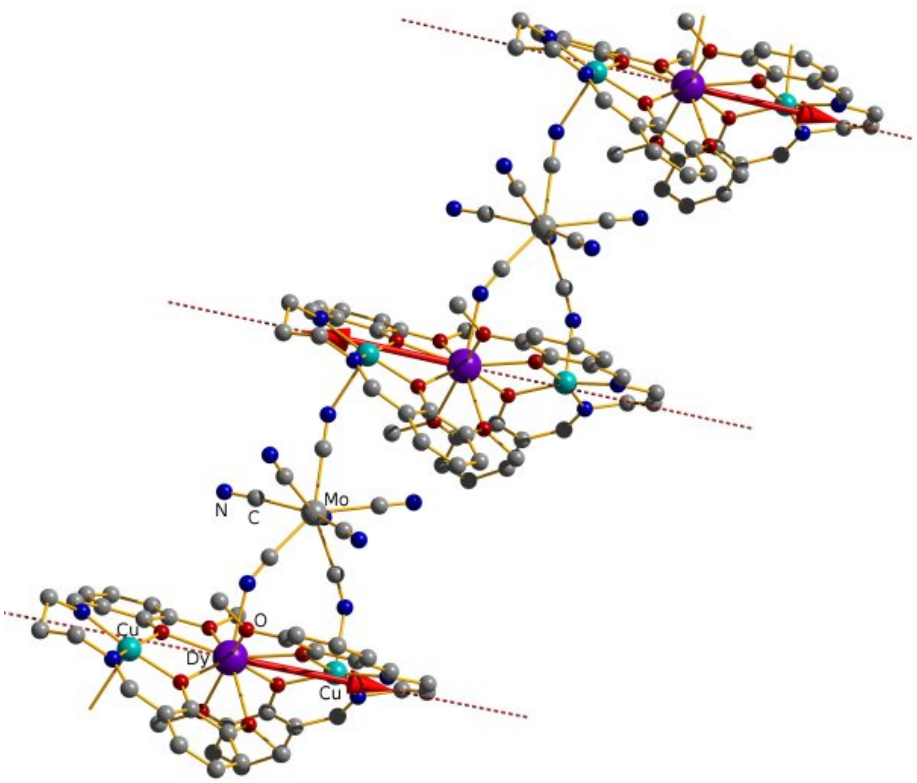

Figure B.1: Part of the $[DyCuMoCu]_\infty$ chain. The dotted line denotes the anisotropy axis of Dy^{3+}, as predicted by the *ab initio* calculations. This is the z axis used in the text. The red arrows represent the antiferromagnetic ground-state configuration of the Ising spins.

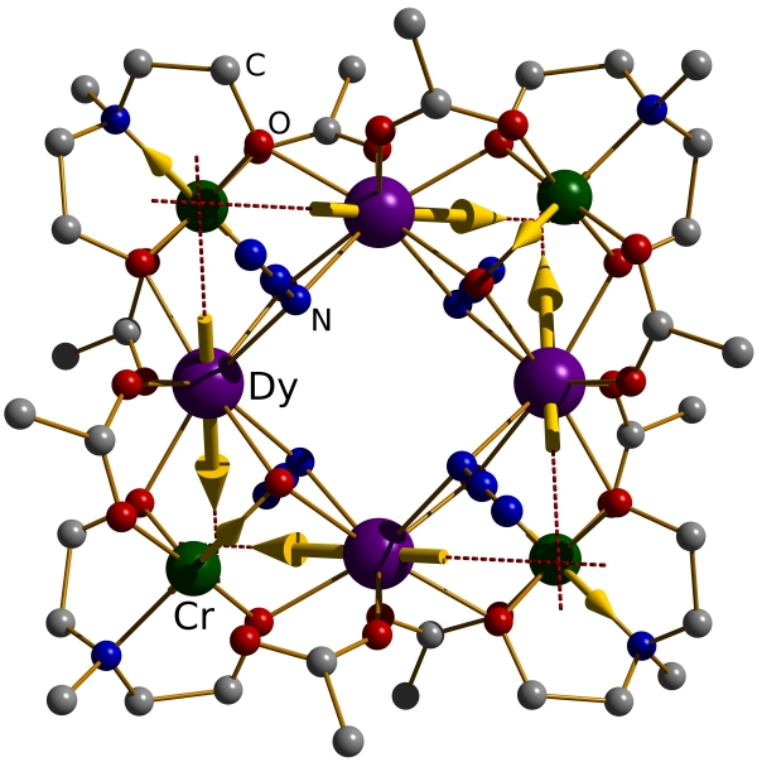

Figure B.2: Sructure of the Dy_4Cr_4 molecule. The arrows represent the spin projections in the ground state. Note that the Cr^{3+} spins are coupled antiferromagnetically to the Dy^{3+} spins.

Chapter 5

Axial magnetic anisotropy of Dy^{3+} and Er^{3+} in crystal fields without symmetry

Abstract The axial magnetic anisotropy of the ground state Kramers doublet of Dy^{3+} ($^6H_{15/2}$) and Er^{3+} ($^4I_{15/2}$) in low-symmetric crystal fields is investigated. Recent *ab initio* calculations have shown that this ground doublet in several Dy^{3+} complexes is close to the axial state $|M_J| = 15/2$, despite a complete lack of local axial symmetry. The second-order part of the crystal field potential is found to be responsible for this. Point charge calculations support the conclusion that the ground Kramers doublet in an arbitrary environment is most likely to be close to $|M_J| = 15/2$.

5.1 Introduction

In recent years, lanthanide ions have been used instead of or in combination with the traditional transition metal ions as magnetic centers in an attempt to make new single-molecule magnets (SMM) and single-chain magnets (SCM) (See [1] and references therein). The interest in doing this arose when slow relaxation of magnetization (at low temperature) was discovered in some mononuclear doubledecker bis(phtalocyaninato) lanthanide complexes [2]. In these complexes, the splitting of the $^{2S+1}L_J$ ground level by the crystal field perturbation of the ligands results in an energy barrier for reorientation of magnetization, which is a characterizing property of SMMs [3].

Lanthanide ions are thought to be promising constituents of SMMs because of their high magnetic moment (at least those of the second half of the $4f$

W. Van den Heuvel and L. F. Chibotaru, unpublished manuscript

series, see Table 5.6) and strong magnetic anisotropy. Lanthanide complexes differ from most transition metal complexes in the way the ligand field induces this magnetic anisotropy. In a polynuclear transition metal complex in which orbital angular momentum of the ions is quenched by the ligand field, spin-orbit coupling acts as a perturbation that breaks the isotropy of the ground state spin multiplet only in second order. The perturbative nature of the splitting means that the effective field felt by the spin is often of much higher symmetry than the real symmetry of the molecule. For example, a fourfold symmetry axis is sufficient to make the second-order perturbation effectively cylindrical (i.e. proportional to S_z^2). Terms that destroy the cylindrical symmetry arise only in fourth order of perturbation and are therefore of subordinate importance [3]. The DS_z^2 potential splits the S level in $\pm M_S$ doublets, with a barrier for reorientation ($M_S \leftrightarrow -M_S$) of the magnetic moment (if $D < 0$) [3].

The situation is quite different in lanthanide complexes. Consider a lanthanide ion coordinated by ligands. Here, the perturbation is the crystal field potential and it destroys the spherical symmetry of the ${}^{2S+1}L_J$ state already in first order of perturbation. The splitting pattern will therefore be more directly influenced by the coordination environment than in the transition metal complex described in the previous paragraph. For example, no comparable hierarchy in the relative importance of the crystal field terms of second order compared to fourth and sixth order (after J) is expected, at least not on the basis of perturbation theory. Let us expand the crystal field potential energy in the usual way in spherical harmonics $Y_{km}(\theta, \phi)$ [4]. We write

$$C_m^{(k)}(\theta, \phi) = \sqrt{\frac{4\pi}{2k+1}} Y_{km}(\theta, \phi).$$

In f^n electronic configurations, only spherical harmonics of zeroth, second, fourth, and sixth order have non-zero matrix elements. The zeroth order term is a constant energy, which we may disregard. So we have the expansion of the crystal field perturbation:

$$V(\theta, \phi) = \sum_{k \in \{2,4,6\}} \sum_{m=-k}^{k} q_{km} C_m^{(k)}(\theta, \phi), \tag{5.1.1}$$

where the radial part of V has already been integrated over the radial part of the $4f$ orbitals. This information is contracted in the complex q_{km} coefficients ($q_{k-m} = (-1)^m q_{km}^*$). To obtain an effective cylindrical symmetry, we must have $q_{km} = 0$ for $m \neq 0$. This requires an eightfold symmetry axis. The remaining $m = 0$ terms in V are a mixture of J_z^2, J_z^4, and J_z^6, after transforming to operator equivalents in the ${}^{2S+1}L_J$ level. No relative ordering of strenghts of these terms can be presupposed however, because they all arise in the first order of perturbation theory. A quadratic barrier of magnetization DJ_z^2, in analogy with DS_z^2 in transition metal SMMs, is therefore not expected in lanthanide

complexes. This is indeed what was found in the bis(phtalocyaninato) lanthanide complexes, which have an S_8 rotation-inversion axis [2,5]. Under the effective cylindrical symmetry, the $^{2S+1}L_J$ level splits in $|\pm M_J\rangle$ doublets, eigenfunctions of J_z (z is the S_8 axis), but the energy of these doublets does not follow a quadratic law in $|M_J|$. One consequence of this is that the lowest-energy doublet is not necessarily the one with highest or lowest possible $|M_J|$ value, but may instead have intermediate $|M_J|$ value [2,5].

A quadratic "double well" potential is however not necessary to observe slow relaxation of magnetization. The study of the doubledecker lanthanide complexes indicated that slow relaxation is likely to occur when the lowest doublet has a high value of $|M_J|$ (e.g. $|M_J| = 13/2$ in Dy^{3+} and $|M_J| = 6$ in Tb^{3+} [2]; compare with $|M_S| = 10$ in the Mn_{12}ac SMM [3]) and is separated from the next doublet by an energy large compared to kT.

In this note we are concerned with the occurence of uniaxial (i.e. cylindrical) anisotropy in lanthanide complexes without any symmetry. This effect was noted in the course of several *ab initio* calculations performed on Dy^{3+} centers in polynuclear complexes to model the magnetic properties of the complex [6–9]. These calculations revealed that the ground state doublet (Dy^{3+} is a Kramers ion) is often very close to the cylindrical doublet of maximum projection $|M_J| = 15/2$.[1] The Dy^{3+} ions in these complexes are mostly coordinated by eight atoms, mostly oxygen and nitrogen, belonging to organic ligands or small molecules like water, and occasionally chloride. The number of investigated complexes is not large, given the complexity of the time-consuming multiconfigurational (CASSCF/RASSI-SO) quantum chemical calculations, but the available results indicate that the $|M_J| = 15/2$ ground state is not an accidental feature of one particular complex, but is found in several complexes that have in common a lack of symmetry of the coordination around Dy^{3+}. This finding is remarkable because uniaxial crystal field states normally require an eightfold symmetry axis, as in the doubledecker lanthanides. The fact that $|M_J| = 15/2$ is very likely to be the ground state in low-symmetry coordination is important for the single-molecule magnetism of polynuclear complexes, in which local symmetry of metal centers is usually low or absent. It means that highly axial crystal fields, like in the lanthanide doubledeckers, are not necessary to obtain a highly axial ground doublet, which is supposed to be a necessary ingredient of SMM behavior.

Let us take a closer look at the problem by means of an example, which shows all the qualitative features we will adress in this work. Table 5.1 shows the lowest part of the crystal field spectrum of one Dy^{3+} center in a Dy_3 triangular complex (Dy(1) in Fig. 5.1). For details on the calculations we refer to [6] and [7]. The eight Kramers doublets originate from the $^6H_{15/2}$ ground level.

[1] See also Chapter 4, Section 4.2.2.

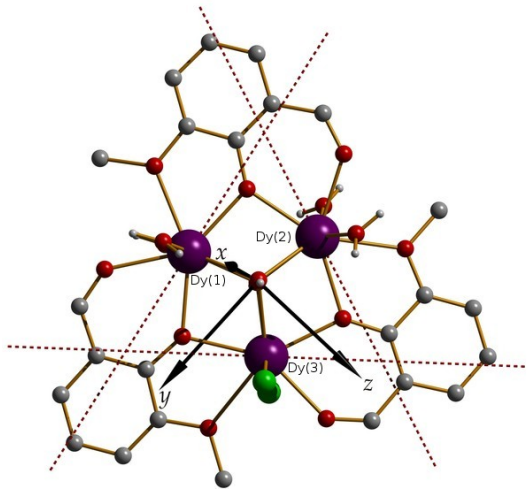

(a)

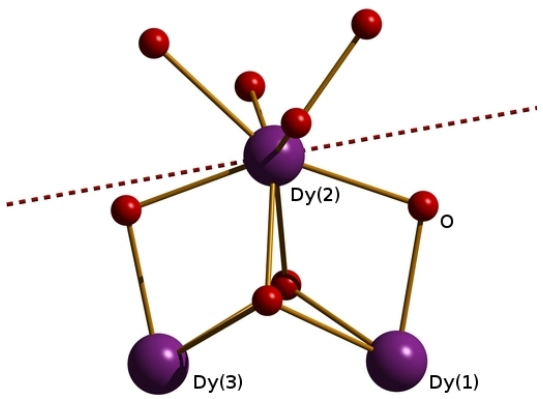

(b)

Figure 5.1: (a) Molecular structure of the Dy_3 triangle. Purple: Dy^{3+}, red: O, green: Cl, grey: C, white: H. The dashed lines are the calculated [6] directions of uniaxial magnetic anisotropy of the ground Kramers doublet on each Dy^{3+} site. See Table 5.1 for the example of Dy(1). (b) The coordination polyhedron around dysprosium is a distorted trigonal dodecahedron.

Table 5.1: *Ab initio* results for the eight Kramers doublets (KD) originating from the $^6H_{15/2}$ ionic level of one Dy^{3+} center in the Dy_3 triangle (Dy(1) in Fig. 5.1). For each Kramers doublet, energy, principal g factors and corresponding directions are tabulated. Note that the sign of the g factors is undetermined and chosen positive throughout.

KD	Energy (cm^{-1})	g factors	Magnetic axes		
			x	y	z
		0.00	0.45	−0.16	0.88
1	0	0.00	0.89	0.07	−0.45
		19.84	0.01	0.98	0.17
		0.15	−0.37	0.10	0.93
2	234	0.17	0.93	0.08	0.36
		17.23	0.04	−0.99	0.12
		2.15	0.08	0.23	0.97
3	373	3.92	0.99	0.10	−0.11
		12.26	−0.12	0.97	−0.22
		1.40	0.37	0.78	−0.50
4	449	3.94	−0.11	0.57	0.81
		8.79	0.92	−0.25	0.30
		0.36	0.78	−0.63	−0.04
5	501	3.96	0.13	0.22	−0.97
		8.78	0.61	0.75	0.25
		2.12	−0.09	0.89	−0.44
6	554	4.52	0.93	0.24	0.28
		11.89	−0.36	0.38	0.85
		0.55	−0.38	−0.92	0.12
7	658	0.63	0.88	−0.40	−0.24
		16.55	0.27	0.01	0.96
		0.06	0.21	0.97	0.08
8	741	0.10	−0.97	0.20	0.15
		19.3	0.13	−0.11	0.99

Table 5.2: g factors of the Kramers doublets that are eigenfunctions of J_z. The exact values are $g_\parallel = 2g_J|M_J|$ and $g_\perp = 0$, except for $|M_J| = 1/2$, where $g_\perp = 8g_J$. The Landé factor g_J equals 4/3 for $^6\mathrm{H}_{15/2}$ and 6/5 for $^4\mathrm{I}_{15/2}$.

	Dy^{3+} ($^6\mathrm{H}_{15/2}$)		Er^{3+} ($^4\mathrm{I}_{15/2}$)	
$\lvert M_J\rvert$	$g_\parallel$	$g_\perp$	$g_\parallel$	$g_\perp$
$\frac{15}{2}$	20.00	0	18.00	0
$\frac{13}{2}$	17.33	0	15.60	0
$\frac{11}{2}$	14.67	0	13.20	0
$\frac{9}{2}$	12.00	0	10.80	0
$\frac{7}{2}$	9.33	0	8.40	0
$\frac{5}{2}$	6.67	0	6.00	0
$\frac{3}{2}$	4.00	0	3.60	0
$\frac{1}{2}$	1.33	10.67	1.20	9.60

For each doublet, principal g factors and corresponding magnetic eigenaxes were calculated. These give a good indication of the composition of the wavefunction and are useful to asses the magnetic "axiality" of a doublet. Each Dy^{3+} ion resides in a nonsymmetrical environment, coordinated by eight atoms which form a distorted trigonal dodecahedron [10] but belong to different ligands and are even of different atomic type on Dy(3). Nevertheless, the spectra of all three Dy^{3+} centers show the same *qualitative* features as in Table 5.1, namely

1. The ground doublet is very close to $|M_J| = 15/2$.
2. The g factors exhibit an approximate inversion symmetry, located between KD 4 and KD 5.

Point 1. is clear if one compares the g values of the ground doublet with those in Table 5.2. Note also that the second doublet in Table 5.1 is not far from $|M_J| = 13/2$, etc. but the deviations from M_J doublets increase strongly when approaching the middle of the spectrum, where the situation is totally blurred and there is no trace of axial symmetry. The higher doublets however, become gradually more axial again, culminating in KD 8, which is, like KD 1, very close to $|M_J| = 15/2$. This pattern is expressed in point 2.

The appearance in the crystal field spectrum of *two* doublets that are close to the maximum projection of angular momentum is interesting. From Table 5.1 one can see that the anisotropy axes (i.e. the axis corresponding to the largest g factor) of KD 1 and KD 8 are approximately orthogonal. This follows from the requirement that the wavefunctions of different energy levels are mutually

Table 5.3: Parameters of Dy^{3+} and Er^{3+} ions. g_J is the Landé g factor. The $\langle r^n \rangle$ values are from Freeman and Watson [12].

		Ground state					$\langle r^2 \rangle$	$\langle r^4 \rangle$	$\langle r^6 \rangle$
		L	S	J	g_J	$g_J \cdot J$	(a_0^2)	(a_0^4)	(a_0^6)
Dy^{3+}	$4f^9$	5	$\frac{5}{2}$	$\frac{15}{2}$	$\frac{4}{3}$	10	0.726	1.322	5.102
Er^{3+}	$4f^{11}$	6	$\frac{3}{2}$	$\frac{15}{2}$	$\frac{6}{5}$	9	0.666	1.126	3.978

orthogonal. Take the cylindrical doublet $|J, \pm J\rangle$, quantized along z. If we want a second $|J, \pm J\rangle$ doublet to be orthogonal to the first, it cannot be quantized along z as well, for then the second doublet is identical with the first. The quantization axis z' of the second doublet must be rotated with respect to z, and this as far as possible to reduce the overlap with the first doublet, i.e. z' must be perpendicular to z. Let us apply this to the doublet of maximum projection $|J, \pm J\rangle$. A rotation of $\pi/2$ about, say, the y axis sends the quantization axis from z to x. We calculate the overlap element

$$\langle JJ|\hat{C}_4^y|JJ\rangle = D^J_{JJ}\left(0, \frac{\pi}{2}, 0\right) = 2^{-J},$$

where $D^J_{MM'}(\alpha, \beta, \gamma)$ is an element of the Wigner rotation matrix for Euler angles (α, β, γ) [11]. This is the minimum attainable overlap for any rotation. It shows that it is not possible to obtain two orthogonal doublets of maximum projection, but it also shows that the deviation from orthogonality decreases exponentially with J. We have $2^{-\frac{15}{2}} = 0.0055$, so a slight correction of the wavefunctions should be enough to make them orthogonal. The particular feature of the crystal field spectrum that KD 1 and KD 8 are approximately angular momentum doublets of maximum projection, can therefore exist only because J is fairly large in Dy^{3+}.

The thus far described features of the crystal field spectrum of Dy^{3+} in nonsymmetrical complexes, motivate a study with crystal field theory. The main result of these calculations is that the properties noted in points 1. and 2. above arise and are stable in a crystal field potential V, Eq. (5.1.1), containing only $k = 2$ spherical harmonics. It other words, the observed pattern can be explained, assuming that, in the complexes under consideration, the $k = 4$ and $k = 6$ terms in V have a subordinate role.

It is interesting to note that a simple application of the point charge crystal field approximation predicts that the fourth- and sixth-order terms are dominated by the second-order terms. A point charge $-Z_i e$ positioned at a distance a_i from the nucleus and with spherical coordinates (θ_i, ϕ_i), exerts a crystal field

potential (5.1.1) with [4, 10]

$$q_{km} = \sqrt{\frac{4\pi}{2k+1}} Z_i e^2 \frac{\langle r^k \rangle}{a_i^{k+1}} Y_{km}^*(\theta_i, \phi_i). \tag{5.1.2}$$

$\langle r^k \rangle$ is the expectation value of r^k in the $4f$ orbitals. A typical distance between lanthanide and coordinating atom is $a = 5\,a_0$ (a_0 is the Bohr radius). With this value and using calculated values for $\langle r^k \rangle$ [12] (Table 5.3), we find the ratios

$$\frac{\langle r^4 \rangle / a^5}{\langle r^2 \rangle / a^3} = \frac{1}{5^2} \frac{\langle r^4 \rangle}{\langle r^2 \rangle} = 0.073,$$
$$\frac{\langle r^6 \rangle / a^7}{\langle r^2 \rangle / a^3} = \frac{1}{5^4} \frac{\langle r^6 \rangle}{\langle r^2 \rangle} = 0.011,$$

for Dy^{3+}. Note also that a relative dominance of one order over another can not result from a great difference in magnitude of the reduced matrix elements of $C^{(k)}$ because, as Table 5.7 in the appendix shows, they are all of the same order of magnitude.

On the other hand it is known from empirical lanthanide spectroscopy that these ratios underestimate the contribution of fourth- and sixth-order harmonics to the crystal field potential in many compounds [13]. For example, we mentioned before that in the lanthanide doubledecker complexes the empirically derived spectrum does not at all fit a potential with only second-order terms [5]. Contrary to these highly axially symmetric compounds however, the properties we wish to address here are observed in complexes with no symmetry at all. It seems that, at least to describe some striking constants in these systems, such as the highly uniaxially anisotropic ground Kramers doublet, the fourth- and sixth-order harmonics may be ignored.

In this paper we will compare Dy^{3+} with Er^{3+}. Dy^{3+} has had most success recently in new complexes exhibiting single-molecule magnetism [1]. It were *ab initio* calculations on some of these compounds that motivated the investigation of which the results are reported here. Dy^{3+} and Er^{3+} are, among the lanthanides, the Kramers ions with the highest angular momentum J and the highest magnetic moment $g_J J$ (see Table 5.6). The fact that they are Kramers ions is of course of great importance for the ions to remain magnetic in nonsymmetrical complexes. Er^{3+} is interesting to compare with Dy^{3+} because it has the same angular momentum ($J = 15/2$) in the free-ion ground level. However, the sign of the reduced matrix element of the second-order spherical harmonic is opposite to that of Dy^{3+} (Table 5.7). So far, Er^{3+} has been much less used than Dy^{3+} in the synthesis of new SMMs. The results indicate however that Er^{3+} is very much like Dy^{3+}, despite the opposite sign of the reduced matrix element.

5.2 Calculations

The crystal field Hamiltonian is

$$H_{\mathrm{CF}} = \sum_{\kappa=1}^{n} V(\theta_\kappa, \phi_\kappa), \tag{5.2.1}$$

where κ runs over the f electrons and V is given in Eq. (5.1.1). H_{CF} is diagonalized numerically in the ${}^{2S+1}L_J$ ground level of the trivalent lanthanide ion. No interaction with higher J levels is considered. The matrix elements of the different constituents of V are factored in a product of a Clebsch–Gordan coefficient and a reduced matrix element (Wigner–Eckart theorem):

$$\langle LSJM_J| \sum_{\kappa=1}^{n} C_m^{(k)}(\theta_\kappa, \phi_\kappa) |LSJM'_J\rangle = \langle km, JM'_J|JM_J\rangle \langle LSJ||C^{(k)}||LSJ\rangle.$$

The reduced matrix elements are listed in Table 5.7.

Diagonalization of H_{CF} in the $J = 15/2$ ground level of Dy^{3+} or Er^{3+} yields eight Kramers doublets. For each Kramers doublet, principal g factors and corresponding magnetic eigenaxes are calculated by diagonalizing the tensor G. If g is the g matrix in the spin Hamiltonian of a doublet state [13], then $G = gg^T$. The g factors are the square roots of the eigenvalues of G. If $|a\rangle$ and $|b\rangle$ form a basis of the Kramers doublet, then the elements of G are [14]

$$G_{\alpha\beta} = \frac{2}{\mu_{\mathrm{B}}^2} \sum_{i,j\in\{a,b\}} \langle i|\mu_\alpha|j\rangle\langle j|\mu_\beta|i\rangle,$$

where α and β are Cartesian components. The magnetic moment $\boldsymbol{\mu}$ in a J level is proportional to the angular momentum [13]:

$$\boldsymbol{\mu} = -\mu_{\mathrm{B}} g_J \mathbf{J}.$$

g_J is the Landé factor [13]. Because $|a\rangle$ and $|b\rangle$ are expanded in the basis $|JM_J\rangle$, the evaluation of the matrix elements in G is simply a matter of angular momentum algebra.

5.3 Results

5.3.1 Second-order crystal field

We will now pursue the assumption set out in the introduction: we ignore fourth- and sixth-order terms in the crystal field perturbation V, and keep only

the second-order terms. A general second-order potential is described by five independent, real parameters, that can be be arranged in a symmetric, traceless second-rank tensor. This tensor can always be diagonalized by an orthogonal transformation. Hence, choosing a suitable orientation of the Cartesian axes, we can write any second-order potential in the form

$$V^{(2)} = q_\theta Y_{z^2} + q_\epsilon Y_{x^2-y^2}, \tag{5.3.1}$$

with the real variants ("d-orbitals") of the spherical harmonics

$$\begin{aligned} Y_{z^2} &= Y_{20} = N(2z^2 - x^2 - y^2), \\ Y_{x^2-y^2} &= \frac{1}{\sqrt{2}}(Y_{22} + Y_{2-2}) = N\sqrt{3}(x^2 - y^2). \end{aligned} \tag{5.3.2}$$

The number of parameters has been reduced from five to two (q_θ, q_ϵ); three degrees of freedom have gone into the rotation of the coordinate frame. A further reduction of the size of parameter space is still possible, because, after having fixed the coordinate frame in (5.3.1), the labeling of the axes as x, y, z is still arbitrary. Any rotation that permutes the axes may still be applied to (5.3.1)[2] With this information one can verify that all the unique second-order potentials, i.e. those that cannot be transformed into each other by a rotation, are given by

$$V^{(2)}(\gamma) = Q\left((2-\gamma)Y_{z^2} + \sqrt{3}\gamma Y_{x^2-y^2}\right), \qquad \begin{cases} 0 \le \gamma \le 1 \\ Q \ge 0 \end{cases} \tag{5.3.3}$$

This form of $V^{(2)}$ was chosen to exploit the symmetry of the parameter space, as we will see below. It's a way to express that q_ϵ/q_θ can run form 0 to $\sqrt{3}$. Q is a parameter that only scales the energy. The eigenstates of $H^{(2)}_{\mathrm{CF}}$, Eq. (5.2.1), are determined by γ alone.

We proceed now to uncover a certain symmetry in the spectrum of $H^{(2)}_{\mathrm{CF}}$. Consider a rotation of 90 degrees about x, represented by the operator $\hat{C}^x_4$. It is not difficult, using (5.3.2), to show that

$$\hat{C}^x_4 V^{(2)}(\gamma) = -V^{(2)}(1-\gamma).$$

Because $H^{(2)}_{\mathrm{CF}}$ is given by Eq. (5.2.1), the last identity holds for $H^{(2)}_{\mathrm{CF}}(\gamma)$ as well. Let $|\psi\rangle$ be an eigenstate of $H^{(2)}_{\mathrm{CF}}(\gamma)$:

$$H^{(2)}_{\mathrm{CF}}(\gamma)|\psi\rangle = E|\psi\rangle. \tag{5.3.4a}$$

[2]I.e. any rotation of the octahedral group O. Y_{z^2} and $Y_{x^2-y^2}$ form a basis for the irreducible representation E of O.

Applying $\hat{C}_4^x$ on both sides gives

$$H_{\mathrm{CF}}^{(2)}(1-\gamma)\big(\hat{C}_4^x|\psi\rangle\big) = -E\big(\hat{C}_4^x|\psi\rangle\big). \tag{5.3.4b}$$

So, the spectrum of $H_{\mathrm{CF}}^{(2)}(1-\gamma)$ is the inverse of the spectrum of $H_{\mathrm{CF}}^{(2)}(\gamma)$, and the eigenstates of the former are those of the latter rotated over 90 degrees about x.

At the special point $\gamma = 1/2$, we have $H_{\mathrm{CF}}^{(2)}(\gamma) = H_{\mathrm{CF}}^{(2)}(1-\gamma)$, and the previous equations tell us that the spectrum then coincides with its own inverse. This is shown in Table 5.4. We must note that in diagonalizing $H_{\mathrm{CF}}^{(2)}$ in the $J = 15/2$ ground level of Dy^{3+} or of Er^{3+}, there is only one difference and that is that the reduced matrix element of the second-order harmonic is negative for Dy^{3+} but positive for Er^{3+} (see Table 5.7). Consequently the relative position of the eigenstates and the eigenstates themselves are exactly the same but their order is *inversed*: the lowest Kramers doublet of Er^{3+} is the highest Kramers doublet of Dy^{3+}, etc.[3] Therefore, in Table 5.4 the KDs are listed according to increasing energy ($1 \rightarrow 8$) for Dy^{3+} and decreasing energy for Er^{3+}. The column headed g/g_J contains the g factors normalized to the Landé factor. This makes comparison more convenient; as remarked already, KDs on the same horizontal line in the Table are identical, but their g factors are different because $g_J = 4/3$ for Dy^{3+} but $g_J = 6/5$ for Er^{3+}. The maximum value of g/g_J is 15 (in the $|M_J| = 15/2$ doublet), corresponding to $g = 20$ in Dy^{3+} and $g = 18$ in Er^{3+} (see also Table 5.2).

Note how KDs 1,2,3,4 are identical with 8,7,6,5, respectively, after rotation of 90 degrees about x.

The spectrum of $H_{\mathrm{CF}}^{(2)}$ shown in Table 5.4 displays essentially all the qualitative features that we have observed in the *ab initio* crystal field spectrum of Dy^{3+} in the introduction (compare Table 5.1 with Table 5.4). In particular, we find a ground KD that is almost uniaxial (g_x and g_y are smaller than 10^{-3}) and, with $g_z = 19.90$ is very nearly equal to the cylindrical doublet $|M_J| = 15/2$, although the crystal field is not nearly cylindrical.[4] At the same time we find that the eigenstate spectrum of Er^{3+} is identically the same as that of Dy^{3+}, apart from a rotation of 90 degrees about x. This follows from the combination of the particular inversion symmetry *within* one spectrum, connected with (5.3.4) at $\gamma = 1/2$, and the fact that the spectrum of Er^{3+} is the inverse of that of Dy^{3+} (due to the opposite sign of the second-order reduced matrix element).

[3] But note that this is not true if the complete crystal field Hamiltonian, including fourth and sixth order harmonics, is diagonalized, because then the ratios of the reduced matrix elements of different k come into play, and these are not the same for both ions (Table 5.7).

[4] $V^{(2)}$ is only cylindrically symmetric when $\gamma = 0$ or 1. Otherwise it has D_{2h} symmetry.

Table 5.4: Principal g factors (rounded) and axes of the Kramers doublets generated by the crystal field $V^{(2)}$ at the symmetric point $\gamma = 1/2$. (See Eq. (5.3.3))

Dy^{3+}			Er^{3+}		Axis		
KD	g	g/g_J	g	KD	x	y	z
	0.00	0.00	0.00		0	1	0
1	0.00	0.00	0.00	8	1	0	0
	19.90	14.92	17.91		0	0	1
	0.02	0.02	0.02		0	1	0
2	0.03	0.02	0.03	7	1	0	0
	16.96	12.72	15.26		0	0	1
	0.46	0.34	0.41		0	1	0
3	0.64	0.48	0.58	6	1	0	0
	13.72	10.29	12.35		0	0	1
	3.54	2.65	3.18		0	1	0
4	4.66	3.50	4.19	5	1	0	0
	9.10	6.82	8.19		0	0	1
	3.54	2.65	3.18		0	0	1
5	4.66	3.50	4.19	4	1	0	0
	9.10	6.82	8.19		0	1	0
	0.46	0.34	0.41		0	0	1
6	0.64	0.48	0.58	3	1	0	0
	13.72	10.29	12.35		0	1	0
	0.02	0.02	0.02		0	0	1
7	0.03	0.02	0.03	2	1	0	0
	16.96	12.72	15.26		0	1	0
	0.00	0.00	0.00		0	0	1
8	0.00	0.00	0.00	1	1	0	0
	19.90	14.92	17.91		0	1	0

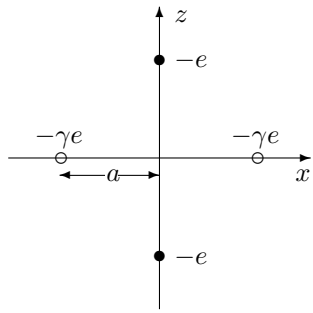

Figure 5.2: Point charge model for $V^{(2)}(\gamma)$.

We have only considered one particular second-order crystal field so far, namely $\gamma = 1/2$. The next question is what the spectrum looks like in an arbitrary second-order field, i.e. for γ between 0 and 1 in Eq. (5.3.3).

If one wishes to attach a physical picture to γ, consider the point charge configuration in Fig. 5.2. Four negative point charges are arranged in a square around the lanthanide nucleus, at a distance a. Two points on the z axis bear a constant charge of $-e$, while two points on the x axis have charge $-\gamma e$. The second-order potential of this configuration is given by (5.3.1), with

$$q_\theta = (2-\gamma)e^2\frac{\langle r^2\rangle}{a^3}, \qquad q_\epsilon = \sqrt{3}\gamma e^2\frac{\langle r^2\rangle}{a^3}, \tag{5.3.5}$$

which corresponds to Eq. (5.3.3), with $Q = e^2\langle r^2\rangle/a^3$. So, increasing γ from 0 to 1 corresponds, in second-order potential, with going from a field axially symmetric around z (only charges on the z axis) to a field axially symmetric around y (four equal charges in a square in the xz plane).

Fig. 5.3 shows the variation of energies of the eight Kramers doublets as function of γ. The energy factor Q was chosen to be that of the square point charge model, Eq. (5.3.5), for a distance a of five Bohr radii. The plot shows the results for Dy^{3+}. To obtain the plot for Er^{3+}, one only has to multiply the energies with the *negative* scaling factor $\frac{\langle r^2\rangle_{\mathrm{Er}}}{\langle r^2\rangle_{\mathrm{Dy}}}\frac{\langle LSJ||C^{(2)}||LSJ\rangle_{\mathrm{Er}}}{\langle LSJ||C^{(2)}||LSJ\rangle_{\mathrm{Dy}}}$. This inverts the order of energy levels, as noted before.

One notes in the plot the inversion symmetry around the central point $(0.5, 0)$, as predicted by (5.3.4). At $\gamma = 0$ and $\gamma = 1$, $V^{(2)}$ is cylindrically symmetric around z and y, respectively. The eigenstates at these points are the angular momentum doublets $|M_J|$, and their energy is proportional to $|M_J|^2$.

To follow the variation of the g factors of every Kramers doublet with γ would be impractical and not very interesting either. We will focus on the lowest doublet alone, whose properties are normally of most importance for the low

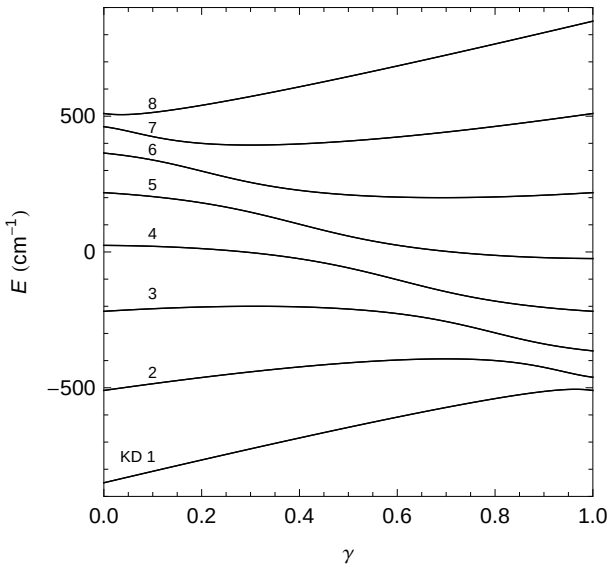

Figure 5.3: Energies of the Kramers doublets of $J = 15/2$ in the second-order crystal field $V^{(2)}(\gamma)$. $Q = e^2\langle r^2\rangle/a^3$, $a = 5a_0$. The energy scale is for Dy^{3+}.

temperature magnetic behavior of the complex. The variation of the g factors of this doublet with γ is plotted in Fig. 5.4. The g factors are scaled to g_J to make comparison between Dy^{3+} and Er^{3+} possible. The plot for Er^{3+} can be obtained from that of Dy^{3+} by the substitutions $\gamma \to 1-\gamma$ and $g_y \leftrightarrow g_z$, again a result of the opposite reduced matrix elements and property (5.3.4). It is equivalent to say that Fig. 5.4(b) shows the g factors of the *highest* Kramers doublet (KD 8) of Dy^{3+} and Fig. 5.4(a) shows the g factors of the *highest* Kramers doublet of Er^{3+}. At the far left of Fig. 5.4(a) and the far right of Fig. 5.4(b), we have the uniaxial g factors of the $|M_J| = 15/2$ doublet. The figure shows that this state remains stable for most of the values of γ. Less anisotropic doublets, like KD 4 in Table 5.4, never occur as ground state.

If we denote by "axiality" the extent to which the lowest doublet approximates $|M_J| = 15/2$, we may say that the axiality of Dy^{3+} decreases with increasing γ while the axiality of Er^{3+} increases with increasing γ.

5.3.2 Point charge calculations for CN=8

The results from the previous section have made it plausible that the ground Kramers doublet of Dy^{3+} or Er^{3+} in an arbitrary environment has a high probability to be close to the doublet of maximum angular momentum projection

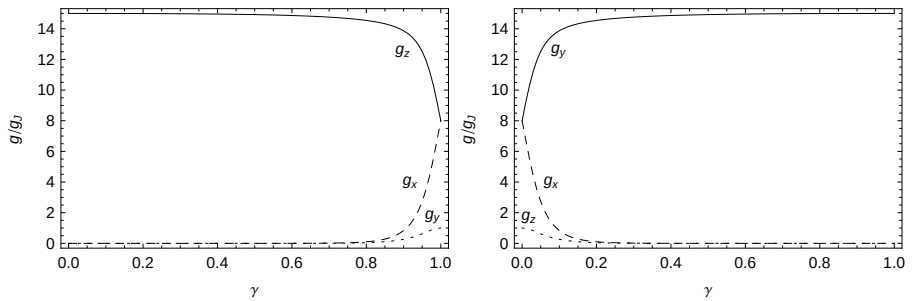

(a) Dy^{3+} (b) Er^{3+}

Figure 5.4: g factors of the lowest Kramers doublet of $J = 15/2$ in the second-order crystal field $V^{(2)}(\gamma)$.

$|M_J| = 15/2$. We had to assume first that the crystal field is dominated by the second-order harmonics. Then, all possible fields of this form were represented by an abstract parameter γ between 0 and 1. However, we do not know which values of γ are more likely to occur than others in real complexes. If, for example, γ is most probably found between 0.9 and 1, then it is not likely for Dy^{3+} to have an highly axial ground doublet at all (Fig. 5.4(a)).

In this section we assume that the point charge model can give us some information on the probability distribution of crystal fields. We consider the lanthanide ion surrounded by eight negative point charges at a distance of $a = 5\,a_0$ ($\approx 2.65\,\text{Å}$). Eight is the most common coordination number (CN) in lanthanide complexes. The asymmetry of the complex is modeled in three different ways.

A. The point charges are fixed on the vertices of an ideal trigonal dodecahedron in the hard-sphere model (see Fig. 5.5 and Refs. [15] and [10] for a description of this structure) and are given a *random* negative charge. The trigonal dodecahedron is one of the most common coordination polyhedra for CN=8; in fact, the coordination of Dy^{3+} in the Dy_3 molecule (Fig. 5.1) can be regarded as a distorted trigonal dodecahedron.

B. The point charges are given equal negative charge but are allowed to take *random* positions on the sphere of radius a.

C. The same as B, but the point charges are not allowed to approach each other closer than $a/2$. This reflects more the situation in a real complex, in which atoms in the coordination sphere repel each other.

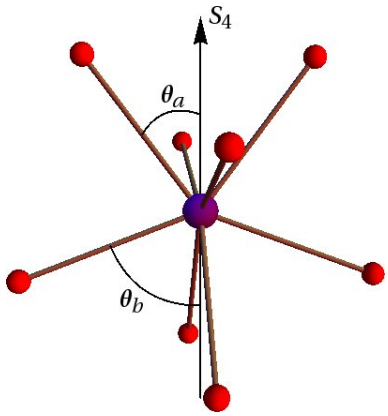

Figure 5.5: Trigonal dodecahedron (point group D_{2d}) used in calculation A. $\theta_a = 36.9°$, $\theta_b = 69.5°$ [15].

The crystal field potential is given by Eqs. (5.1.1) and (5.1.2). We use the complete, correct potential, that is, including fourth- and sixth-order harmonics, but, as remarked in the introduction, the second-order harmonics in general dominate the potential (using the values of $\langle r^k \rangle$ in Table 5.3 and $a = 5\,a_0$).

To each of the cases A, B, C, corresponds a probability distribution of crystal field spectra, which we estimate from calculations on a sample of $N = 10000$ random points, for each case and for Dy^{3+} and Er^{3+}. We consider in each case the principal g factors of the ground Kramers doublet, arranged in decreasing order $g_1 > g_2 > g_3$. Some results are collected in Table 5.5. The g factors are divided by the Landé factor g_J to make comparison between Dy^{3+} and Er^{3+} possible.

The table has to be read as follows: the probability that g_1/g_J of Dy^{3+} in case A is higher than 14.0 is 97.7%, with an uncertainty of 0.2%. The uncertainty is the standard deviation of the sample probability, given by $s = \sqrt{\bar{p}(1-\bar{p})/N}$, where $\bar{p}$ is the sample probability, 0.977 in the example.

The extent to wich g_1/g_J approaches 15 measures the extent to which the Kramers doublet approaches the cylindrical doublet of maximum projection $|M_J| = 15/2$, while the smallness of g_2/g_J is a measure for the uniaxiality of the Kramers doublet. The two are seen to be correlated: a higher probability for g_1/g_J to be large is accompanied by a higher probability for g_2/g_J to be small.

Apart from some small differences between A, B, and C, the lowest Kramers doublet of Dy^{3+} and Er^{3+} in an arbitrary unsymmetrical crystal field has a high probability to be uniaxial and close to $|M_J| = 15/2$. The probabilities for

Table 5.5: Selected probabilities (in %) on the g factors of the lowest Kramers doublet. Note that $(g_1/g_J)_{\max} = 15$.

	A		B		C	
g_1/g_J	Dy^{3+}	Er^{3+}	Dy^{3+}	Er^{3+}	Dy^{3+}	Er^{3+}
> 14.0	97.7(2)	93.4(2)	98.6(1)	96.5(2)	98.2(1)	97.2(2)
> 14.5	93.6(2)	84.8(4)	95.5(2)	89.3(3)	93.9(2)	91.8(3)
> 14.9	61.5(5)	44.0(5)	68.7(5)	46.4(5)	61.9(5)	52.2(5)
g_2/g_J						
< 0.1	92.6(3)	84.5(4)	94.7(2)	87.5(3)	92.9(3)	90.4(3)
< 0.01	79.9(4)	64.6(5)	84.7(4)	68.2(5)	81.1(4)	73.3(4)
< 0.001	60.8(5)	38.4(5)	69.5(5)	42.4(5)	62.8(5)	47.3(5)
< 0.0001	39.0(5)	13.4(3)	50.3(5)	16.3(4)	41.7(5)	18.0(4)

Er^{3+} are systematically lower than for Dy^{3+} but the differences are small.

5.4 Conclusion

The simple point charge model provides some clear evidence for the remarkable result that the ground state Kramers doublet of Dy^{3+} or Er^{3+} can be uniaxially anisotropic in a ligand environment without any axial symmetry. This result was first found in the course of *ab initio* calculations on several Dy^{3+}-containing complexes, synthesized in view of their single-molecule magnetic behavior. The possibility to block magnetic relaxation at decreased temperatures is supposed to be favored by a highly uniaxially anisotropic ground state. The present results suggest that Er^{3+} may be as useful as Dy^{3+} in this respect.

5.A Tables

Table 5.6: Overview of relevant properties of the ground-state J level of trivalent lanthanide ions. n is the number of electrons in the $4f$ shell. Note that $J = L - S$ for $n < 7$ and $J = L + S$ for $n \geq 7$.

	n	L	S	J	g_J	$g_J J$
Ce^{3+}	1	3	$\frac{1}{2}$	$\frac{5}{2}$	$\frac{6}{7}$	2.14
Pr^{3+}	2	5	1	4	$\frac{4}{5}$	3.20
Nd^{3+}	3	6	$\frac{3}{2}$	$\frac{9}{2}$	$\frac{8}{11}$	3.27
Pm^{3+}	4	6	2	4	$\frac{3}{5}$	2.40
Sm^{3+}	5	5	$\frac{5}{2}$	$\frac{5}{2}$	$\frac{2}{7}$	0.71
Eu^{3+}	6	3	3	0	–	–
Gd^{3+}	7	0	$\frac{7}{2}$	$\frac{7}{2}$	2	7
Tb^{3+}	8	3	3	6	$\frac{3}{2}$	9
Dy^{3+}	9	5	$\frac{5}{2}$	$\frac{15}{2}$	$\frac{4}{3}$	10
Ho^{3+}	10	6	2	8	$\frac{5}{4}$	10
Er^{3+}	11	6	$\frac{3}{2}$	$\frac{15}{2}$	$\frac{6}{5}$	9
Tm^{3+}	12	5	1	6	$\frac{7}{6}$	7
Yb^{3+}	13	3	$\frac{1}{2}$	$\frac{7}{2}$	$\frac{8}{7}$	4

Table 5.7: Reduced matrix elements (in the Clebsch-Gordan scheme) of $C^{(k)}$ in the ground-state J level of trivalent lanthanides. L, S, and J values are given in Table 5.6.

	$\langle LSJ\|\|C^{(k)}\|\|LSJ\rangle$					
	Exact			Numerical		
	$k=2$	4	6	$k=2$	4	6
Ce^{3+}	$-2\sqrt{\frac{2}{35}}$	$\sqrt{\frac{2}{21}}$	0	−0.48	0.31	0
Pr^{3+}	$-\frac{52}{45}\sqrt{\frac{7}{55}}$	$-\frac{2}{33}\sqrt{\frac{182}{11}}$	$\frac{136}{99}\sqrt{\frac{5}{143}}$	−0.41	−0.25	0.26
Nd^{3+}	$-\frac{7}{11}\sqrt{\frac{2}{33}}$	$-\frac{476}{363}\sqrt{\frac{2}{143}}$	$-\frac{8075}{1573}\sqrt{\frac{2}{429}}$	−0.16	−0.16	−0.35
Pm^{3+}	$\frac{14}{33}\sqrt{\frac{7}{55}}$	$\frac{476}{1089}\sqrt{\frac{14}{143}}$	$\frac{6460}{4719}\sqrt{\frac{5}{143}}$	0.15	0.14	0.26
Sm^{3+}	$\frac{13}{9}\sqrt{\frac{2}{35}}$	$\frac{13}{33}\sqrt{\frac{2}{21}}$	0	0.35	0.12	0
Eu^{3+}	0	0	0			
Gd^{3+}	0	0	0			
Tb^{3+}	$-\frac{1}{3}\sqrt{\frac{35}{22}}$	$\frac{2}{33}\sqrt{\frac{119}{11}}$	$-\frac{5}{429}\sqrt{\frac{323}{11}}$	−0.42	0.20	−0.06
Dy^{3+}	$-\sqrt{\frac{17}{105}}$	$-\frac{4}{33}\sqrt{\frac{323}{91}}$	$\frac{5}{143}\sqrt{\frac{1615}{39}}$	−0.40	−0.23	0.23
Ho^{3+}	$-\frac{1}{5}\sqrt{\frac{19}{30}}$	$-\frac{3}{22}\sqrt{\frac{19}{13}}$	$-\frac{25}{143}\sqrt{\frac{437}{78}}$	−0.16	−0.16	−0.41
Er^{3+}	$\frac{2}{5}\sqrt{\frac{17}{105}}$	$\frac{1}{11}\sqrt{\frac{323}{91}}$	$\frac{10}{143}\sqrt{\frac{1615}{39}}$	0.16	0.17	0.45
Tm^{3+}	$\frac{1}{3}\sqrt{\frac{35}{22}}$	$\frac{8}{99}\sqrt{\frac{119}{11}}$	$-\frac{25}{429}\sqrt{\frac{323}{11}}$	0.42	0.27	−0.32
Yb^{3+}	$\sqrt{\frac{5}{21}}$	$-\frac{3}{\sqrt{77}}$	$\frac{5}{\sqrt{429}}$	0.49	−0.34	0.24

Bibliography

[1] R. Sessoli and A. K. Powell, Coord. Chem. Rev. **253**, 2328 (2009)

[2] N. Ishikawa, M. Sugita, T. Ishikawa, S.-Y. Koshihara, and Y. Kaizu, J. Phys. Chem. B **108**, 11265 (2004)

[3] D. Gatteschi, R. Sessoli, and J. Villain, *Molecular Nanomagnets* (Oxford University Press, Oxford, 2006)

[4] S. Sugano, Y. Tanabe, and H. Kamimura, *Multiplets of Transition-Metal Ions in Crystals*, Pure and Applied Physics, Vol. 33 (Academic Press, New York and London, 1970)

[5] N. Ishikawa, M. Sugita, T. Okubo, N. Tanaka, T. Iino, and Y. Kaizu, Inorg. Chem. **42**, 2440 (2003)

[6] L. F. Chibotaru, L. Ungur, and A. Soncini, Angew. Chem. **47**, 4126 (2008)

[7] L. Ungur, W. Van den Heuvel, and L. F. Chibotaru, New J. Chem. **33**, 1224 (2009)

[8] D. Visinescu, A. M. Madalan, M. Andruh, C. Duhayon, J.-P. Sutter, L. Ungur, W. Van den Heuvel, and L. F. Chibotaru, Chem. Eur. J. **15**, 11808 (2009)

[9] K. Bernot, J. Luzon, L. Bogani, M. Etienne, C. Sangregorio, M. Shanmugam, A. Caneschi, R. Sessoli, and D. Gatteschi, J. Am. Chem. Soc. **131**, 5573 (2009)

[10] C. Görller-Walrand and K. Binnemans, in *Handbook on the Physics and Chemistry of Rare Earths*, Vol. 23, edited by K. A. Gschneidner, Jr. and L. Eyring (Elsevier Science B.V., Amsterdam, 1996) Chap. 155, p. 121

[11] D. A. Varshalovich, A. N. Moskalev, and V. K. Khersonskii, *Quantum Theory of Angular Momentum* (World Scientific Publishing, Singapore, 1989)

[12] A. J. Freeman and R. E. Watson, Phys. Rev. **127**, 2058 (1962)

[13] A. Abragam and B. Bleany, *Electron Paramagnetic Resonance of Transition Ions* (Clarendon Press, Oxford, 1970)

[14] M. Gerloch and R. F. McMeeking, J. Chem. Soc. Dalton Trans. , 2443 (1975)

[15] J. K. Burdett, R. Hoffmann, and R. C. Fay, Inorg. Chem. **17**, 2553 (1978)

Chapter 6

Ultralow blocking temperature and breakdown of the giant spin model in Er^{3+}-doped nanoparticles

Abstract The magnetization of luminescent Er^{3+}-doped PbF_2 nanoparticles (formula $Er_{0.3}Pb_{0.7}F_{2.3}$) has been studied. Despite of the high concentration of the doping Er^{3+} ions and relatively large size (8 nm) of these nanoparticles we have found no deviation between field-cooled (FC) and zero-field-cooled (ZFC) magnetization curves down to $T = 0.35\,\mathrm{K}$, which points out an ultralow blocking temperature for the reversal of magnetization. We also have found strongly deviating magnetization curves $M(H/T)$ for different temperatures T. These results altogether show that the investigated nanoparticles are not superparamagnetic, but rather each Er^{3+} ion in these nanoparticles is found in a paramagnetic state down to very low temperatures, which implies the breakdown of the Néel-Brown giant spin model in the case of these nanoparticles. Calculations of magnetization within a paramagnetic model of non-interacting Er^{3+} ions support this conclusion. Due to the ultralow blocking temperature, these nanoparticles have a potential for magnetic-field-induced nano-scale refrigeration with possibility of optical localization and temperature control.

W. Van den Heuvel, V. K. Tikhomirov, D. Kirilenko, N. Schildermans, L. F. Chibotaru, J. Vanacken, P. Gredin, M. Mortier, G. van Tendeloo, and V. V. Moshchalkov, submitted to Phys. Rev. B. W. V.d.H. is responsible for the theoretical part of this work, Section 6.4.

6.1 Introduction

The physics of magnetic nanoparticles is an active field of research for already a few decades due to new magnetic properties which arise at the nanoscale and to numerous applications [1]. One of the central demands in these applications is the fabrication of nanoparticles with a narrow size distribution and their arrangement in two- and three-dimensional lattices with controllable interparticle spacing, which was recently achieved by new synthetic approaches and self-assembly [2–5]. For the storage applications, it is desirable to have nanoparticles with large anisotropy energy while keeping their volume small [6]. Magnetic nanoparticles have been attracting recently a substantial interest also for hyperthermal treatment of cancer cells, nuclear-magnetic-resonance imaging and nanolabeling [7, 8], as well as for site-specific drug delivery and manipulating cell membranes [9, 10]. A great potential for future applications of nanoparticles is related to magnetic-field-induced refrigeration based on the magneto-caloric effect, which is considered as an alternative to a traditional vapor-cycle refrigeration [11–13]. Here rare-earth intermetallic compounds have been considered as most promising for magnetic refrigeration due to the large magnetic moments in the ground state of their rare-earth components, such as Gd, Er, Ho, Dy [11, 13]. Those intermetallic compounds are not transparent though, therefore the luminescence properties of their rare-earth component cannot be used. As yet, magnetic refrigeration has been explored only at the macro-scale, while a refrigeration of nano-volumes still has not been attained.

In this article we investigate the magnetization of luminescent Er^{3+}-doped PbF_2 nanoparticles, formula $Er_{0.3}Pb_{0.7}F_{2.3}$. The nanoparticles were either embedded in bulk glass-ceramics host or extracted from this host to form free-standing nanopowder according to procedure [14], as described further in the Experimental section. We find that, in both cases, despite high concentration of the doping Er^{3+} ions and relatively large size (8 nm) of these nanoparticles, they show *no blocking temperature* down to $T = 0.35\,\mathrm{K}$ as proved by field-cooled (FC) and zero-field-cooled (ZFC) magnetization experiments down to $T = 0.35\,\mathrm{K}$. Moreover, the magnetization curves, when drawn as function of the ratio of applied magnetic field and temperature, H/T, strongly deviate from each other, resembling an anisotropic superparamagnetic behavior [1]. These facts enforced us to conclude that the Néel-Brown model [15, 16], based on the concept of giant (total) spin and successfully used for other nanoparticles, cannot be applied to the investigated Er^{3+}-doped nanoparticles, which are therefore rather paramagnetic than superparamagnetic. We also performed simulations of measured magnetization and susceptibility within a model of non-interacting Er^{3+} ions which support this conclusion.

An implication of our findings is that the earlier known transparent and luminescent Er^{3+}-doped PbF_2 nanoparticles [14] may also be used for nano-scale

refrigeration, in particular, at temperatures below 1 K, due to high magnetic moment in the ground state of the Er^{3+} and the absence of the blocking temperature down to at least 0.35 K. Luminescent nanoparticles also have proven to be useful as optical nanolabels [7], nanoheaters [17] and nanosensors of magnetic field [18]. Hence, the here proposed combination of magnetic and luminescent properties in one nanoparticle $Er_{0.3}Pb_{0.7}F_{2.3}$ would be of advantage.

6.2 Experimental

First, the bulk oxyfluoride Er^{3+}-doped nano-scaled glass-ceramics (NGC)

$$32(SiO_2)9(AlO_{1.5})31.5(CdF_2)18.5(PbF_2)5.5(ZnF_2) : 3.5(ErF_3),$$

mol%, has been prepared as described in [19]. The Er^{3+} ions nucleate the growth of PbF_2-based crystalline nanoparticles in this NGC on heat-treatment and therefore up to 100% of Er^{3+} ions are incorporated into these nanoparticles ([14, 17, 18] and refs therein). Further, the nanoparticles have been extracted from the NGC by means of chemical etching as described in Ref. [14].

The transmission electron microscope (TEM) images of the nanoparticles/powder are presented in Figs. 6.1(a,b,c); they show that the nanoparticles are spherical and homogeneous in diameter, which is about 8 nm. The electron diffraction pattern and transmission electron microscope energy dispersive X-ray spectroscopy (TEM EDX) of the nanoparticles/powder are shown in Fig. 6.1(d) and Fig. 6.1(e), respectively. The diffraction pattern in Fig. 6.1(d) indicates that the structure of the nanoparticles is a face centered cubic (fcc) structure of the classic substituted fluorite (or β-PbF_2 [19]), which is known to be in case of Er^{3+}-doping the $Er_xPb_{1-x}F_{2+x}$, where $x = 0.29$, or approximately $Er_{0.3}Pb_{0.7}F_{2.3}$ ([20, 21] and refs therein). The lattice parameter of the nanoparticles, Fig. 6.1(d), is slightly shorter than in β-PbF_2 due to smaller ionic radii of Er^{3+} ions compared to Pb^{2+}, as argued in [19].

When doing the TEM EDX experiments, Fig. 6.1(e), we have noted that the fluorine ions tend to move away from the area irradiated by the electron beam due to high superionic conductivity of the β-PbF_2 [21] and the negative charge of the electron beam. Therefore, the proportion of Er^{3+} and Pb^{2+} ions can be certainly found in TEM EDX experiments, while the proportion of registered F^- ions slightly depends on the parameters of the electron beam. As we have not found in EDX spectra any substantial admixtures of other ions apart from Er^{3+}, Pb^{2+} and F^-, (Fig. 6.1(e)), the proportion of F^- ions was estimated exactly by charge compensation, which corresponds to the classic substituted fluorite $Er_xPb_{1-x}F_{2+x}$, where $x = 0.29$, or approximately to $Er_{0.3}Pb_{0.7}F_{2.3}$.

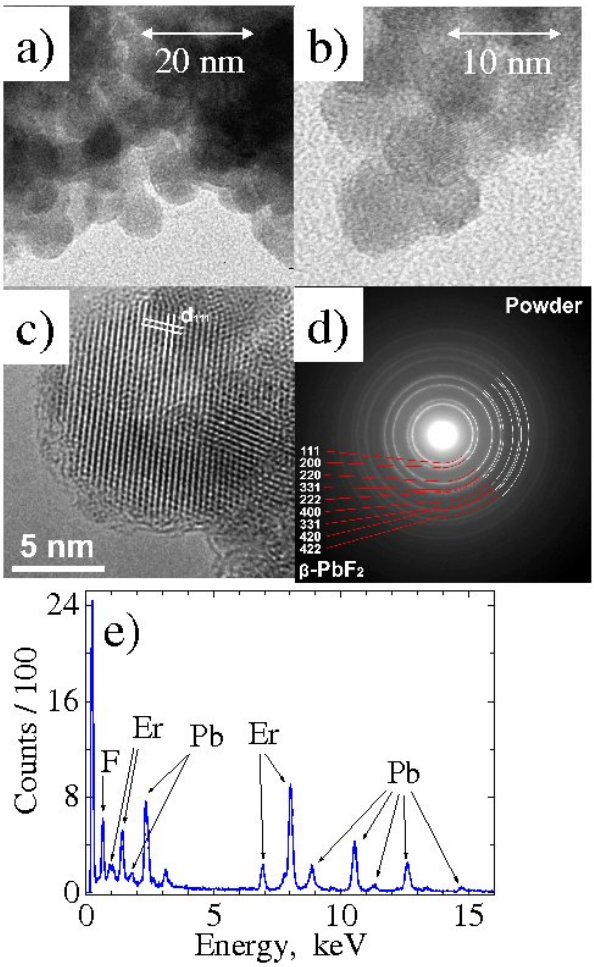

Figure 6.1: (a,b) TEM images of nanoparticles with different spatial resolution. Black round spots of about 8 nm diameter are the nanoparticles comprising the aggregates/nanopowder. (c) TEM image of single nanoparticle, where crystalline planes (1,1,1) of β-PbF_2 are indicated as d111. (d) Electron diffraction pattern taken from nanopowder, where the diffraction rings from certain planes of the β-PbF_2 are indicated. (e) TEM EDX spectra taken from the nanopowder; the observed peaks are labeled.

The $Er_xPb_{1-x}F_{2+x}$ is known as a stoichiometric compound of *tveitite* type and rare-earth ions dissolve/disperse in this compound without clustering, The high luminescence yield in these nanoparticles [22] proves high solubility/dispersion of the Er^{3+} dopants in tveitite structure because the clustering of the dopants could result in the concentration quenching of luminescence. For the measurements of magnetization, a sample of the nanoparticle powder was aggregated in a small cylinder pellet about 2 mm diameter and 2 mm height. The bulk NGC samples of about 40 mg were chipped from the larger pieces of bulk NGC, which weighed up to 10 to 20 gram. The magnetization has been measured with Vibrating Sample Magnetometer (VSM), Superconducting Quantum Interference Device (SQUID) and Hall Probe Magnetometer in the temperature ranges 300 to 1.85 K, 15 to 3.5 K and 1.85 to 0.35 K, respectively, using liquid He^4 and He^3 cooling agents, as appropriate.

6.3 Results

Fig. 6.2 shows the temperature dependence of magnetization M of the nanopowder obtained with VSM (a), SQUID (b) and Hall Probe (c) techniques, in the zero field cooled (ZFC) and field cooled (FC) regimes. Er^{3+} is known as one of the most magnetic ions with magnetic moment of ca. $9\,\mu_B$ in the ground state ($J = 15/2$). These ions are responsible without doubt for the magnetic properties of the investigated nanoparticles. The deviation point in ZFC and FC temperature dependencies would indicate the blocking temperature T_B, below which the magnetic moments of the sample get frozen, i.e. they cannot be thermally or magnetic-field re-oriented [23–25]. However, the ZFC and FC curves were coincident in the whole temperature range, from 300 down to 0.35 K, Figs. 6.2(a,b,c), at any applied constant magnetic field H. This points out the absence of blocking temperature down to 0.35 K, the lowest temperature which can be achieved with our He^3 cryostat. This means that the magnetic moments of Er^{3+} in these nanoparticles still can be re-oriented, either thermally or by applying an external magnetic field, even at very low temperatures. Then the magneto-caloric effect and the magnetic-field-induced cooling of the nanoparticles should be allowed down to temperatures as low as 0.35 K. The same result has been obtained for the bulk NGC samples with the magnitude of magnetization of about twice lower than in the nanopowder, because in the NGC the nanoparticles comprise only about half of the total mass of the sample [14, 22].

To attempt an attribution of the magnetic behavior shown in Fig. 6.2 to some known type of magnetism we have plotted in Fig. 6.3 the experimental temperature dependence of $1/\chi$, where χ is the low-field Van Vleck magnetic susceptibility. The same result has been obtained for the bulk NGC samples and

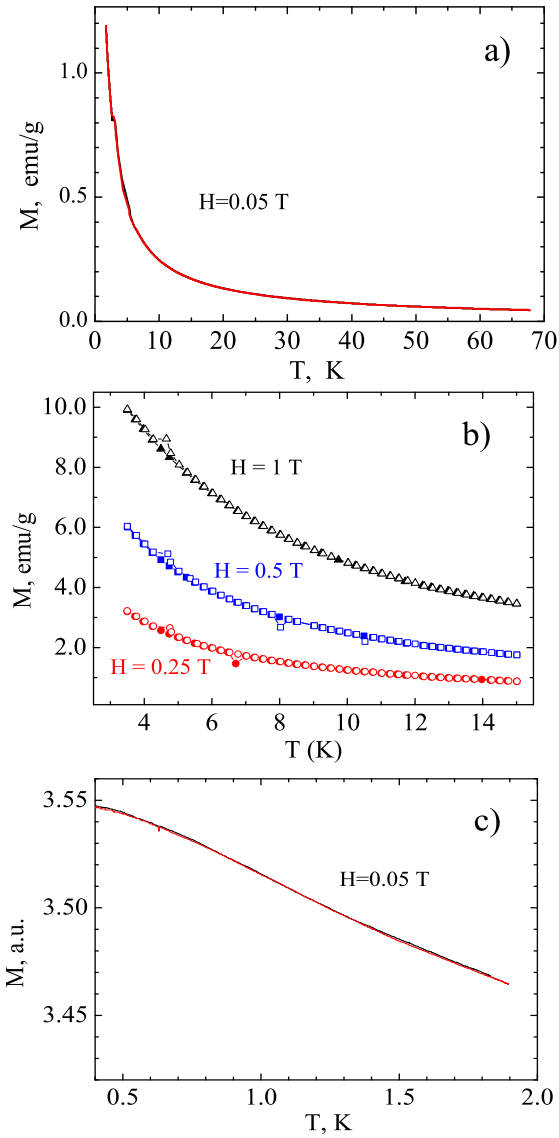

Figure 6.2: Temperature dependence of magnetization M in $Er_{0.3}Pb_{0.7}F_{2.3}$ nanopowder at indicated external magnetic fields. Measurements have been done using the VSM (a), SQUID (b) and Hall probe (c) set-ups. The dependences for zero-field-cooled (ZFC) and field-cooled (FC) regimes were coincident at all applied external fields H.

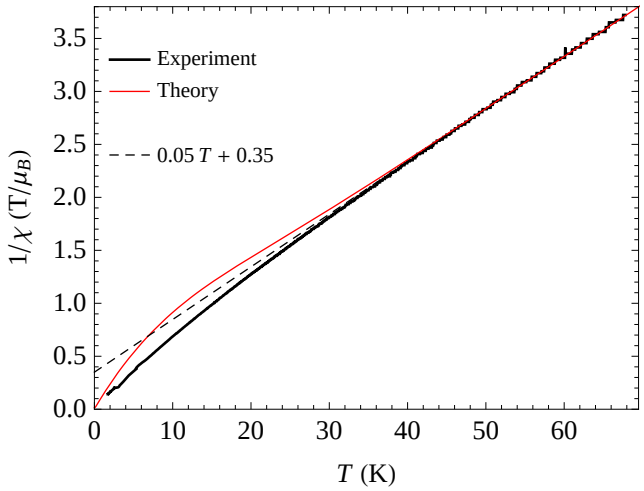

Figure 6.3: Experimental and theoretical temperature dependences of the inverse magnetic susceptibility in $Er_{0.3}Pb_{0.7}F_{2.3}$ nanopowder normalized per Er^{3+} ion and determined from the magnetization at 0.05 T. The experimental dependence $1/\chi$ has been divided by a factor of 2.0, as discussed further in the text. Crystal field parameters for the theoretical curve were taken at $x = -0.375$ and $W = 0.959\,\mathrm{cm}^{-1}$.

therefore it is not shown here. As seen in Fig. 6.3, the behavior of the inverse susceptibility cannot be attributed to any basic type of magnetic ordering. Indeed, the intercept of $1/\chi$ seems to be at the origin of coordinates, as follows from an extrapolation of the low temperature part of the curve from the lowest measured point at 1.85 K. To be noted, for ferro and ferri type of ordering the intercept should lie on the T axis, while for antiferro ordering and spin glass phase it should be on the $1/\chi$ axis [26]. Hence the dependence in Fig. 6.3 points to a paramagnetic behavior of the nanoparticles. However this paramagnetism is rather unconventional since $1/\chi$ does not extrapolate to zero from the high temperature region, as Fig. 6.3 clearly shows. This strongly differs, for instance, from the magnetism of $Fe_{1-x}C_x$ nanoparticles, for which perfect superparamagnetism was achieved (straight $1/\chi$ lines extrapolated to zero from high temperature region), either by dilution or by reducing the size of nanoparticles to 3.8 nm [24]. The origin of unconventional paramagnetism seen in Fig. 6.3 will be elucidated in the next section.

Fig. 6.4 shows experimental magnetization curves M vs H (a) and M vs H/T (b) of the nanopowder at the indicated temperatures, and similar results have been obtained for the bulk NGC, again with about twice lower values due to the magnetic non-active glass host component embedding the $Er_{0.3}Pb_{0.7}F_{2.3}$

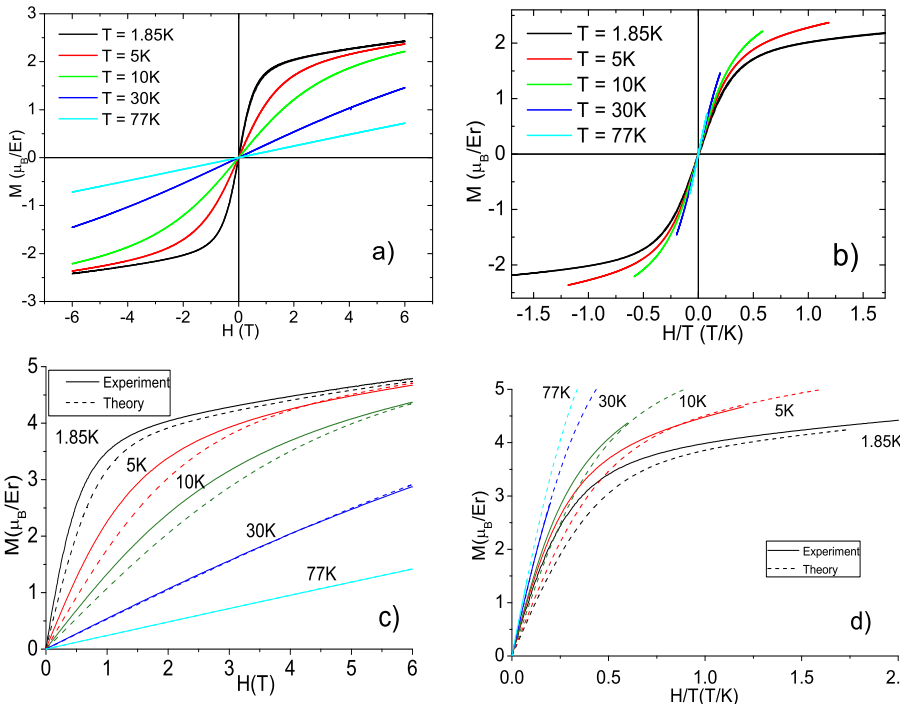

Figure 6.4: (a,b) The experimental field dependence of the magnetization in $Er_{0.3}Pb_{0.7}F_{2.3}$ nanopowder, normalized per Er^{3+} ion. (c,d) The theoretical and experimental field dependences of the magnetization; the experimental dependences have been multiplied by factor of 2.0 for comparison of experimental and theoretical data, as in Fig. 6.3. The theoretical magnetization is given for a field parallel to the cubic C_4 axis. Crystal field parameters are the same as in Fig. 6.3.

nanocrystals. For both nanopowder and bulk NGC materials, the $M(H)$ curves show no hysteresis, i.e. the coercive field is zero, and the magnetization does not reach saturation, even for fields up to 10 Tesla (not shown here).

The experimental field dependences of magnetization of investigated nanoparticles (Fig. 6.4(a)) are typical for superparamagnetic single-domain magnetic nanoparticles [23–25]. The same curves drawn as function of the ratio H/T (Fig. 6.4(b)) do not superimpose on each other, pointing out an important contribution of magnetic anisotropy. Indeed, in the absence of this contribution the magnetization is described either by Brillouin function [27] or Langevin function [26], both depending on H/T; therefore, the functions $M(H/T)$ considered for different fixed values of T would lie on the same curve. The behavior

of magnetization similar to the one shown in Fig. 6.4(b) was observed in many nanoparticles, e.g., in $CoPt_3$ [28], and is called anisotropic superparamagnetism [1, 28]. In these nanoparticles the theoretical magnetization curves can be brought into perfect accord with experiment by taking into account the finite anisotropy energy E_A of the total magnetization of the nanoparticle [28]. However, this scenario cannot be applied to the nanoparticles investigated here for the following reasons. In conventional nanoparticles the magnetization is well described within the Néel-Brown giant spin model [15, 16], i.e. by considering only the dynamics of the total spin (magnetization) of the nanoparticle. Within this model, the anisotropy energy (the difference of the energy of the giant spin aligned along and perpendicular to the anisotropy axis of the nanoparticle), usually of axial type, is equalized to the energy of the barrier for the reversal of magnetization of the nanoparticle, E_B [15]. Now since the blocking temperature for reversal of magnetization T_B is proportional to E_B (and E_A), large deviations of magnetization curves from the prediction of the free magnetic moment model (described by the Langevin function) should be accompanied by large values of T_B. This is indeed the case for conventional nanoparticles, e.g., of $CoPt_3$, where deviations of magnetization from the Langevin function were observed down to $T = 150\,K$, and $T_B = 37.5\,K$ was found for nanoparticles of 6 nm size [28]. By contrast, in our case the deviations of magnetization from the predictions of free magnetic moment model are of the same extent, while the blocking temperature is practically zero. Thus the physics underlying the observed magnetization curves (Fig. 6.4(b)) is totally different.

The above analysis shows that the magnetization of nanoparticles studied here cannot be described within the giant spin model since it cannot conciliate the strongly deviating magnetization curves in Fig. 6.4(b) with negligible T_B as concluded from Fig. 6.2(c). This means that the magnetism of our Er^{3+}-doped nanoparticles should be better described by a collection of magnetic moments of Er^{3+} ions which fluctuate independently from each other down to very low temperatures. The exchange interaction between neighbor erbium ions is not excluded of course but it is expected to be weak, given the negligible T_B in these relatively large (8 nm) nanoparticles, with high concentration of Er_3^+ ions. Therefore as a starting model for the description of the observed magnetic properties we consider in the next section non-interacting Er^{3+} ions.

6.4 Model and simulations

As we already mentioned, at high temperatures the measured inverse susceptibility is a straight line with positive intercept on the vertical axis, resembling a Curie-Weiss behavior, Fig. 6.3, while at lower temperatures, the curve bends away from the straight line and clearly approaches zero susceptibility at 0 K,

indicating a paramagnetic ground state. This behavior can be understood from the crystal field splitting of the $^4I_{15/2}$ ground state of a single Er^{3+} ion [29]. Crystal field splitting in lanthanides is usually of the order of magnitude of 100 K, comparable with the temperature scale of the measurements. Therefore, *thermal population* or depopulation of the crystal field levels determines the temperature dependence of magnetic properties. The bending in the susceptibility curve is associated with the transition from a state where only the ground Kramers doublet is occupied to a state where both the ground and the first excited Kramers doublet(s) are occupied. This is accompanied by an increase of the average magnetic moment, as indicated by the decreasing slope (i.e. negative curvature) of $1/\chi$ with increasing temperature. We see the same effect in the magnetization versus H/T plots in Fig. 6.4(b). Perfectly coinciding curves are expected for the magnetization of a single Kramers doublet (Brillouin curves). Instead, the magnetization clearly increases with increasing temperature. Finally, the effect of excited Kramers doublets is also seen in the magnetization versus H plot at 1.85 K in Fig. 6.4(a): after early saturation around 1.5 T, the magnetization continues to increase almost linearly with the field. This results from the linear (first order) increase of the magnetic moment of the ground state by interaction with excited Kramers doublets through the Zeeman Hamiltonian.

6.4.1 Crystal field calculations

As seen in Fig. 6.1, the structure of the nanoparticles is face-centered cubic with a lattice parameter corresponding to the β-PbF_2 phase [19]. Therefore, to calculate the magnetic properties we consider the Er^{3+} ion in a cubic crystal field potential created by 8 F^- ions positioned at the vertices of a cube centered on Er^{3+}. Actually this approximation is expected to be rather crude for two reasons. First, local charge compensation by F^- or other anions can distort the cubic coordination environment considerably. Second, the site symmetry can be considered cubic only in the bulk of the PbF_2 crystal. The nanoparticles have such a small size however, that a non-negligible proportion of atoms are located near the surface of the particle. For example, if we assume that atoms belong to the "surface volume" if they are within 1 nm of the surface, we find that, in a spherical nanoparticle of radius 5 nm, as much as 49 % of the atoms is contained in the surface volume (assuming that the number of atoms per volume is constant over the nanoparticle). Er^{3+} ions near the surface will experience a deviation from the bulk cubic field. The strength and form of this perturbation are not known and we carry the calculation through in the assumption of perfect and uniform cubic field potential. At least at high temperatures, we expect the perturbations to be of less importance.

The calculation is based on the atomic $^4I_{15/2}$ level, without consideration of

any higher levels. The Stark levels are classified by irreducible representations $\Gamma_7 + 3\Gamma_8 + \Gamma_6$ [30]. The cubic field is described by two parameters x and W, defined in Refs. [31,32]. The parameter x determines the relative contributions of the fourth- and sixth-order angular momentum operators to the crystal field Hamiltonian, while the parameter W determines the energy scale of the crystal field interaction. In Ref. [33], the following values where determined for Er^{3+} centers in a PbF_2 crystal with nonlocal charge compensation: $x = -0.375$ and $W = 1.49\,\mathrm{cm}^{-1}$. We take these as starting values, keeping in mind that they may be adjusted to fit the experimental results. These parameters place the Γ_7 as ground state and an accidentally degenerate Γ_6, Γ_8 pair $80\,\mathrm{cm}^{-1}$ higher [31]. The Landé g factor for the ground atomic multiplet $J = 15/2$ equals $6/5$ [32].

6.4.2 Simulation of magnetic properties

We have modelled the experimental magnetization curves of Fig 6.4 assuming the magnetization occurs along the major crystalline axes, such as C_4 and C_3 axes (Fig. 6.4(c,d)), and found that the theoretical curves for these directions deviate less than 5% from each other. Since the nanoparticles are randomly oriented with respect to the direction of the applied magnetic field, an average over all different crystalline orientations has to be taken into account but the difference in magnetization along different axes shows that such an averaging is actually unnecessary. To obtain a quantitative correspondence with the experiment, it was necessary to scale the latter: the experimental magnetization and susceptibility, normalized to one Er^{3+} ion using the sample mass and the formula $Er_{0.3}Pb_{0.7}F_{2.3}$, were calculated to be smaller than the theoretical predictions. It is possible to determine the scaling factor from the experimental results. There are two experimentally accessible properties that are independent of the crystal field parameters. The first is the slope of $1/\chi$ in the high-temperature limit. The second is the magnetic moment of the Γ_7 ground doublet, given by the intercept of the magnetization with the M axis, in the zero-temperature limit. The first is crystal-field-independent because the splitting of the energy levels is irrelevant at temperatures higher than this splitting. The second is crystal-field-independent because Γ_7 occurs only once in the cubic reduction: $J = 15/2 \to \Gamma_6 + \Gamma_7 + 3\Gamma_8$. The Γ_7 wavefunction is thus completely defined by symmetry; its magnetic moment is $m(\Gamma_7) = 3.4\,\mu_\mathrm{B}$ [32]. Of course this is only valid insofar as the symmetry is exactly cubic. In the present case the principle of magnetic moment is not very useful to derive the scaling factor. As seen in Fig. 6.4(b), a reliable intercept cannot be derived from the 1.85 K curve, as there is some curvature in the higher field region. Clearly still lower temperatures would be needed for this. Furthermore, we have mentioned before that deviations from cubic symmetry are expected. We will therefore derive the scaling factor from the susceptibility. The slope of $1/\chi$ is

given by the Curie formula, applied to the $^4I_{15/2}$ multiplet:

$$\frac{1}{\chi} = \frac{3k}{\mu_B g^2 J(J+1)} T = 0.0487\,T,$$

where χ is in units of μ_B per Tesla. The measured $1/\chi$ approaches linearity from about 45 K, with a slope of $\approx 0.099\,\mathrm{T}/(\mu_B\mathrm{K})$. Together with the previous equation, this yields a scaling factor of $0.099/0.0487 \approx 2.0$. With the slope fixed by the scaling factor, the high-temperature part of $1/\chi$ is made to coincide with the theoretical one by adjusting the crystal field parameters. The x parameter was kept constant at -0.375 while the W parameter was lowered to $0.959\,\mathrm{cm}^{-1}$. In principle, the x parameter could be adjusted to further refine the correspondence. We found however no improvement doing this and x was kept to the value reported in Ref. [33].

Fig. 6.4 shows the theoretical magnetization curves for a single Er^{3+} ion within the above model, compared with the experimental measurements on the nanoparticles. The magnetization curves in Fig. 6.4 were calculated for a field parallel with a cubic C_4 axis. As the reported measurements were done on powder samples, the calculated magnetization should be averaged over all directions of the field. For fields lower than 6 T however, the dependence of magnetization on field direction is negligible for our purposes and therefore ignored. Note that while the scaling factor and the W parameter were determined from the susceptibility measurement alone, the agreement with the magnetization curves is satisfactory as well, and can be seen as an independent confirmation of the model.

There are still discrepancies between theory and experiment in the low temperature region that could not be eliminated within the cubic crystal field model applied here. This is not unexpected in view of the reservations we made concerning the validity of the approximation in the nanoparticles, as discussed above. The large reduction of the W parameter, from $1.49\,\mathrm{cm}^{-1}$ in Ref. [33] to $0.995\,\mathrm{cm}^{-1}$ here, should probably also be regarded as an indication of the deviation from uniform, cubic potential that the Er^{3+} ions experience in the nanoparticles.

6.5 Discussion and conclusions

We have studied the magnetic properties of luminescent Er^{3+}-doped PbF_2 nanoparticles when embedded in glass-ceramics host and when extracted from this host. Our main finding is the ultralow value of blocking temperature of reversal of magnetization in these nanoparticles, for which the upper limit was estimated to be at 0.35 K. This is the more surprising as the nanoparticles

have relatively large diameters and high concentration of erbium ions. In combination with other observed magnetic properties, Figs. 6.3 and 6.4(b), this result implies that the investigated nanoparticles are not superparamagnetic but simply paramagnetic, i.e. described by independent dynamics of individual magnetic moments of Er^{3+} ions. This means the breakdown of the giant spin model in application to Er^{3+}-doped nanoparticles investigated here, which to our knowledge is the first example of this type, not reported for previously investigated nanoparticles.

One of the consequences of the independent-local-moments model is that the shape anisotropy of the nanoparticle, which is the main source of magnetic anisotropy in conventional nanoparticles [15], does not play a role here. By contrast in the present model the main contribution to the deviation of magnetization curves from conventional ones is given by the spin-orbit coupling on the Er^{3+} sites. The observed unconventional behavior of magnetization and susceptibility is not related to the anisotropy which might be induced by the spin-orbit coupling on the metal sites but only to the fact that due to the latter the spins of the metal ions are not good quantum numbers anymore (and therefore different levels of the Er^{3+} ion have strongly differing magnetic moments). For instance, in the simplified model considered here the local magnetic moments on the Er^{3+} sites are perfectly isotropic (no easy axes of magnetization) due to the supposed cubic symmetry of the Er^{3+} environment. Note that the independent-local-moments model is fully consistent with the observed very low value of T_B because there is no blockage of magnetization in a system of non-interacting magnetic ions.

The proposed paramagnetic interpretation of measured magnetic properties has been supported by simulations done within the model of magnetically non-interacting Er^{3+} ions, with a further simplification that the erbium ions resided in perfectly cubic sites. Despite the fact that such a crystal field model is not supported by recent luminescence experiments for the investigated nanoparticles [19, 29], it allows to reproduce all qualitative features of the measured magnetic properties (Figs. 6.3 and 6.4). In order to obtain a better agreement with experiment the determination of the actual structure of the nearest environment of Er^{3+} ions in the investigated nanoparticles is indispensable. This task can be accomplished by using neutron scattering techniques and such a work is planned by our group for the near future. Besides allowing a further elucidation of magnetism, this knowledge is needed also for the clarification of the mechanism of extraordinary suppression of green luminescence of these nanoparticles in strong applied field [34].

Interestingly, lanthanides doped in different metals have shown pretty high blocking temperatures at much lower concentrations [35]. For instance, single-crystals of Y doped with only 5% of erbium ions show $T_B = 5.6\,K$ [35]. The large difference in the value of the blocking temperature from the present case is

probably explained by the fact that in our case Er^{3+} is doped into the insulating PbF_2 host, which does not transmit efficiently the exchange interaction between erbium ions, in contrast to the metallic Y host.

As one possible application, the ultralow blocking temperature exhibited by the Er^{3+}-doped nanoparticles may be used for magnetic refrigeration in nanovolumes to temperatures lower than 0.35 K.

Bibliography

[1] S. Bedanta and W. Kleemann, J. Phys. D: Appl. Phys. **42**, 013001 (2009)

[2] S. Sun, C. B. Murray, D. Weller, L. Folks, and A. Moser, Science **287**, 1989 (2000)

[3] V. F. Puntes, K. M. Krishnan, and A. P. Alivisatos, Science **291**, 2115 (2001)

[4] E. V. Shevchenko, D. V. Talapin, A. Kronowski, F. Wiekhorst, J. Kötzler, M. Haase, A. L. Rogach, and H. Weller, Adv. Mater. (Weinheim, Ger.) **14**, 287 (2002)

[5] E. V. Shevchenko, D. V. Talapin, A. L. Rogach, A. Kronowski, M. Haase, and H. Weller, J. Am. Chem. Soc. **124**, 11480 (2002)

[6] D. Weller and A. Moser, IEEE Trans. Magn. **35**, 4423 (1999)

[7] X. Gao, Y. Cui, R. M. Levenson, L. W. K. Chung, and S. Nie, Nature Biotechnology **22**, 969 (2004)

[8] S. A. Corr, Y. P. Rakovich, and Y. K. Gun'ko, Nanoscale Research Letters **3**, 87 (2008)

[9] C. C. Berry and A. S. G. Curtis, J. Phys. D: Appl. Phys. **36 R**, 198 (2003)

[10] P. P. Freitas and H. A. Ferreira, in *Handbook of Magnetism and Magnetic Materials, vol. 4: Novel Materials*, edited by H. Kronmüller and S. P. S. Parkin (Wiley, New York, 2007)

[11] K. A. Gschneidner, V. K. Pecharsky, and A. O. Tsokol, Rep. Prog. Phys. **68**, 1479 (2005)

[12] O. Tegus, E. Bruck, K. H. L. Buschow, and F. R. de Broer, Nature **415**, 150 (2002)

[13] C. R. H. Bahl and K. K. Niels, J. Appl. Phys. **105**, 013916 (2009)

[14] M. Mortier and G. Patriarche, Opt. Mater. **28**, 1401 (2006)

[15] L. Néel, C. R. Acad. Sci. Paris **228**, 664 (1949)

[16] W. F. Brown, J. Appl. Phys. **30**, 130S (1959)

[17] V. K. Tikhomirov, K. Driesen, V. Rodriguez, P. Gredin, M. Mortier, and V. V. Moshchalkov, Opt. Express **17**, 11794 (2009)

[18] V. K. Tikhomirov, L. F. Chibotaru, D. Saurel, P. Gredin, M. Mortier, and V. V. Moshchalkov, Nano Letters **9**, 721 (2009)

[19] V. K. Tikhomirov, D. Furniss, I. M. Reaney, M. Beggiora, M. Ferrari, M. Montagna, and R. Rolli, Appl. Phys. Lett. **81**, 1937 (2002)

[20] D. J. M. Bevan, J. Strähle, and O. Greis, J. Solid State Chem. **44**, 75 (1982)

[21] S. Hull, Rep. Prog. Phys. **67**, 1233 (2004)

[22] V. K. Tikhomirov, M. Mortier, P. Gredin, G. Patriarche, C. Görller-Walrand, and V. V. Moshchalkov, Opt. Express **16**, 14544 (2008)

[23] M. F. Hansen and S. Mørup, J. Magn. Magn. Mater. **203**, 214 (1999)

[24] M. F. Hansen, C. Johansson, M. S. Pedersen, and S. Mørup, J. Phys.: Condens. Matter **7**, 9269 (1995)

[25] M. Knobel, W. C. Nunes, L. M. Socolovsky, E. De Biasi, J. M. Vargas, and J. C. Denardin, J. Nanosci. Nanotechnol. **8**, 2836 (2008)

[26] N. W. Ashcroft and N. D. Mermin, *Solid State Physics* (Saunders College, Philadelphia, 1988)

[27] O. Kahn, *Molecular Magnetism* (VCH Publishers, New York, 1993)

[28] F. Wiekhorst, E. Shevchenko, H. Weller, and J. Kötzler, Phys. Rev. B **67**, 224416 (2003)

[29] V. D. Rodríguez, V. K. Tikhomirov, and J. Méndez-Ramos, Europhys. Lett. **69**, 128 (2005)

[30] J. S. Griffith, *The Theory of Transition-Metal Ions* (Cambridge University Press, Cambridge, 1964)

[31] K. R. Lea, M. J. M. Leask, and W. P. Wolf, J. Phys. Chem. Solids **23**, 1381 (1962)

[32] A. Abragam and B. Bleany, *Electron Paramagnetic Resonance of Transition Ions* (Clarendon Press, Oxford, 1970)

[33] I. B. Aizenberg, B. Z. Malkin, and A. L. Stolov, Sov. Phys. Solid State **13**, 2155 (1972)

[34] L. F. Chibotaru, V. K. Tikhomirov, D. Saurel, and V. V. Moshchalkov, J. Appl. Phys. **106**, 053502 (2009)

[35] K. Baberschke, P. Pureur, A. Fert, R. Wendler, and S. Senoussi, Phys. Rev. B **29**, 4999 (1984)

Chapter 7

Conclusions and outlook

In this thesis we have studied several theoretical models relevant for new magnetic molecular materials of high current interest. We have shown that the Anderson superexchange model, widely used nowadays for the rationalization of exchange coupling in magnetic complexes and networks, is not of universal applicability even within the basic exchange model. A clear case when it breaks down corresponds to large intrasite electron repulsion. This seems to be more the case in lanthanides, where the magnetic electrons reside in 4f orbitals of relatively small size, than for transition metal ions for which the model was originally proposed. After a thorough analysis of the origin of this drawback of the Anderson model we have proposed an alternative approach which works perfectly in the entire region of electronic parameters.

Another line of theoretical development concerned the thermodynamics of long (infinite) chains and cycles with several metal ions, in particular, heterometallic chains, with strongly anisotropic metal ions having Ising exchange interactions with their neighbors. The new aspect of this problem, well investigated in the past, is the decorated character of the chains, where beside Ising ions there are also other ions present which couple with each other through Heisenberg (isotropic) exchange interaction. The complex unit cell of the chains is considered together with arbitrary orientation of anisotropy axes on the Ising ions, which generally are not parallel to each other. We were able to cope with both these aspect of the chain by developing a theory based on the transfer matrix approach, which allowed also to treat the thermodynamics of the chain in applied magnetic field arbitrarily oriented with respect to the chain and of arbitrary magnitude. This development was motivated by the fact that many compounds presently designed and considered as most performant as SMMs and SCMs involve lanthanide ions. Moreover, the currently investigated SCMs are often of a decorated heterometallic type, while many of the presently synthesized

SMMs are cyclic molecules with non-parallel anisotropy axes on the strongly anisotropic metal sites. Finally, we considered from a theoretical point of view the persistence of axial Kramers doublets in the ground state of lantanide ions embedded in low-symmetry sites of polynuclear compounds. The counter-intuitive result that the ground state can be almost axial in an environment completely lacking an axial symmetry was displayed in several crystal field models and shown to be indeed the most common in a broad region of crystal field parameters. The implication of this investigation is the explanation of the reason for blocking of magnetization in low-symmetry complexes involving lanthanide ions.

Among applications of the theory we considered (i) individual polynuclear complexes, (ii) magnetic heterometallic chains and (iii) magnetic nanoparticles doped with lanthanide ions. In all these compounds the unquenched orbital momentum on the metal sites plays an important role in the observed magnetic properties. Thus we were able to explain the unusual magnetism of a [CoPdCo] complex, showing a very large temperature-domain of TIP behavior. Here a combination of spin-orbit coupling and strong antiferromagnetic exchange interaction between the Co(II) ions promoted by electron transfer through Pd(II) leads to the observed behavior.

As application of the theory of decorated Ising chains, two different materials have been described, the $[DyCuMoCu]_\infty$ chain and the $[Dy_4Cr_4]$ cyclic molecule. In the former compound an effective Ising interaction propagates between the ground Kramers doublets on the neighbor Dy(III) sites through magnetically isotropic metal ions Cu(II) and Mo(II). This effective Ising interaction between the Dy(III) ions is also the reason for the S-shaped field-dependent magnetization, which was not observed in the isostructural $[GdCuMoCu]_\infty$ chains involving isotropic Gd(III) ions. In the complex $[Dy_4Cr_4]$ the finite value of χT at zero temperature is found to be very sensitive to the angles of anisotropy axes on Dy(III) sites, while the linear increase of the powder magnetization with field up to 8 Tesla without sign of saturation is actually the result of its averaging over the directions of applied field, while the magnetization markedly differs for different directions.

The variation of the axial character of the Kramers doublets in the low-lying spectrum of eight crystal field levels of Dy(III) ions in the Dy_3 complex, found in *ab initio* calculations, has been reproduced by a simple crystal field model. This gives also credibility to broader conclusions drawn within this model concerning the persistence of the axial nature of the ground Kramers doublet in low-symmetry lanthanides with elevated magnetic moment.

Finally, the ultralow blocking temperature observed in Er^{3+}-doped insulating nanoparticles is explained by the very low exchange interaction between erbium ions. A model taking into account only the local crystal field on sites was able

to describe semi-quantitatively the main features of magnetic susceptibility and magnetization of these nanoparticles, which show significant deviations from other magnetic nanoparticles. As an implication of this finding, we may draw the conclusion of the breakdown of the Néel-Brown giant spin model in these nanoparticles.

Some of the results obtained in this thesis indicate research directions for a future work. Within the theory of exchange interactions, it would be interesting to extend the analysis of superexchange interactions performed here over multiatomic bridging ligands which bring two more contributions to the isotropic exchange parameters, the spin-polarization contribution and the interference between different exchange paths. The last effect does not arise explicitly in the Anderson model and deserves further study because it can be an efficient source for enhancement of ferromagnetic exchange interaction between distant magnetic ions. It would also be interesting to find out how the new exchange model proposed in this thesis is applied for the description of anisotropic exchange interactions between anisotropic magnetic ions. In particular, it would be interesting to see how the microscopic description of Dzialoshinsky-Moria interaction proposed by Morya on the basis of the Anderson model, will change. Another domain of the theory of exchange interactions, which has not been investigated yet, is the effect of spin polarization on the anisotropic exchange constants. Another development of the theory which emerges as continuation of the present work concerns the microscopic theory of dynamics of magnetization in complexes involving strongly anisotropic ions. In contrast to complexes in the strong-coupling limit, where the exchange interaction between the metal sites is stronger than the zero-field splitting on sites, the situation for complexes in the weak-coupling limit, e.g. those involving lanthanides, is opposite. The theory of magnetic dynamics and relaxation in such complexes has not been developed like for complexes in the weak-coupling limit (e.g. Mn_{12} acetate), while there is an increased need for such a theory in view of the growing number of lanthanide-based SMMs. The same can be said for insulating nanoparticles doped by lanthanides, where new phenomena like the anomalous behavior of the blocking temperature with applied dc magnetic field have been observed.

Samenvatting

Deze thesis bevat bijdragen tot de theoretische beschrijving van magnetische eigenschappen van moleculaire materialen. Hierbij werden zowel theoretische modellen zelf bestudeerd (hoofdstuk 2, 4, 5) als de toepassing van theoretische modellen op nieuwe verbindingen en materialen (hoofdstuk 3, 4, 6).

In hoofdstuk 2 wordt de theorie van uitwisselingsinteractie tussen ongepaarde spins op metaalcentra bestudeerd aan de hand van een gedetailleerde vergelijking van de Anderson en VBCI (valence bond configuration interaction) benaderingen in het meest eenvoudige modelsysteem, bestaande uit twee metaalorbitalen gescheiden door een ligandorbitaal. Deze twee veel gebruikte benaderingen behandelen het verbindende ligand als medium voor de uitwisselingsinteractie op een verschillende manier. Met dit onderzoek wilden we een beter begrip krijgen van de waarde van deze methodes om de uitwisselingsconstante te berekenen. In het modelsysteem beschouwden we enkel de belangrijkste interacties tussen en op de drie centra (metaal-ligand-metaal), zodat een minimum model ontstond waarin we de uitwisselingsinteractie tussen de metaalelektronen konden berekenen. De uitwisselingsinteractie (triplet-singlet splitsing) werd benaderd met de Anderson en de VBCI methoden en vergeleken met de exacte oplossing in dit model. Door deze berekeningen uit te voeren voor verschillende waarden van de parameters van het model, kon de toepasbaarheid van beide benaderingen in verscheidene fysische situaties geëvalueerd worden. In het bijzonder werden die situaties geïdentificeerd waarin deze benaderingen tekortschieten om de uitwisselingsinteractie betrouwbaar te berekenen. De oorzaak van het falen ligt telkens in de keuze van nulde-orde golffuncties die dienen als startpunt voor perturbatietheorie. Een correcte behandeling van de metaal-ligand covalente interactie bleek hier cruciaal te zijn. Door deze covalentie exact in te sluiten in de nulde-orde golffunctie ontstaat een perturbatieve benadering waarin covalentie en uitwisselingsinteracties strikt gescheiden zijn en waarmee de uitwisselingsinteractie in alle situaties nauwkeurig benaderd wordt.

In hoofdstuk 3 wordt de temperatuursafhankelijkheid van de magnetische susceptibiliteit van het complex $[Co_2PdCl_2(dpa)_4]$ bestudeerd met behulp van een effectieve spin-orbitaal-Hamiltoniaan. Opmerkelijk aan dit complex is dat

deze susceptibiliteit quasi-constant is tussen 0 en 300 Kelvin, het volledige experimenteel toegankelijke temperatuursgebied. Temperatuursonafhankelijk paramagnetisme is een gekend verschijnsel bij mononucleaire transitiemetaalcomplexen met een niet-magnetische (gesloten schil) grondtoestand. In het CoPdCo complex is dit effect echter 100 keer sterker dan gewoonlijk. De theoretische analyse wordt bemoeilijkt door de orbitaalontaarding en bijgevolg relatief sterke eerste-orde spin-orbitaalkoppeling op de Co^{2+} ionen. Een correcte modelhamiltoniaan moet daarom noodzakelijkerwijs verschillen van de isotrope Heisenberg spinhamiltoniaan voor uitwisselingsinteractie gecombineerd met een "zero-field splitting" term, welke bedoeld is voor systemen zonder eerste-orde spin-orbitaalkoppeling. Een uitgebreidere Hamiltoniaan werd daarom opgesteld die rekening houdt met de spin- en orbitaal-vrijheidsgraden op Co^{2+} en met de uitwisselingsinteractie tussen de Co^{2+} ionen. De open-schil-structuur op Co^{2+} geeft aanleiding tot verschillende mogelijke paden voor uitwisselingsinteractie (elk enkelvoudig bezet orbitaal kan hieraan deelnemen). Hier speelt het Pd^{2+} ion, als brug tussen de Co^{2+} ionen, een belangrijke rol; Pd^{2+} is in een niet-magnetische toestand en wordt door de rigide structuur van de vier dpa liganden redelijk dicht bij de Co^{2+} ionen gebracht. Dit resulteert in een sterke overlap van de d-orbitalen en bijgevolg in een pad voor sterke antiferromagnetische uitwisselingsinteractie tussen de Co^{2+} ionen. Met de nieuwe Hamiltoniaan kon de magnetische susceptibiliteit van het complex goed gereproduceerd en verklaard worden. In het bijzonder werd het temperatuurs-onafhankelijk gedrag toegeschreven aan de onderdrukking van de magnetische momenten van de thermisch bevolkte niveaus door de sterke antiferromagnetische uitwisselingsinteractie.

In hoofdstuk 4 wordt de gedecoreerde Isingketen geïntroduceerd als model voor de magnetische eigenschappen van bepaalde eendimensionale verbindingen gebaseerd op Dy^{3+} ionen. Een gedecoreerde Isingketen kan gezien worden als een eenvoudige Isingketen waarvan alle bindingen vervangen zijn door een moleculaire eenheid (de decorerende eenheid), waarvan de samenstelling willekeurig is. Het anisotrope Dy^{3+} fungeert hier als Ising spin, zowel in de interactie met het magnetisch veld als in de uitwisselingsinteractie met naburige ionen. Dit gedrag is niet vanzelfsprekend en moet gestaafd worden met *ab initio* berekeningen op de individuele Dy^{3+} fragmenten. Indien de juiste voorwaarden vervuld zijn en Dy^{3+} zich inderdaad als een Ising spin gedraagt, heeft dit verregaande vereenvoudigende gevolgen voor de berekening van het spectrum en vooral voor de berekening van thermodynamische eigenschappen. Het is met name mogelijk om de partitiefunctie van het systeem in een arbitrair georienteerd magnetisch veld exact te bekomen met behulp van een transfermatrixmethode. Het probleem reduceert zich dan tot de diagonalisatie van de Hamiltoniaan van één decorerende eenheid. Deze theorie werd toegepast op twee nieuwe magnetische verbindingen: een oneindig lange keten gebaseerd op een [DyCuMoCu] eenheidscel en een ring bestaande uit vier [DyCr] eenheden. Door vergelijking met experimentele metingen van magnetisatie en susceptibiliteit konden waardes

voor de uitwisselingsconstantes afgeleid worden.

In hoofdstuk 5 gaan we dieper in op de axiale anisotropie van Dy^{3+} die een belangrijke rol speelde in het vorige hoofdstuk. Uit recente *ab initio* berekeningen is gebleken dat het laagst gelegen Kramers doublet van Dy^{3+} in een niet-symmetrische coördinatieomgeving vaak slechts heel weinig afwijkt van het cylindrische doublet $|M_J| = 15/2$ (van het atomair $J = 15/2$ multiplet). Dit is eerder onverwacht omdat men steeds aannam dat complexen met hoge axiale symmetrie nodig zijn om zulke eigentoestanden te bekomen. In dit hoofdstuk proberen we met behulp van kristalveldtheorie een inzicht te krijgen in dit gedrag. Hieruit bleek dat het *ab initio* waargenomen patroon van kristalveldtoestanden kwalitatief volledig gereproduceerd kan worden door de tweede-orde-termen in de kristalveldhamiltoniaan. Een berekening in het puntladingsmodel voor een groot aantal willekeurige asymmetrische configuraties van de puntladingen rond Dy^{3+} toont aan dat de grondtoestand met grote waarschijnlijkheid dicht aanleunt bij het doublet van maximale projectie $|M_J| = 15/2$. Deze berekeningen voorspellen ook dat hetzelfde gedrag verwacht wordt voor Er^{3+}. Van deze laatste zijn echter nog geen *ab initio* of experimentele resultaten beschikbaar die deze voorspelling kunnen bevestigen.

Hoofdstuk 6 bevat een toepassing van de magnetische eigenschappen van lanthanide ionen in een kristalveldomgeving op de studie van PbF_2 nanodeeltjes gedopeerd met Er^{3+} ionen. De magnetisatie en susceptibiliteit van deze deeltjes konden semi-kwantitatief beschreven worden door de Er^{3+} ionen als onafhankelijk van elkaar te beschouwen. De opsplitsing van het J multiplet van Er^{3+} in het kubische kristalveld van de PbF_2 matrix leidt tot een spectrum van thermisch toegankelijke niveaus. De variatie van bezetting van deze niveaus in functie van de temperatuur is verantwoordelijk voor het waargenomen magnetische gedrag. De interpretatie van onafhankelijke Er^{3+} ionen is in overeenstemming met de afwezigheid van een blokkeringstemperatuur voor de magnetisatie.

List of abbreviations

AF	antiferromagnetic
And	Anderson
CASSCF	complete active space self-consistent field
CF	crystal field
CN	coordination number
DFT	density functional theory
DIC	decorated Ising chain
EDX	energy-dispersive X-ray spectroscopy
F	ferromagnetic
FC	field-cooled
HF	Hartree-Fock
KD	Kramers doublet
L	ligand
M	metal
NGC	nano-glass-ceramic
RASSI-SO	restricted active space state interaction - spin-orbit
RKKY	Ruderman-Kittel-Kasuya-Yosida
ROHF	restricted open-shell Hartree-Fock
SCM	single-chain magnet
SMM	single-molecule magnet
SQUID	superconducting quantum interference device
TEM	transmission electron microscopy
TIP	temperature-independent paramagnetism
UHF	unrestricted Hartree-Fock

VBCI	valence bond configuration interaction
VSM	vibrating sample magnetometer
ZFC	zero-field-cooled

Publications

1. *A CASPT2 study of the electronic spectrum of hexacyanoosmate(III),*
   W. Van den Heuvel, M. F. A. Hendrickx, and A. Ceulemans,
   Inorg. Chem. **46**, 8032 (2007)

2. *Basic exchange model: Comparison of Anderson and valence bond configuration interaction approaches and an alternative exchange expression,*
   W. Van den Heuvel and L. F. Chibotaru,
   Phys. Rev. B. **76**, 104424 (2007)

3. *Ab initio investigation of the non-collinear structure and the lowest magnetic excitations in dysprosium triangles,*
   L. Ungur, W. Van den Heuvel, and L. F. Chibotaru,
   New J. Chem. **33**, 1224 (2009)

4. *Elucidation of the magnetism of $[Co_2PdCl_2(dpa)_4]$: Origin of a large temperature domain of TIP behavior,*
   W. Van den Heuvel and L. F. Chibotaru,
   Inorg. Chem. **48**, 7557 (2009)

5. *First Heterotrimetallic {3d-4d-4f} Single Chain Magnet, Constructed from Anisotropic High-spin Heterometallic Nodes and Paramagnetic Spacers,*
   D. Visinescu, A. M. Madalan, M. Andruh, C. Duhayon, J.-P. Sutter, L. Ungur, W. Van den Heuvel, and L. F. Chibotaru,
   Chem. Eur. J. **15**, 11808 (2009)

6. *An octanuclear [Cr4Dy4] compound: The first example of a 3d/4f single-molecule magnet containing Cr^{III},*
   J. Rinck, G. Novitchi, W. Van den Heuvel, L. Ungur, Y. Lan, C. E. Anson, L. F. Chibotaru, and A. K. Powell,
   submitted to Angew. Chem. Int. Ed.

7. *Ultralow blocking temperature and breakdown of the giant spin model in Er^{3+}-doped nanoparticles,*
   W. Van den Heuvel, V. K. Tikhomirov, D. Kirilenko, N. Schildermans, L. F. Chibotaru, J. Vanacken, P. Gredin, M. Mortier, G. van Tendeloo, and V. V. Moshchalkov,
   submitted to Phys. Rev. B

8. *The decorated Ising chain in molecular magnetism,*
   W. Van den Heuvel and L. F. Chibotaru,
   in preparation

9. *Axial magnetic anisotropy of Dy^{3+} and Er^{3+} in crystal fields without symmetry,*
   W. Van den Heuvel and L. F. Chibotaru,
   in preparation